

# Novel aerosol condensing heat exchanger for small-scale biomass combustion applications

**Citation for published version (APA):**

Best, de, C. J. J. M. (2007). *Novel aerosol condensing heat exchanger for small-scale biomass combustion applications*. [Phd Thesis 1 (Research TU/e / Graduation TU/e), Mechanical Engineering]. Technische Universiteit Eindhoven. <https://doi.org/10.6100/IR630972>

**DOI:**

[10.6100/IR630972](https://doi.org/10.6100/IR630972)

**Document status and date:**

Published: 01/01/2007

**Document Version:**

Publisher's PDF, also known as Version of Record (includes final page, issue and volume numbers)

**Please check the document version of this publication:**

- A submitted manuscript is the version of the article upon submission and before peer-review. There can be important differences between the submitted version and the official published version of record. People interested in the research are advised to contact the author for the final version of the publication, or visit the DOI to the publisher's website.
- The final author version and the galley proof are versions of the publication after peer review.
- The final published version features the final layout of the paper including the volume, issue and page numbers.

[Link to publication](#)

**General rights**

Copyright and moral rights for the publications made accessible in the public portal are retained by the authors and/or other copyright owners and it is a condition of accessing publications that users recognise and abide by the legal requirements associated with these rights.

- Users may download and print one copy of any publication from the public portal for the purpose of private study or research.
- You may not further distribute the material or use it for any profit-making activity or commercial gain
- You may freely distribute the URL identifying the publication in the public portal.

If the publication is distributed under the terms of Article 25fa of the Dutch Copyright Act, indicated by the "Taverne" license above, please follow below link for the End User Agreement:

[www.tue.nl/taverne](http://www.tue.nl/taverne)

**Take down policy**

If you believe that this document breaches copyright please contact us at:

[openaccess@tue.nl](mailto:openaccess@tue.nl)

providing details and we will investigate your claim.

Novel aerosol condensing heat exchanger  
for small-scale biomass combustion applications

PROEFSCHRIFT

ter verkrijging van de graad van doctor aan de  
Technische Universiteit Eindhoven, op gezag van de  
Rector Magnificus, prof.dr.ir. C.J. van Duijn, voor een  
commissie aangewezen door het College voor  
Promoties in het openbaar te verdedigen  
op maandag 17 december 2007 om 14.00 uur

door

Carlo Jacobus Johannes Maria de Best

geboren te Wamel

Dit proefschrift is goedgekeurd door de promotoren:

prof.dr.ir. J.J.H. Brouwers  
en  
prof.Dr.Dipl.-Ing. I. Obernberger

Copromotor:  
dr.ir. H.P. van Kemenade

Copyright © 2007 by C.J.J.M. de Best  
All rights reserved. No part of this publication may be reproduced, stored in a retrieval system, or transmitted, in any form, or by any means, electronic, mechanical, photocopying, recording, or otherwise, without the prior permission of the author.

Cover design: Oranje Vormgevers Eindhoven ([www.oranjevormgevers.nl](http://www.oranjevormgevers.nl)).

Printed by the Eindhoven University Press.

A catalogue record is available from the Library Eindhoven University of Technology

ISBN: 978-90-386-1157-0





# Contents

<b>Summary</b>	<b>9</b>
<b>1 Introduction</b>	<b>13</b>
1.1 Definition of area of interest . . . . .	13
1.2 Particle formation during biomass combustion . . . . .	14
1.3 Objectives and approach . . . . .	17
<b>2 Basic principles</b>	<b>19</b>
2.1 Introduction . . . . .	19
2.2 Heterogeneous condensation vs. wall condensation . . . . .	20
2.3 Closure . . . . .	26
<b>3 Plug flow model with particle formation in a heat exchanger</b>	<b>27</b>
3.1 Introduction . . . . .	27
3.2 Aerosol formation process . . . . .	28
3.3 Modeling approach . . . . .	30
3.4 Aerosol dynamics . . . . .	34
3.4.1 Homogeneous nucleation . . . . .	35
3.4.2 Heterogeneous condensation . . . . .	36
3.4.3 Coagulation . . . . .	37
3.5 Total change of vapour pressure . . . . .	39
3.5.1 Change of vapour pressure due to particle formation and growth	39
3.5.2 Change of vapour pressure due to wall condensation . . . . .	39
3.6 Change of flue gas temperature . . . . .	40
3.7 Solution procedure and initial conditions . . . . .	41
3.7.1 Determination of step size $\Delta z$ . . . . .	42
3.8 Results . . . . .	44
3.8.1 Effect of varying the initial flue gas velocity . . . . .	45
3.8.2 Effect of varying the initial PSD . . . . .	46
3.8.3 Influence of coagulation . . . . .	48
3.8.4 Effect of insulation on the wall condensation rate . . . . .	50
3.9 Influence of the surface tension on the homogeneous nucleation rate .	53
3.10 Closure . . . . .	57

<b>4</b>	<b>2D model with particle formation and particle deposition in a heat exchanger</b>	<b>59</b>
4.1	Introduction . . . . .	59
4.2	Modeling approach . . . . .	60
4.2.1	Momentum equation . . . . .	61
4.2.2	Energy equation . . . . .	62
4.2.3	Continuity equation for aerosol forming species . . . . .	62
4.2.4	Particle deposition . . . . .	62
4.2.5	Solution method . . . . .	65
4.3	Results . . . . .	66
4.3.1	Particulate emission reduction in a cylindrical tube without consideration of additional forces acting on aerosol particles . . . . .	67
4.3.2	Particulate emission reduction in a cylindrical tube with consideration of additional forces acting on aerosol particles . . . . .	69
4.4	Analysis of particle deposition mechanisms . . . . .	71
4.5	Conversion from cylindrical coordinates to arbitrary coordinates . . . . .	77
4.6	Closure . . . . .	79
<b>5</b>	<b>Experiments: Proof of concept</b>	<b>81</b>
5.1	Introduction . . . . .	81
5.2	Methodology . . . . .	81
5.2.1	Biomass combustion plant used for experiments . . . . .	81
5.2.2	Requirements for the experimental aerosol condensing heat exchangers . . . . .	83
5.2.3	Measurement techniques . . . . .	83
5.2.4	Determination of the chemical composition of fuels and aerosols . . . . .	84
5.2.5	Calculations regarding the maximum potential for aerosol formation . . . . .	84
5.2.6	Definitions of emission reduction efficiencies . . . . .	84
5.3	Laminar flow shell and tube heat exchanger . . . . .	85
5.3.1	Description HE1 and HE2 with variable tube dimensions of 12.50 and 6.20 mm . . . . .	86
5.3.2	Description of HE3 with a tube dimension of 1.07 mm . . . . .	87
5.3.3	Design calculations concerning the laminar flow shell and tube heat exchanger . . . . .	88
5.3.4	Results from test runs with laminar flow shell and tube heat exchangers . . . . .	89
5.3.5	Analysis of the working efficiency concerning HE3 . . . . .	97
5.4	Compact laminar counterflow gas to gas heat exchanger . . . . .	102
5.4.1	Description of HE4, the compact laminar counterflow gas to gas heat exchanger . . . . .	102
5.4.2	Design calculations concerning HE4 . . . . .	103
5.4.3	Results from test runs with HE4 . . . . .	104
5.5	Comparison of experiments with theory . . . . .	107

---

<b>6 Experiments: Towards a commercial design</b>	<b>111</b>
6.1 Insulated plate type heat exchanger . . . . .	111
6.1.1 Description of HE5, insulated plate type heat exchanger . . . . .	112
6.1.2 Design calculations concerning HE5 . . . . .	115
6.1.3 Results from test runs with HE5 . . . . .	119
6.2 Comparison of experimental results of HE5 with simulations . . . . .	130
6.3 Fin tube heat exchanger . . . . .	131
6.3.1 Description of HE6, fin tube heat exchanger . . . . .	132
6.3.2 Results from test runs with HE6 . . . . .	134
6.4 Closure . . . . .	147
<b>7 Conclusions</b>	<b>149</b>
7.1 Future outlook . . . . .	151
<b>Bibliography</b>	<b>153</b>
<b>A Transport equations in cartesian coordinates</b>	<b>157</b>
<b>Dankwoord</b>	<b>159</b>
<b>Curriculum vitae</b>	<b>161</b>





# Summary

## Novel aerosol condensing heat exchanger for small-scale biomass combustion applications

In order to meet the Kyoto targets, CO<sub>2</sub> emissions have to be reduced significantly. The use of biomass fuels is regarded as one of the options to reduce greenhouse gas emission. However, combustion of biomass fuels is accompanied by considerable fine particulate (PM<sub>1</sub>) matter emissions, the so called aerosols, that could cause health risks. In large and medium-scale combustion plants, these aerosols can easily and cost efficiently be precipitated from the flue gas by use of baghouse filters or electrostatic precipitators. However, up to now no economically attractive aerosol precipitation techniques are available for small-scale biomass combustion applications.

In order to arrive at an economically attractive aerosol precipitation technique, first the aerosol formation process is investigated. It is known that during combustion of biomass, aerosol forming compounds are released from the fuel to the gas phase. Subsequently, these compounds undergo gas phase reactions. When the flue gas temperature decreases, these aerosol forming compounds can become supersaturated, resulting in aerosol formation by homogeneous nucleation or condensation on already existing surfaces. As current boiler designs aim at minimisation of aerosol forming compounds on heat exchanging surfaces, it should also be possible to stimulate aerosol forming vapours on these surfaces. From this, it appears that one way to reduce fine particulate matter emissions from the flue gas is to stimulate condensation of aerosol forming vapours on heat exchanger surfaces so that the emitted aerosol mass is reduced. It is noted that a cost efficient heat exchanger cleaning system has to be devised to remove the fouling layer.

First, an analytical approach is performed to investigate whether there is a physical basis that condensation of aerosol forming vapours indeed can be stimulated. In this approach, condensation of aerosol forming vapours on heat exchanger surfaces and already existing particles are incorporated, whereas formation of new particles is neglected. The calculations in this approach and in the further numerical studies are limited to one aerosol forming compound only, namely potassium sulphate. Analysis of aerosols sampled downstream the boiler and the aerosol condensing heat exchanger as well from analysis of aerosols sampled inside the furnace supported this assumption. The result of this approach showed that decreasing the tube dimensions in the millimetre regime resulted in significant aerosol emission reductions, up to  $\approx 90\%$

using tube dimensions of 2 *mm*.

In order to investigate whether particle formation by homogeneous nucleation might cause significant deviations compared to the analytical approach, a plug flow model incorporating condensation and formation of aerosol forming vapours is derived. The results obtained by this model confirm the trend already obtained by the analytical approach without homogeneous nucleation. Besides this, the model also showed that reduction of the temperature gradient of the flue gas results in higher precipitation efficiencies of aerosol forming vapours on heat exchanger surfaces.

From literature is also known that external forces acting on already existing aerosol particles, such as thermophoresis and lift force [44, 32, 22], might cause a reduction in fine particulate emission. Analysis of a 2D model showed that the effect of additional particle deposition  $\approx 18\%$  for aerosol sizes typically found during combustion of woody biomass fuels. From the 2D model, it can also be concluded that the hydraulic diameter is a parameter that can be used to predict the condensation rate of aerosol forming vapours on heat exchanger surfaces for arbitrary heat exchanger geometries.

In order to verify the analytical and modeling approach, experiments with water cooled heat exchanger designs that stay close to commonly used boiler geometries are performed. Three different tube dimensions were used for the experiments, respectively 12.50, 6.20 and 1.07 *mm*. Average aerosol emission reductions compared to ordinary boiler designs of 28 and 36 % could be achieved using tube dimensions of respectively 12.50 and 6.20 *mm*. Experiments with a water cooled heat exchanger having tube dimension of 1.07 *mm* were not successful. Heat transfer near the heat exchanger inlet was significant due to the lack of insulation between the furnace and the cold heat exchanger surface towards the furnace, resulting in lower flue gas temperatures near the heat exchanger inlet than is expected based on temperature measurements inside the furnace. Consequently, nucleation and condensation of aerosol forming compounds already occurred before the flue gas entered the heat exchanger, resulting in a deficient condensation rate of aerosol forming vapours inside the heat exchanger. Therefore, a compact laminar counterflow gas to gas heat exchanger with a hydraulic diameter of 2.22 *mm* originally developed for recuperative burners was applied resulting in an aerosol emission reduction of about 70 %.

From a practical point of view, small tube dimensions are not attractive. Blocking with coarse particles rapidly results in a decrease of the heat transfer. This problem, in combination with a bad accessibility regarding cleaning make such heat exchangers not suitable. In order to avoid blocking, it is useful having larger tube dimensions. From the modeling results could be observed that reducing the temperature gradient results in higher condensation rates of aerosol forming vapours on heat exchanger surfaces. This phenomenon can be used to arrive at a cost efficient aerosol condensing heat exchanger. At first an insulated plate type heat exchanger was designed and tested to see whether channel dimensions with a hydraulic diameter of 6 *mm* indeed result in significant aerosol emission reductions. Experiments showed that aerosol emission reductions of 80 % could be achieved using combustion temperatures of about 1000 °C, while at combustion temperature of 800 °C still a reduction of about 64 % could be observed.

In order to arrive at a commercially viable solution, a fin tube heat exchanger,

with a hydraulic diameter of approximately 4 *mm* was designed and tested that can withstand temperatures up to 1000 °C. The fins are carried out with an extra heat resistance, in the form of holes in the fins, to have the desired temperature gradient of the flue gas. A flexible connection between the fins and the tubes is applied to minimise thermal stresses. This design gave aerosol emission reductions of 80 % at combustion temperatures of about 1050 °C, whereas average aerosol emission reductions of 59 % could be observed using combustion temperatures of about 800 °C.

In this work it is proven that aerosol emissions indeed can be reduced by stimulation of aerosol forming vapours on heat exchanger surfaces. Besides heat exchanger designs for lab-scale testing, also a step towards a commercially attractive aerosol condensing heat exchanger design was made, resulting in a fin tube heat exchanger that can operate at high temperatures. The fin tube heat exchanger has proven its general applicability in biomass combustion processes within this work. Further development is required on the improvement of the manufacturing process of the heat exchanger as well as on the implementation of an automated cleaning system.



# Chapter 1

## Introduction

Worldwide the Total Primary Energy Supply (TPES) is still increasing. Data presented in the Key World Energy Statistics 2007 of the International Energy Agency [25] show that the global energy consumption has increased from 6128 Mtoe in 1973 up to 11435 Mtoe in 2005. The corresponding CO<sub>2</sub> emissions increased from 15661 Mt in 1973 up to 27136 Mt in 2005. From these data it can be observed that in this time interval most of the extra required energy is produced by non CO<sub>2</sub> neutral energy sources like oil, gas and coal. In order to meet the Kyoto targets, the CO<sub>2</sub> emissions have to be reduced significantly. Bio-energy is regarded as one of the options to mitigate greenhouse gas emissions and substitute fossil fuels [16]. However, a disadvantage of the combustion of biomass fuels compared to liquid and gaseous fuels is that this process is accomplished with considerable particulate matter (PM) emissions that could cause health risks [7]. Therefore, methods to reduce particulate matter emissions from biomass combustion systems have to be implemented in order to arrive at a complete environmentally friendly energy conversion method. In medium and large-scale biomass combustion plants, fine particulate matter emissions can cost efficiently be precipitated from the flue gas using highly efficient dust precipitation devices like baghouse filters or electrostatic precipitators. For small-scale biomass combustion systems such devices are not available. Therefore, this work is focussed on the development of a cost efficient aerosol precipitation technique for small-scale biomass combustion systems.

### 1.1 Definition of area of interest

Several methods for energetic biomass utilisation can be distinguished. In general, distinction can be made between thermochemical and biochemical conversion processes. Examples of biochemical biomass conversion processes are fermentation for alcohol production and anaerobic digestion for production of methane-enriched gas, see Van Loo [50]. This work is related to the first route of biomass conversion, namely thermochemical conversion technologies, especially biomass combustion processes. Combustion is the most advanced and most frequently applied thermochemical conversion

technology for solid biomass fuels. Besides combustion technologies also gasification and pyrolysis are examples of thermochemical conversion technologies, which become more and more important.

Regarding combustion based systems, a broad spectrum of biomass combustion technologies suitable for different biomass fuels covering a wide range of plant capacities can be distinguished. In this thesis, combustion plants are classified in three main categories with respect to their capacity.

- *Small-scale biomass combustion plants* are combustion plants with a nominal capacity  $< 100 kW_{th}$ . These systems are mainly used for residential and central heating purposes. Woody biomass fuels like pellets and chemically untreated wood chips are commonly used as fuels for small-scale biomass combustion applications.
- *Medium-scale biomass combustion plants* cover the nominal capacity range between  $100 kW_{th}$  up to  $10 MW_{th}$ . Several biomass fuels can be used in such systems. Besides woody biomass fuels like wood chips, sawdust, bark, forest residues and waste wood also straw and agricultural residues can be applied.
- *Large-scale biomass combustion plants* cover the range with nominal capacities  $> 10 MW_{th}$ . Large-scale biomass combustion plants are used for heating purposes, CHP plants and biomass combustion plants for power production only. A wide variety of biomass based fuels and residues of agricultural industry can be used as a fuel.

As already mentioned, particulate matter emissions from biomass combustion plants are considerable. In the past, several filtering techniques for different plant capacities have been developed and implemented to meet the current requirements regarding particulate matter emissions. Nowadays, cost efficient aerosol (particles  $< 1 \mu m$ ) precipitation techniques for medium- and large-scale applications are available. However, for small-scale applications no cost efficient techniques are available. Still a lot of development effort is required to arrive at a practical and cost efficient filtering technique for small-scale biomass combustion plants. Therefore, this work focusses on the development of a device for cost efficient particulate matter reduction for small-scale biomass combustion plants, as long as almost complete gas phase burnout prevails.

## 1.2 Particle formation during biomass combustion

In general, the fly ash fraction formed during biomass combustion exhibits a bi-modal particle size distribution and can be divided into a coarse mode and a fine mode. An example of the bi-modal particle size distribution of the total fly ash emission during the combustion of wood chips is depicted in Fig. 1.1. Coarse fly ash particles usually have particle sizes that can vary between a few  $\mu m$  up to about  $200 \mu m$ . The coarse fly ash particles can be removed cost efficiently for the entire range of combustion plants using cyclones or multi cyclones [8, 11]. The second fraction is formed by the

so called aerosols having aerodynamic diameters  $< 1 \mu\text{m}$ . Depending on the fuel used, aerosol emissions between  $20 \text{ mg}/\text{Nm}^3$  (13 vol%  $\text{O}_2$ ) for chemically untreated wood chips and pellets up to about several hundreds of  $\text{mg}/\text{Nm}^3$  for waste wood can be observed.

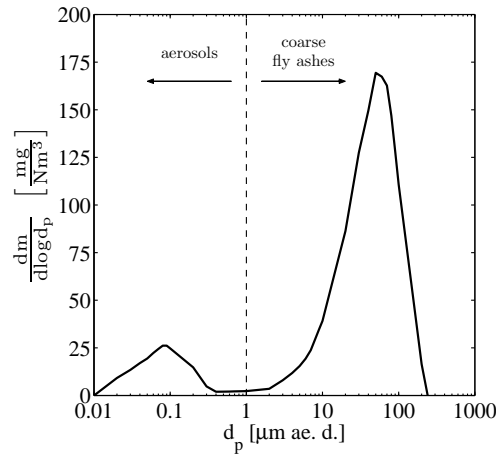


**Figure 1.1.** Typical example of a bi-modal particle size distribution of fly ash emissions from fuel bed combustion of wood chips. Source [15].

Explanations: Concentrations related to dry flue gas and 13 vol.%  $\text{O}_2$ ; ae. d. ... aerodynamic particle diameter.

The reason for two different fly ash fractions is the fact that the particle formation processes for coarse fly ash particles and aerosols are completely different. Before the fuel enters the combustion unit, it is dried. The volatile combustible species are then released from the fuel during a pyrolysis/gasification step and are oxidised during homogeneous gas phase reactions with combustion air. Finally, the oxidation of the fixed carbon takes place during charcoal combustion. During these processes, a part of the non-volatile ash forming matter in the biomass fuel is entrained from the fuel bed and forms the coarse fly ashes. In general, these coarse fly ashes mainly consist of inorganic ash forming matter like Ca, Si, K, Mg, and Fe. Once the organic matter has been released or oxidised, these elements remain as coarse fly ash structures. The coarse fly ash fraction increases with the boiler load due to higher flue gas velocities and is strongly depending on the ash content of the fuel, the combustion technology applied, the design of the combustion unit and the process control system used [11].

The aerosol formation process is much more complicated and therefore a closer look on the combustion process is needed to explain aerosol formation. During combustion of woody biomass fuels, the aerosol formation process in fixed bed combustion systems follows a basic scheme, see Fig. 1.2. Besides main organic elements like C, H, O and N, biomass fuels also contain ash forming elements. These inorganic elements can originate from the plant itself, as they are a part of the structure of the fibres, as well as from sand, stones or other kinds of contaminations of the fuel. An example of the



**Table 1.1.** Typical chemical composition of wood chips based on five independent fuel analysis.

Explanation: d.b. ... dry base; w.b. ... wet base; STD ... standard deviation.

parameter	unit	average value & STD
Moisture	wt. % (w.b.)	28 ± 1.8
Ash	wt. % (d.b.)	0.9 ± 0.1
S	mg/kg (d.b.)	134 ± 5
Cl	mg/kg (d.b.)	80 ± 6
Ca	mg/kg (d.b.)	2251 ± 364
Si	mg/kg (d.b.)	529 ± 480
Mg	mg/kg (d.b.)	270 ± 17
K	mg/kg (d.b.)	758 ± 119
Na	mg/kg (d.b.)	21 ± 6
Zn	mg/kg (d.b.)	8 ± 5
Pb	mg/kg (d.b.)	14 ± 6

chemical composition of chemically untreated wood chips which is commonly used in small-scale biomass combustion plants is depicted in Tab. 1.1.

A considerable part of the easily volatile aerosol forming elements (e.g. K, Cl, S, Pb, Na and Zn) is released from the fuel to the gas phase during combustion and subsequently undergoes chemical reactions, resulting in the formation of e.g. alkaline sulphates, chlorides and carbonates as well as heavy metal oxides. As soon as these compounds reach supersaturation, particle formation by nucleation takes place. Supersaturation can occur due to excessive formation of a compound or due to the cooling of the flue gas. The particles formed by nucleation are very small in size, about 5 to 10 *nm*, but on their way with the flue gas, these particles grow by coagulation, agglomeration and condensation of aerosol forming compounds on their surfaces [34, 11, 30, 46, 13, 50]. These particles form the major part of the aerosol fraction, characterised by a particle size < 1  $\mu m$ . Consequently, the main difference in the particle formation processes of coarse fly ashes and aerosols is that coarse fly ashes always remain in the solid phase, whereas aerosols undergo gas phase reactions, followed by gas to particle conversion mechanisms during their formation process, resulting in small particles.

As inorganic aerosols cannot be avoided, the formation of the 2<sup>nd</sup> fraction, namely organic aerosols can be avoided. Organic aerosol are formed when the charcoal and flue gas burnout is not fully completed. Soot and hydrocarbons may form aerosols. In modern small-scale biomass combustion plants emissions caused by organic compounds are very low. Appropriate air staging and well designed air injection nozzles for secondary air injection ensure an extensive mixing of the combustion air with flue gases so that organic emissions are almost negligible. To ensure a complete gas phase burnout, furnace temperatures in modern small-scale biomass combustion plants are usually above 850 °C. It is noticed that, especially at low load operation, the tem-

temperatures in the regions of the cooled furnace walls are not high enough to complete the oxidation process, resulting in slight organic aerosol emissions. On the other hand, old, badly operating combustion systems can show very high organic aerosol emissions.

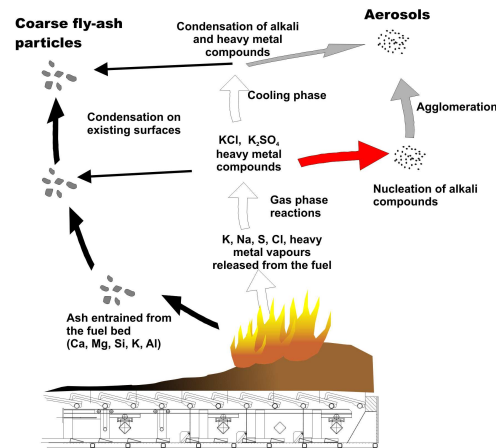


**Figure 1.2.** Particle formation process during fixed-bed combustion of chemically untreated wood chips. Figure obtained from [15].

### 1.3 Objectives and approach

As already mentioned, coarse fly ash particles can easily be removed from the flue gas by the use of cost efficient precipitation techniques like cyclones or multi-cyclones [8, 11]. Baghouse filters or electrostatic precipitators, as applied in medium and large-scale biomass combustion plants to precipitate aerosol particles from the flue gas are presently from an economic point of view not suitable for small-scale combustion units. Therefore, a cost efficient technique has to be developed which specially aims at the reduction of aerosol emissions in small-scale biomass combustion units.

Provided that an almost complete combustion prevails, mainly inorganic easily volatile ash forming elements (e.g. K, Cl, S, Pb, Na and Zn) are responsible for aerosol formation. During combustion, these elements are partially released to the flue gas. Depending on the cooling rate and the concentration of ash forming elements in the flue gas, these volatilised compounds nucleate or condense on the surface of pre-existing particles in the flue gas as well as on the cold surfaces of the heat exchanger, see Van Kemenade [48]. Consequently, it may be possible to reduce aerosol emissions by enhancing wall condensation, contrary to the goal of current heat exchanger designs which aims at the minimisation of particle deposit formation. If this emission reduction is high enough to eliminate the need for an expensive flue gas treatment system, the additional costs of a heat exchanger cleaning system may be justified.

The objective of this work can therefore be defined as:

- *Investigation of the feasibility of designing a heat exchanger for small-scale biomass combustion plants wherein condensation of aerosol forming vapours directly on the heat exchanger surfaces is stimulated in order to reduce aerosol formation and emissions (the so called aerosol condensing heat exchanger).*
- *Development of models describing the aerosol formation and deposition processes, with which parameters that may influence aerosol emission reduction can be analysed and quantified. Based on sensitivity analysis, constraints regarding heat exchanger designs should be determined.*
- *Design and testing of heat exchangers according to the aerosol condenser concept to proof the concept and to verify the modeling results.*
- *Stepwise optimisation to arrive at an appropriate and commercially attractive aerosol condensing heat exchanger concept.*

Therefore, in chapter 2, a first order estimation of the competing mechanisms of wall condensation and heterogeneous condensation on already existing particle surfaces in a heat exchanger passage is made to investigate the relevant parameters for dimensioning an aerosol condensing heat exchanger. Continuum diffusion with a correction factor for diffusion outside the continuum regime is used to determine the particle growth rate, whereas a Sherwood relation is used to determine the wall condensation rate.

In chapter 2, formation of new particles is left out of consideration. In order to investigate the influence of particle formation, a plug flow model that besides wall condensation and heterogeneous nucleation also includes particle formation via homogeneous nucleation is derived in chapter 3. A Classical Nucleation Theory (CNT) is used to describe the particle formation process. For the sake of simplicity the model derived is restricted to one single aerosol forming compound only. A worst case estimation is obtained assuming that the compound used in the simulations, covering the whole range of aerosol forming compounds, is the most sensitive compound for nucleation. The results obtained by the plug flow model should reconfirm trends regarding design issues, already obtained in chapter 2. Furthermore, the plug flow model should provide new insights regarding aerosol reduction based on fundamental knowledge.

Besides stimulation of vapour deposition on heat exchanger surfaces, also direct deposition of existing aerosol particles might cause an emission reduction. Literature is investigated to determine which additional forces could contribute to the reduction of fine particulate matter emissions. A 2D model describing the temperature and velocity field as well as the deposition rate of both particles and aerosol forming vapours on heat exchanger surfaces is developed, in chapter 4. Then a commercially attractive design should be developed and tested.

# Chapter 2

## Basic principles\*

### 2.1 Introduction

The objective of this work is to investigate the feasibility of designing a heat exchanger wherein direct condensation of aerosol forming vapours on heat exchanger surfaces is stimulated such that particle formation and emissions are reduced. Van Kemenade [48] derived a model in order to investigate which mechanisms cause fine particulate emission reductions in conventional boiler designs. The model derived includes transport mechanisms of both particles and aerosol forming vapours. It has been shown that concerning deposition mechanisms towards heat exchanger walls like thermophoresis, Brownian diffusion, eddy impactation and direct condensation of aerosol forming vapours on heat exchanger surfaces only direct condensation of aerosol forming vapours on heat exchanger surfaces had a significant impact on the aerosol emission reduction. Further analysis showed that current boiler designs are such that within the limits of the applications deposition is minimised, as is to be expected to minimise fouling of the heat exchanger surfaces. However, small-scale installations might benefit from a heat exchanger that stimulates fouling as a mechanism to reduce aerosol formation. It is noticed that a cost efficient heat exchanger cleaning system for removing the fouling layer has to be devised.

In order to see whether stimulated condensation of aerosol forming vapours on heat exchanger surfaces is indeed possible, a physical basis is required. Therefore, a first order estimation of the main competing processes regarding gas to particle conversion mechanisms is made. The competing processes included in the analysis are direct condensation of aerosol forming vapours on heat exchanger surfaces and heterogeneous condensation on already existing aerosol particles in a heat exchanger passage. Formation of new particles due to homogeneous nucleation as described in Pyykönen, Christensen and Jöller et al. [35, 13, 30] is thus neglected.

---

\*This chapter is partially reproduced from: *de Best, C.J.J.M. et al. Particulate emission reduction in small-scale biomass combustion plants by a condensing heat exchanger*, accepted for publication in *Energy & Fuels*

## 2.2 Heterogeneous condensation vs. wall condensation

As soon as the flue gas temperature equals the condensation temperature of aerosol forming species in a heat exchanger, condensation on pre-existing particles as well as on heat exchanger walls take place as competing processes. To make a first order estimation of the amount of vapour condensing on the walls of a heat exchanger, it is assumed that both the nuclei in the gas and the walls of the heat exchanger are below the condensation temperature of the aerosol forming vapours. In that case the vapour molecules diffuse both to the walls and to the already existing aerosol particles. In order to simplify the calculations regarding the condensation rate on particles and on heat exchanger walls it is assumed that the number concentration of aerosol particles near the heat exchanger inlet and during the cooling process is constant.

From measurements it is known that a rather constant aerosol number concentration downstream hot water boilers can be observed, which is usually in the order of  $1 \cdot 10^{13} \text{ Nm}^{-3}$ , see Brunner [10]. It is expected that the number concentration of aerosols during the cooling process does not change significantly, implying that the number concentration of aerosols near the heat exchanger inlet is also within the same range. The reason for this constant number concentration can be attributed to coagulation processes. ZnO particles for instance are assumed to form in large amounts directly after the flue gases leave the fuel bed [9]. On their way with the flue gas, these particles are able to coagulate. The final number concentration when the aerosol particles enter the heat exchanger inlet mainly depends on the initial number concentration and on the time available. To illustrate this coagulation process, a simple monodisperse coagulation model is used in order to predict the number concentration as a function of time. The time dependent coagulation process is given by Hinds [24]:

$$N(t) = \frac{N_0}{1 + N_0 K_0 t}, \quad (2.1)$$

where  $N_0$  represents the initial number concentration,  $K_0$  is the coagulation coefficient and  $t$  represents the time. The coagulation coefficient is determined at a typical flue gas temperature of  $1000 \text{ }^\circ\text{C}$ .

Figure 2.1 shows a graphical representation of the number concentration decrease for various initial number concentrations. Assuming a residence time of the flue gas inside the furnace of at least one second (see Brunner [9]) yields that the number concentration near the heat exchanger inlet is always within the range of  $1 \cdot 10^{13} \text{ Nm}^{-3}$ , which is a conservative approximation. Because the time required for further coagulation increases exponentially. It is unlikely that the aerosol number concentration in the heat exchanger itself decreases significantly. Especially taking into account that the residence time inside the heat exchanger (so the time available for coagulation) is also limited to less than one second. Furthermore, it is assumed that particle formation by nucleation as described in literature [35, 13, 30] is widely suppressed due to the high aerosol concentration near the heat exchanger inlet. Therefore, it is reasonable to exclude formation of new particles in the first analysis.

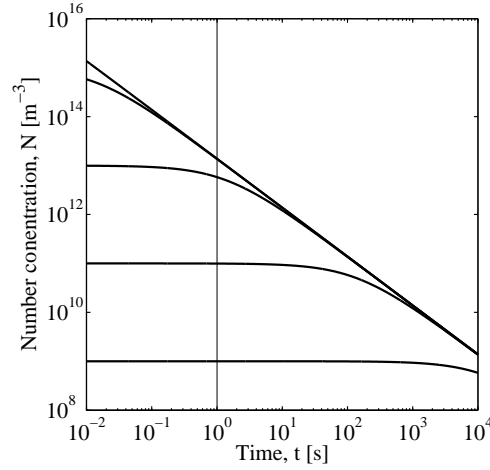


**Figure 2.1.** A logarithmic representation of a simple monodisperse coagulation model. The coagulation coefficient  $K_0$  is evaluated at a flue gas temperature of  $1000\text{ }^\circ\text{C}$ . The horizontal axis represents the time  $t$ , whereas the vertical axis represents the number concentration  $N$ .

In order to estimate the wall condensation rate, a laminar flow in an axi-symmetric heat exchanger tube is assumed. The reason for choosing round tubes is based on the fact that current boiler designs also exhibit this geometry. The laminar flow is indicated by a Reynolds number lower than 2300 [6]:

$$Re = \frac{D_{tube}\rho_g v_g}{\mu_g} < 2300. \quad (2.2)$$

In Eq. 2.2,  $D_{tube}$  represents the tube diameter of one heat exchanger tube.  $\rho_g$  and  $\mu_g$  represent the density and the dynamic viscosity of the flue gas, whereas  $v_g$  represents the axial bulk velocity of the flue gas.

The mass vapour flux towards the walls of the heat exchanger per unit length  $j'_{\alpha,w}$  can be written as (Bird et al. [6]):

$$j'_{\alpha,w} = \frac{Sh(D_{tube})\pi\mathbb{D}M_\alpha}{R_u T_g} (p_{\alpha,w} - p_{\alpha,g}), \quad (2.3)$$

where  $M_\alpha$  represents the molar mass of the aerosol forming compound,  $R_u$  is the universal gas constant,  $T_g$  is the flue gas temperature,  $p$  is the partial vapour pressure, whereas  $\mathbb{D}$  represents the diffusion coefficient of the aerosol forming vapours. The subscript  $\alpha$  refers to the aerosol forming vapour compound, whereas the subscripts  $w$  and  $g$  refer to its position, respectively on the wall of the heat exchanger and relatively far away from the wall in the bulk of the flue gas. In Eq. 2.3,  $Sh(D_{tube})$  represents the Sherwood number, which is a dimensionless number to calculate the mass-transfer rate. This number represents the ratio of the length scale (in this case the tube diameter,  $D_{tube}$ ) to the diffuse boundary layer thickness. Since a fully

developed laminar flow is assumed, the Sherwood number is constant at 3.66 when applying a constant wall concentration (Bird et al. [6]).

A similar relation as described in Eq. 2.3 but now for the vapour flux towards the particles in the tube per unit length is derived. The total particle surface area in a tube per unit length  $A'_p$  is defined as:

$$A'_p = \pi d_p^2 N \frac{\pi}{4} D_{tube}^2, \quad (2.4)$$

where the term  $\pi d_p^2$  represents the surface area of one nucleus and  $N$  represents the number of nuclei per cubic metre, whereas  $\frac{\pi}{4} D_{tube}^2$  represents the volume per unit length. Therefore, the vapour flux towards the particles in the tube per unit length can be defined as:

$$j'_{\alpha,p} = \frac{N d_p \text{Sh}(d_p) \phi \pi^2 D_{tube}^2 \mathbb{D} M_\alpha}{4 R_u T_g} (p_{\alpha,p} - p_{\alpha,g}). \quad (2.5)$$

Equation 2.5 is based on diffusion of molecules to the surface of the particle in the continuum limit. A correction factor  $\phi$  for diffusion outside the continuum regime is introduced while the dimensions of the particles are within the mean free path regime. In that case transport is controlled by kinetic processes. The effect of the correction factor  $\phi$  results in a slowing down of the growth rate and is given by the Dahneke equation, Seinfeld [41]:

$$\phi(\text{Kn}_d) = \frac{1 + \text{Kn}_d}{1 + 2\text{Kn}_d(1 + \text{Kn}_d)}, \quad (2.6)$$

where  $\text{Kn}_d$  is given by,

$$\text{Kn}_d = \frac{4\mathbb{D}}{d_p} \left( \frac{\pi M_\alpha}{8 R_u T_g} \right)^{\frac{1}{2}}. \quad (2.7)$$

Inertia effects can be neglected for particles in the sub-micrometre range (Fuchs [20]), implying that the particles follow the streamlines and the net flow around the particle is zero. Therefore, the Sherwood number  $\text{Sh}(d_p)$  as mentioned in Eq. 2.5 equals 2 in the case of small net mass-transfer rates and zero flow around a spherical particle.

In Eq. 2.5 it is assumed that the particle temperature equals the flue gas temperature. However, for a particle in a condensing atmosphere, particle heating takes place due to the release of latent heat of vaporisation during the condensation process. An equilibrium particle temperature is established when the energy necessary to heat up the particle is in balance with the heat loss due to conduction to the surrounding flue gas. The resulting quasi-static temperature between the particle and the surrounding flue gas  $T_p - T_g$  is given by Hinds [24]:

$$T_p - T_g = \frac{\mathbb{D} M_\alpha \mathcal{L} \phi}{R_u k_g} \left( \frac{p_{\alpha,p}}{T_p} - \frac{p_{\alpha,g}}{T_g} \right), \quad (2.8)$$

where  $k_g$  is the thermal conductivity of the surrounding flue gas. Assuming that potassium sulphate  $\text{K}_2\text{SO}_4$  is the main aerosol forming compound (see Sec. 3.3),  $\mathcal{L}$

represents the latent heat of vaporisation of  $K_2SO_4$ . Due to the temperature dependency of the saturation vapour pressure (see Fig.2.2) at the particle surface  $p_{\alpha,p}$  and the particle temperature itself  $T_p$ , Eq. 2.8 cannot be solved explicitly. Because of this, Eq. 2.8 is solved numerically. For the calculations a particle diameter  $d_p$  of typically  $0.1 \mu m$  is assumed in order to calculate the correction factor  $\phi$ . Figure 2.3 shows a graphical representation of  $T_p - T_g$  for various flue gas temperatures as a function of the saturation ratio  $S$ , assuming that  $K_2SO_4$  is the main aerosol forming compound. This saturation ratio, which is the ratio of the actual partial vapour pressure of the vapour in the flue gas to the saturation vapour pressure based on the flue gas temperature is defined as (Hinds [24]):

$$S = \frac{p_{\alpha,g}}{p_{\alpha,sat}}, \quad (2.9)$$

where  $p_{\alpha,g}$  represents the actual partial vapour pressure in the flue gas, whereas  $p_{\alpha,sat}$  represents the saturation vapour pressure evaluated on the flue gas temperature.

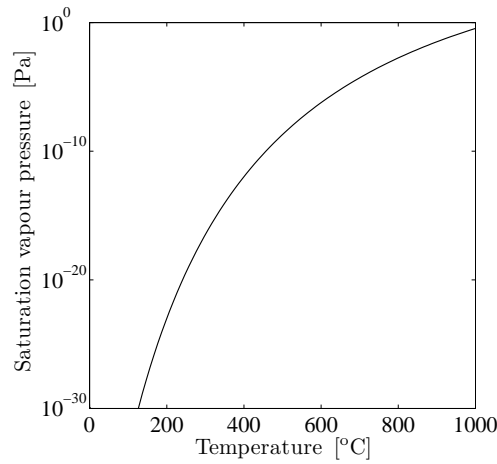


**Figure 2.2.** The saturation vapour pressure of  $K_2SO_4$  as function of temperature.

In Fig. 2.3 it can be observed that the difference between particle temperature and flue gas temperature depends on the flue gas temperature itself and the degree of saturation. During the growth process, the effect of the rising particle temperature results in an increase of the partial vapour pressure near the surface of the particle, which results in a slowing down of the net condensational growth rate. Because of this, the temperature difference between the particle and the surrounding flue gas is relatively small for a wide range of saturation ratios. A quantitative approach in the case of applying a saturation ratio of 10000 (which is extremely high) and a flue gas temperature of  $1000 \text{ }^\circ C$ , results in temperature difference  $T_p - T_g$  of less than  $3 \text{ }^\circ C$ , whereas the temperature difference for the same saturation ratio in the case of a flue gas temperature of  $800 \text{ }^\circ C$  results in an insignificant temperature difference between the particle and the surrounding flue gas. Therefore, the assumption that the particle



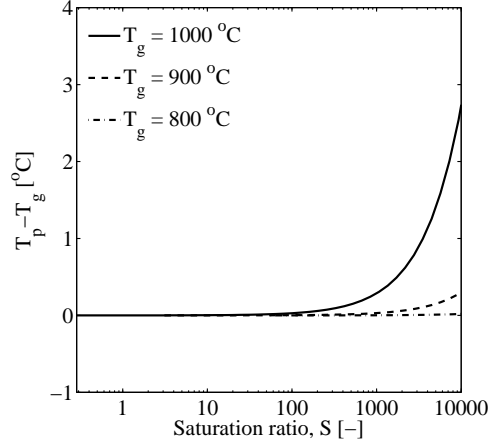


**Figure 2.3.** Particle temperature minus flue gas temperature ( $T_p - T_g$ ) versus saturation ratio  $S$  for flue gas temperatures of 800 - 1000  $^{\circ}\text{C}$ . Simulations are performed under the assumption that  $\text{K}_2\text{SO}_4$  is the main aerosol forming compound. The particle size during the simulation was always 0.1  $\mu\text{m}$ .

temperature equals the flue gas temperature for a wide range of flue gas temperatures as well as for a wide range of saturation ratios is plausible.

If wall condensation and heterogeneous condensation take place at the same moment and all other particle deposition mechanisms are neglected, the absolute wall condensation rate  $\varepsilon_{abs,theo}$  can be expressed as the ratio of the vapour flux towards the walls and the total vapour flux per unit length:

$$\varepsilon_{abs,theo} = \frac{j'_{\alpha,w}}{j'_{\alpha,w} + j'_{\alpha,p}}. \quad (2.10)$$

Using the fact that the particle temperature equals the flue gas temperature yields that  $p_{\alpha,p}$  equals the saturation pressure evaluated at flue gas temperature,  $p_{\alpha,sat}$ . Furthermore, the wall saturation ratio,  $S_{wall}$  is introduced and is defined as:

$$S_w = \frac{p_{\alpha,w}}{p_{\alpha,sat}}. \quad (2.11)$$

Substituting equations 2.3, 2.5, 2.9 and 2.11 into Eq. 2.10 and applying the previously described assumptions yields the following expression for the absolute wall condensation rate:

$$\varepsilon_{abs,theo} = \frac{\text{Sh}(D_{tube})(S_w - S)}{\text{Sh}(D_{tube})(S_w - S) + \frac{\pi}{4} D_{tube}^2 \phi \text{Sh}(d_p) N d_p (1 - S)}. \quad (2.12)$$

In Eq. 2.12,  $S_w$  is strongly depending on the wall temperature of the heat exchanger, which is always below the bulk temperature of the flue gas. This implies that, due to the strong temperature dependency of the vapour pressure of the aerosol forming

compound, the vapour pressure of the aerosol forming compound near the wall of a heat exchanger  $p_{\alpha,w}$  is always lower than the vapour pressure of the aerosol forming compound in the bulk of the flue gas. Therefore,  $S_w$  is always  $< 1$ . The other way around yields that the saturation ratio of the aerosol forming compound in the bulk of the flue gas is always significantly larger than one when assuming  $K_2SO_4$  as the main aerosol forming compound in order to establish particle condensation.

From Eq. 2.12 it can be observed that the absolute wall condensation rate strongly depends on the saturation ratio in the bulk  $S$  and near the wall  $S_w$ . Before investigating the influence of the saturation ratio  $S$  on the total wall condensation rate, the wall saturation ratio has to be determined. In the case of a water cooled heat exchanger it is assumed that the wall temperature of the heat exchanger equals the water temperature, which is much smaller than the flue gas temperature. Consequently the wall saturation ratio  $S_w$  in the region where wall condensation occurs goes to zero due to the strong temperature dependency of the saturation pressure of the aerosol forming species. In other words, when  $S_w \ll 1$ , the contribution of  $S_w$  can be neglected and Eq. 2.12 only depends on the saturation ratio  $S$ . This situation changes in the case that the wall temperature is slightly below the flue gas temperature, for instance when applying a gas to gas heat exchanger. However, the difference in the wall condensation rate for applying a wall saturation ratio  $S_w \approx 0.5$  instead of an wall condensation ratio  $S_w = 0$  is less than 10 % when a saturation ratio  $S = 1.5$  is assumed. Increasing the saturation ratio  $S$  rapidly gives that the influence of  $S_w$  can be neglected. Because of this several simulations have been performed for various saturation ratios  $S$  under the assumption that  $S_w = 0$ , see Fig. 2.4.

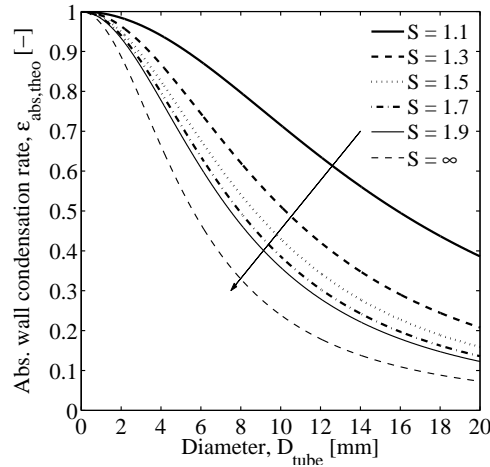


**Figure 2.4.** The effect the tube diameter  $D_{tube}$  on the absolute wall condensation rate,  $\varepsilon_{abs,theo}$  for various saturation ratios. Initial conditions:  $N = 1 \cdot 10^{13}$ ,  $d_p = 0.1 \mu m$  and  $S_w = 0$ .

In Fig. 2.4 two effects regarding the wall condensation rate can be observed. First of all decreasing the tube diameter to typically 2 mm results in a significant increase

of the wall condensation rate for all saturation ratios  $S$ . Consequently, decreasing the tube diameter results in a significant decrease of the particulate emissions at the heat exchanger outlet, which is the desired effect. Increasing the diameter has the consequence that condensation of aerosol forming vapours on pre-existing surfaces (particles) rapidly becomes the dominating process, thus increasing the particle mass emitted. Theoretically, an absolute wall condensation rate up to almost 90 % can be achieved by applying a tube diameter of approximately 2 mm. In principle also decreasing the saturation ratio slightly above 1 can result in a higher wall condensation ratio for large tube diameters. Theoretically, a wall condensation rate of 100 % could be achieved in the limit when  $S$  goes to 1. This means that there is no net cooling rate or driving force for condensation due to the fact that the wall saturation ratio  $S_w$  equals  $S$ , making this solution not practical.

## 2.3 Closure

An analytical approach incorporating heterogeneous- and wall condensation is derived to investigate whether there is a physical basis for preferential condensation of aerosol forming compounds on heat exchanger walls. Consequently, stimulating wall condensation results in fine particulate emission reductions to the atmosphere. Continuum diffusion of molecules towards already present nuclei in the flue gas in combination with a correction factor for diffusion outside the continuum limit is used in the approach.

The approach indicates a significant reduction of aerosol emissions by preference of wall condensation when sufficient heat exchanging area is provided, the distance to the wall in every cross section is in the millimetre range and the flow regime is laminar. Theoretically, a wall condensation rate of 100 % could be achieved in the limit of an infinite small tube diameter or in the limit when the saturation ratio  $S$  goes to 1. It is noticed that these two conditions are hypothetical because an infinitely small tube diameter is from a practical point of view not suitable, whereas a saturation ratio equal to 1 implies that no heat is transferred. However, applying tube dimensions of approximately 2 mm results in a wall condensation rate up to almost 90 %, which is a significant reduction. So it is proven that a fundamental basis for aerosol forming vapour condensation on heat exchanger surfaces exists.

Experiments with narrow channeled heat exchanger designs in the order of a couple of millimetres are required to prove whether such small tube dimensions indeed result in significant aerosol reductions in real-scale applications. Furthermore, the influence of particle formation and particle deposition has to be investigated to determine its influence on the fine particulate emission reduction. Besides this, also the applicability of such heat exchanger dimensions for small-scale biomass combustion systems has to be investigated. Blocking of the flue gas channel, for instance with coarse fly ash particles, could limit the practical applicability.

## Chapter 3

# Plug flow model with particle formation in a heat exchanger

### 3.1 Introduction

In chapter 2 and in De Best et al. [14] it is derived that for sufficiently small heat exchanger passages wall condensation dominates over heterogeneous condensation. Besides decreasing the tube diameter also the influence of the saturation ratio is investigated. Decreasing the saturation ratio results in an increase of the wall condensation rate if only wall condensation and heterogeneous condensation are considered. The other way around yields that increasing the saturation ratio, results in a slowing down of the wall condensation rate and in an increase of the condensation rate on already existing particles. Besides this, also another process can become important while increasing the saturation ratio. From literature it is known that increasing the saturation ratio results in an increasing possibility for particle formation, the so called homogeneous nucleation process [2]. This process also have a negative effect on the wall condensation rate. The more particles are formed by nucleation the more surface area is provided for condensation and therefore wall condensation becomes of minor importance. Therefore, a more detailed model including particle formation has been derived to investigate the interaction of the particle formation process and the wall condensation process. The numerical code is implemented in MATLAB ®.

Researchers like Pyykönen and Jöller et al. [35, 30] both derived models to investigate the particle formation process in biomass combustion plants equipped with ordinary boiler designs, which operate in the turbulent regime. One aim of their models was to compare the predicted particle size distribution (PSD) with experimentally obtained PSD's. Therefore, it was necessary to incorporate particle deposition mechanisms as well as vapour deposition mechanisms. Contrary to their efforts, the focus of this research is on the wall condensation mechanism and how this mechanism may be stimulated.

Jensen et al. [28] describe a model regarding the particle formation process during cooling of a synthetic flue gas containing sodium and potassium chloride vapours in

a tubular reactor with laminar flow. The model includes nucleation of particles, as well as condensation of aerosol forming vapours on the reactor walls and the particles formed. Using a prescribed wall temperature profile and volume flow rate, wall condensation ratios between 60 - 80 % could be observed depending on the conditions applied. From the results it could also be observed that slight variations in the wall temperature profile rapidly result in different wall condensation rates. However, no explanation is given for this trend. So besides the influence of the tube diameter as mentioned in chapter 2 it seems likely that the temperature gradient of the flue gas in the heat exchanger passage also influences the wall condensation rate. Therefore, the model developed should provide a fundamental basis with respect to the trend that decreasing the temperature gradient in a heat exchanger passage should result in an increasing wall condensation rate. When a fundamental basis exists, this phenomenon can be enhanced to stimulate condensation of aerosol forming vapours on heat exchanger surfaces.

## 3.2 Aerosol formation process

In fixed-bed biomass combustion process the aerosol formation process follows a basic scheme (see, Fig. 1.2), already described in Sec.1.2. In this section, a more detailed description is provided.

### Release of aerosol forming compounds

As already mentioned in the introduction, the biomass combustion process involves drying of the fuel, pyrolysis and gasification, followed by charcoal burnout. During these processes, easily volatile aerosol forming compounds containing K, Na, S and Cl as well as heavy metals like Pb and Zn are partly released from the fuel to the flue gas. From the fuel analyses in Tab. 1.1, it can be observed that K and S are the most important aerosol forming elements for chemically untreated wood chips.

As mentioned in Brunner [9], detailed interactions between the fuel composition and release of the aerosol forming elements from the fuel are still uncertain. However, thermochemical equilibrium calculations indicate that at reducing conditions alkaline metals like K and Na are released as hydroxides and chlorides. Under oxidising conditions, K is mainly released as  $K_2SO_4$  and KCl.

Concerning the heavy metals it is known that Pb can be released as elemental Pb or PbS at reducing conditions. Under oxidising conditions, Pb is mainly formed as PbO and  $PbCl_2$ , depending on the chlorine concentration. Zn can be released either as elemental Zn (under reducing conditions) or as  $ZnCl_2$  (if high chlorine concentrations are available, which is usually not the case during the combustion of chemically untreated wood chips). Under oxidising conditions outside the fuel bed, elemental Zn is oxidised, leading to the formation of ZnO. Moreover, small amounts of non volatile elements (Ca, Si and Mg) can be released to the flue gas as sub-micron particles due to different processes (see Brunner [9]).

However, aerosol forming elements in the fuel are not fully released to the flue gas and therefore a direct determination of the ash vapour concentrations and com-

positions in the furnace is not possible. Therefore, release factors describing the rate per element released to the flue gas have been applied to estimate the concentrations of aerosol forming compounds in the flue gas. The release factors used to estimate the flue gas composition and consequently also the aerosol composition strongly depend on the combustion temperature applied [18]. Based on combustion temperatures around 1000 °C the following release factors can be found in literature for the relevant aerosol forming elements, see Tab. 3.1.

**Table 3.1.** Release factors of aerosol forming elements at combustion temperatures around 1000 °C used for gas to particle conversion calculations.

element	release factor [%]	literature data
S	80	[31, 55, 29, 18]
Cl	90	[31, 55, 29, 18]
K	40	[31, 18]
Na	30	[31, 18]
Zn	80	[31, 55, 29, 18]
Pb	90	[31, 55, 29, 18]

### Homogeneous nucleation of ZnO

As already mentioned, Zn is only volatile at reducing conditions. When the atmosphere changes from a reducing condition to an oxidising condition, ZnO is formed. Due to the low saturation vapour pressure of ZnO, ZnO nucleates very rapidly. Because of this, ZnO particles can be formed immediately above the fuel bed. Later on, these ZnO particles grow due to condensation or coagulation.

### Chemical reactions of released inorganic compounds

In the furnace and in the boiler, inorganic species released from the fuel to the flue gas undergo chemical reactions. K is most probably released as KOH and KCl. KOH can react by both SO<sub>3</sub> and CO<sub>2</sub>, whereas KCl can react with SO<sub>3</sub>. It is noticed that the transformation from SO<sub>2</sub> to SO<sub>3</sub>, is chemically limited during biomass combustion. Consequently, not all KOH and KCl can be sulphated, even when the SO<sub>2</sub> concentration is high enough. Depending on the concentrations, a part of the KCl, together with the SO<sub>3</sub> will form K<sub>2</sub>SO<sub>4</sub>. Consequently, a part of the gaseous KCl condenses, resulting in solid KCl particles. The KOH that reacts with CO<sub>2</sub> will form K<sub>2</sub>CO<sub>3</sub>.

### Coagulation of already formed particles

As already mentioned, ZnO particles that are immediately formed above the fuel bed can coagulated, reducing the number concentration of particles. Besides coagulation between ZnO particles only, also coagulation between ash forming compounds like CaO, SiO<sub>2</sub> and MgO particles can occur. It is noticed that the particle formation

process of these ash forming compounds is not discussed in detail in this work, since they only provide almost negligible contributions to the aerosol emissions.

### Homogeneous nucleation and condensation of aerosol forming compounds and further coagulation

The biomass composition as depicted in Tab. 1.1 indicates that during the combustion of chemically untreated wood chips aerosols mainly consist of  $K_2SO_4$ ,  $KCl$  and some small amounts of  $K_2CO_3$  and heavy metals are formed.

Homogeneous nucleation or condensation of  $K_2SO_4$  can occur when the saturation ratio, as defined in Eq. 2.9, of this particular compound is high enough. Compared to  $KCl$ , the saturation vapour pressure of  $K_2SO_4$  is rather low, resulting that  $K_2SO_4$  can already nucleate/condense at higher temperatures ( $\approx 1000$  °C) at typical vapour phase concentrations during wood chips combustion. In Fig. 2.2, the saturation vapour pressure of  $K_2SO_4$  is depicted as a function of temperature.

As the  $K_2SO_4$  concentration in the flue gas is that high, formation of particles by homogeneous nucleation and consequently condensation can already occur before the flue gas enters the convective path.

## 3.3 Modeling approach

A plug flow model describing the particle formation process as well as the condensation processes in narrow channeled heat exchangers is developed. Using a plug flow approach implies that radial effects are neglected in the model presented.

As current firetube boiler designs exhibit round tubes, simulations are subjected to this geometry. Enforcing a wall temperature profile, as described in Jensen et al. [28], was possible by varying the heat resistance towards the cooling medium. In ordinary firetube boilers, the outer side of the firetubes are surrounded by cooling water. However, during the simulations it is assumed that these tubes are covered with insulation material around which cooling water flows, see Fig. 3.1. In this way the heat resistance could easily be varied by applying more or less insulation material. A major consequence of applying insulation material is that the heat transfer is reduced, resulting in an increase of the heat exchanging surface area required for heat transfer. The thickness of the insulation material, which is equal to  $R_3 - R_2$ , is varied between 0 and 10 mm, whereas the thermal conductivity of the insulation material is taken to be  $0.05 \frac{W}{(m \cdot K)}$ . Besides varying the insulation thickness the inner radius,  $R_1$ , is varied from 0.5 to 5 mm. The thickness of the tubing material,  $R_2 - R_1$ , during the simulations remained constant at 2 mm, whereas the thermal conductivity of the tubing material is equal to that of steel, that is typically  $50 \frac{W}{(m \cdot K)}$ .

In order to reduce the number of equations required, some simplifications have to be made. First of all the flow is assumed to be laminar and fully developed, which is reasonably valid for small tube dimensions. Furthermore, it is assumed that the flue gas is already polluted with very small particles, originating from gas to particle conversion mechanisms inside the furnace. The total number concentration of particles near the heat exchanger inlet is assumed to be on the order of  $1 \cdot 10^{13} Nm^{-3}$ .

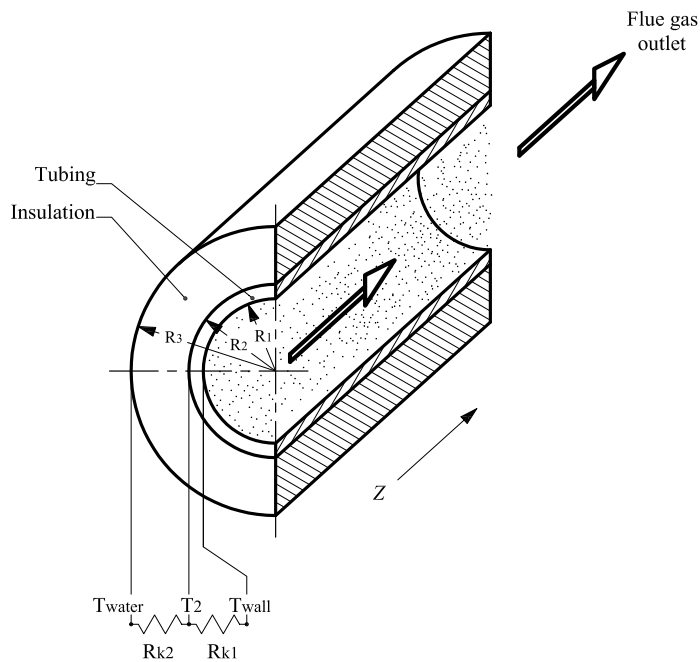


**Figure 3.1.** Schematic representation of a tube with insulation.

The basis for this assumption is supported by the fact that measurements regarding the aerosol concentration downstream hot water boilers have revealed that the total number concentration was usually in that order, see Brunner et. al [10]. It is expected that the number concentration of aerosols during the cooling process in ordinary hot water boilers does not change significantly, which can be attributed to coagulation processes. Small particles that are formed in the furnace due to gas to particle conversion mechanisms are assumed to be formed in large numbers. On their way in the flue gas, coagulation processes are able to reduce these numbers. The initial number concentration and the time available for coagulation mainly determine the final number concentration. As already mentioned in Sec. 2.2, a conservative estimation for the time available for coagulation in the furnace is one second. As a result of the limited time available for coagulation, the resulting final particles number concentration before entering the heat exchanger is approximately  $1 \cdot 10^{13} Nm^{-3}$ , even for significantly higher initial number concentrations. Furthermore, it is assumed that in common firetube boilers particle formation by nucleation is widely suppressed due to the high aerosol concentration near the heat exchanger inlet.

Constant flue gas temperatures and flue gas compositions near the inlet of the heat exchanger are assumed for all simulations. The cooling water temperature is assumed to be constant throughout the whole heat exchanger, e.g. as if the mass capacity flow ( $\dot{m}c_p$ ) of cooling water is much larger compared to the mass capacity flow of the flue gas. Using this assumption also implies that the heat exchanger material that



is directly in contact with cooling water is in first order approximation equal to the cooling water temperature. Typical cooling water temperatures in firetube boilers are around  $90\text{ }^{\circ}\text{C}$  at boiler outlet, whereas the flue gas temperature at boiler outlet is typically  $150\text{ }^{\circ}\text{C}$ . From experiments performed with several aerosol condensing heat exchangers at high flue gas temperatures, it could be observed that the time average combustion temperature in the furnace is around  $1030\text{ }^{\circ}\text{C}$ , see Fig. 6.7 and 6.19. Because of this, simulations are subjected to initial flue gas temperatures of around  $1030\text{ }^{\circ}\text{C}$ .

As already described in Sec. 3.2, aerosol formation and growth is a complicated process involving gas phase reactions, homogeneous nucleation and condensation of aerosol forming vapours and coagulation of existing particles. Because of this, it is useful to make simplifications to arrive at a plug flow model describing the most important trends.

One possibility to reduce the number of equations is to assume one aerosol forming compound only. The big advantage of considering one aerosol forming compound only is that chemical equilibrium calculations required for a multi-component system can be excluded from the analysis. To assure whether such simplification is permitted, it is necessary to investigate the chemical composition of the aerosol forming compounds. When analysis show that there is one dominant aerosol forming compound in the flue gas, that specific compound can act as a compound, covering the whole range of aerosol forming vapours.

Therefore, the flue gas composition and consequently also the chemical composition of the aerosols is estimated, based on the fuel composition as described in Tab. 1.1 and release factors as described in Tab. 3.1. All estimated concentrations are related to dry flue gas  $13\text{ vol\% } O_2$ . Calculations show that the alkaline sulphate concentration in the flue gas is expected to amount to  $44\text{ mg/Nm}^3$ , whereas the alkaline chloride concentration is expected to be  $13\text{ mg/Nm}^3$ . Because all potassium is already consumed by either S and Cl, yields that no alkaline carbonates are formed. Regarding the heavy metal content, it can be observed that its share is rather low. The concentrations PbO and ZnO are expected to amount to respectively 2 and  $1\text{ mg/Nm}^3$ .

From this analysis it can be derived that the total estimated concentration of aerosol forming compounds in the flue gas amounts to approximately  $60\text{ mg/Nm}^3$ . The concentration of alkaline sulphates amounts to  $44\text{ mg/Nm}^3$ , which is more than  $70\text{ wt.}\%$ . Due to this significant share of  $K_2SO_4$ , it is in first order approximation allowed to assume that the calculations can be subjected to an aerosol concentration of  $60\text{ mg/Nm}^3$ , consisting of  $K_2SO_4$  only. Since  $K_2SO_4$  is a compound that is rather sensitive to nucleation even at high flue gas temperatures yields that the results obtained are a worst case estimation.

Furthermore, it is supposed that the vapour pressure near the entrance of the heat exchanger is in an equilibrium state, i.e. the saturation ratio  $S \leq 1$ . However, the use of an initial flue gas temperature of  $1030\text{ }^{\circ}\text{C}$  in combination with a concentration of aerosol forming compounds released from the fuel to the flue gas,  $\rho_{\alpha,rel}$ , of  $60\text{ mg/Nm}^3$  consisting of  $K_2SO_4$  only yields that the saturation ratio  $S > 1$ . To make sure that the vapour pressure is in an equilibrium state, the excess of vapour in the flue gas in

the furnace is supposed to be transformed into solid particles, such that the saturation ratio  $S = 1$ . It is assumed that these particles exhibit a lognormal distribution before they enter the convective path. This lognormal distribution is given by Hinds [24]:

$$N(d_p) = \frac{N_{norm,ini}}{\ln \sigma_{g,ini} \sqrt{2\pi}} \left[ -\frac{(\ln d_p - \ln \text{GMD}_{ini})^2}{2 \ln^2 \sigma_{g,ini}} \right]. \quad (3.1)$$

In Eq. 3.1,  $N_{norm,ini}$  represents the total initial particle number concentration that amounts to  $1 \cdot 10^{13} \text{ Nm}^{-3}$ . The terms  $\text{GMD}_{ini}$  and  $\sigma_{g,ini}$  represent respectively the initial geometric mean diameter (GMD) and the geometric standard deviation. The geometric mean diameter is defined as:

$$\text{GMD} = \exp \left[ \frac{1}{\sum N_i} \sum N_i \ln d_{p,i} \right] \quad (3.2)$$

where  $N_i$  is the number concentration of particles with a specific diameter  $d_{p,i}$ .

Considering the deviation in particle sizes, three classification regarding the size distributions can be distinguished. According to VDI-guideline 3491, page 1, aerosols are divided as follows:

- $\sigma_g < 1.15$  monodisperse
- $1.15 \leq \sigma_g < 1.5$  quasimonodisperse
- $\sigma_g \geq 1.5$  polydisperse

As combustion particles from biomass combustion exhibit a polydisperse distribution, a typical geometric standard deviation of 1.6 is assumed. The GMD is chosen in such a way that the initial particle concentration near the heat exchanger inlet  $\rho_{part,ini}$  exhibits a lognormal particle size distribution equal to the excess of aerosol forming vapour that is transformed into particles. Based on the saturation vapour pressure curve, the maximum concentration of potassium sulphate in gaseous state at a temperature of 1030 °C is 51 mg/Nm<sup>3</sup>. Consequently, approximately 9 mg/Nm<sup>3</sup> of vapour should already be transformed into solid particles. In order to satisfy all previous conditions, the resulting geometric mean diameter should be equal to 62 nm.

In Tab. 3.2 all relevant input parameters required for the simulations are summarised.

**Table 3.2.** Overview of the input parameters required of the simulations

Tube radius, $R_1$	0.5-5 mm
Thickness tubing material, $R_2 - R_1$	2 mm
Thickness insulation material, $R_3 - R_2$	0-10 mm
Thermal conductivity tubing material, $k_{tube}$	50 W/(m · K)
Thermal conductivity insulation material, $k_{iso}$	0.05 W/(m · K)
Flue gas temperature at heat exchanger inlet, $T_{g,ini}$	1030 °C
Flue gas temperature at heat exchanger outlet, $T_{g,out}$	≈ 150 °C
Cooling water temperature, $T_{water}$	90 °C
Flue gas velocity at inlet, $v_{ini}$ (unless stated otherwise)	1 m/s
Aerosol forming compound, $\alpha$	K <sub>2</sub> SO <sub>4</sub>
Initial particle number concentration, $N_{norm,ini}$	$1 \cdot 10^{13} Nm^{-3}$
Initial Geometric Mean Diameter, $GMD_{ini}$	62 nm
Initial Geometric Standard Deviation, $\sigma_{g,ini}$	1.6
Saturation ratio near heat exchanger inlet $S$	≤ 1
concentration aerosol forming vapour released to the flue gas, $\rho_{\alpha,rel}$	60 mg/Nm <sup>3</sup>

### 3.4 Aerosol dynamics

During aerosol formation several mechanisms can be distinguished that cause formation of new particles (homogeneous nucleation) and growth of particles (heterogeneous condensation and coagulation). Besides this, also direct condensation of aerosol forming vapours on surfaces in the vicinity could occur e.g. wall condensation. A tool which is often used in order to determine the dynamics of the particle formation process is the General Dynamic Equation (GDE), describing the change of the particle population over the time. According to Friedlander [19] this GDE is given by:

$$\frac{\partial N_k}{\partial t} + \nabla \cdot N_k v = \left[ \frac{\partial N_k}{\partial t} \right]_{growth} + J_k + \left[ \frac{\partial N_k}{\partial t} \right]_{coag} + \nabla \cdot \mathbb{D}_p \nabla N_k - \nabla \cdot v_p N_k \quad (3.3)$$

In the equation above, the first three terms on the right hand side are source and sink terms for a specific size class  $k$ , whereas the remaining terms are transport terms. In Eq. 3.3,  $\frac{\partial N_k}{\partial t}$  represents the time dependent change of the number concentration of particles of a specific size class  $k$ , whereas the diffusion coefficient  $\mathbb{D}_p$  is a function of the particle size. In contrast to heterogeneous condensation, coagulation only modifies the size distribution of an aerosol, without change of the mass concentration. The flue gas velocity is represented by  $v$ , whereas  $v_p$  is the relative particle velocity resulting

from an external force field e.g. thermophoresis or electrostatic forces. The subscripts *growth* and *coag* represent the change in number concentration of a specific size class due to respectively heterogenous condensation and coagulation, whereas the term  $J$  represents the formation of new particles within the size class  $k$ .

### 3.4.1 Homogeneous nucleation

A vapour is in a supersaturated state when its partial vapour pressure,  $p_{\alpha,g}$ , is larger than its saturation vapour pressure,  $p_{\alpha,sat}$ . In this situation, two routes are open for the system to return to equilibrium; via homogeneous nucleation and condensation on (pre-existing) surfaces. The non-equilibrium parameter for an ideal vapour is the saturation ratio  $S$ , defined as:

$$S = \frac{p_{\alpha,g}}{p_{\alpha,sat}} \quad (3.4)$$

In Eq. 3.4,  $p$  represents the partial vapour pressure of the aerosol forming vapour  $\alpha$ . For the simulations performed  $\alpha$  is equal to potassium sulphate, whereas the subscripts *sat* and *g* represents respectively the saturation vapour pressure and the saturation pressure in the bulk. Expressions describing the homogeneous nucleation rate  $J = J(T_g, S)$  depending on temperature  $T_g$  and saturation ratio  $S$  are of the form (Friedlander [19]):

$$J(T_g, S) = K \exp\left(\frac{-\Delta G^*}{k_b T_g}\right), \quad (3.5)$$

where  $k_b$  denotes the Boltzmann constant and  $\Delta G^*$  the change in Gibbs free energy. For  $S > 1$ , the term  $-\Delta G^*/(k_b T_g)$  exhibits a maximum:

$$\frac{-\Delta G^*}{k_b T_g} = \frac{-16\pi}{3} \frac{\hat{v}_{ml}^2 \sigma^3}{(k_b T_g) \ln(S)^2}, \quad (3.6)$$

where  $\hat{v}_{ml}$  is the molecular volume of the condensing component, while  $\sigma$  represents the surface tension. The kinetic prefactor,  $K$ , is according to *Classical Nucleation Theory*:

$$K_{CNT} = S \frac{p_{\alpha,sat}^2}{(k_b T_g)^2} \hat{v}_{ml}^2 \left(\frac{2\sigma}{\pi m}\right)^{\frac{1}{2}}, \quad (3.7)$$

where  $m$  is the mass of one vapour molecule. An estimation of the particle dependent surface tension is given by the Tolman equation (Vogelsberger [52]), which is of a semi-empirical nature:

$$\sigma = \sigma_\infty \left(1 + \frac{4\delta}{d_p}\right)^{-1}, \quad (3.8)$$

where  $\sigma_\infty$  is the macroscopic surface tension of a plane surface and  $\delta$  is the Tolman length. However, the use of the Tolman equation in nucleation models is still a topic of discussion (Pykönen [35]). An estimation for the Tolman length from molecular

dynamics simulations of a Lennard-Jones liquid vapour interface is  $\delta = \sigma_{LJ,\alpha}\zeta$ , where  $\sigma_{LJ,\alpha}$  is the Lennard-Jones characteristic length of aerosol forming component  $\alpha$ , whereas  $\zeta$  is the dimensionless Tolman length proposed by Haye et al. [21], which equals 0.2.

The size of the new born particles can be determined by invoking the Kelvin equation [24]:

$$\frac{p_{\alpha,p}^{eq}}{p_{\alpha,sat}} = \exp\left(\frac{4\sigma\hat{v}_{ml}^2}{k_b T_g d_p}\right) = \exp(\text{Ke}), \quad (3.9)$$

where  $p_{\alpha,sat}$  denotes the saturation vapour pressure of the condensing compound for a plane surface at a given temperature and  $p_{\alpha,p}^{eq}$  for a curved plane. For a given uniform vapour pressure,  $p_{\alpha,g} > p_{\alpha,sat}$ , and for a cloud of aerosols with a wide range of sizes, there exists a metastable equilibrium for one particular droplet size such that  $p_{\alpha,g} = p_{\alpha,p}^{eq} = Sp_{\alpha,sat}$ . Substitution of this relation together with the Tolman equation in the Kelvin equation (3.9) yields a relation for the critical or Kelvin diameter:

$$d_p^* = \frac{4\sigma_\infty\hat{v}_{ml}^2}{k_b T_g \ln(S)} - 4\delta, \quad (3.10)$$

### 3.4.2 Heterogeneous condensation

The radial growth rate of aerosol forming vapours on already present nuclei in the flue gas as well as on new particles formed by homogeneous nucleation is given by (Hinds [24]):

$$\frac{\partial d_p}{\partial t} = F(\text{Kn}_d) \frac{4\mathbb{D}M_\alpha}{R_u T_g d_p \rho_{\alpha,p}} (p_{\alpha,g} - p_{\alpha,p}^{eq}), \quad (3.11)$$

where  $\mathbb{D}$  represents the diffusion coefficient, calculated according to Chapman-Enskog's kinetic theory.  $M_\alpha$  and  $\rho_{\alpha,p}$  represent the molar mass and the density of the condensed phase of the aerosol forming vapour, while  $R_u$  represents the universal gas constant and  $d_p$  is the particle diameter. The partial vapour pressure of the compound  $p_{\alpha,g}$  is the vapour pressure far away from the aerosol, while  $p_{\alpha,p}^{eq}$  indicates the vapour pressure on the surface of the aerosol, which is calculated according to the Kelvin equation, see Eq. 3.9. Equation 3.11 is based on diffusion of molecules to the surface of the particle. However, the new particles formed by homogeneous nucleation have dimensions which are usually within the free molecular regime. Because of this a correction term for diffusion outside the continuum regime has been applied, indicated by the correction term  $F(\text{Kn}_d)$ . This correction term results in a slowing down of the growth rate and is given by the Dahneke equation, Seinfeld [41],

$$F(\text{Kn}_d) = \frac{1 + \text{Kn}_d}{1 + 2\text{Kn}_d(1 + \text{Kn}_d)}, \quad (3.12)$$

where the Knudsen number  $\text{Kn}_d$  is given by

$$\text{Kn}_d = \frac{\mathbb{D}}{d_p} \left( \frac{M_\alpha \pi}{2R_u T_g} \right)^{\frac{1}{2}}. \quad (3.13)$$

### 3.4.3 Coagulation

When particles are generated by homogeneous nucleation, the possibility that these particles collide with already formed particles increases with the number concentration. As a result of this coagulation process, the number concentration of particles decreases. Because mass of particles is conserved, the average size of the particles should increase. Because of this, coagulation influences the particle growth process and consequently also the competing process of wall condensation.

Smoluchowski [42] developed a relation to predict the effect of coagulation on the particle size distribution equal to:

$$\frac{dN(m_p, t)}{dt} = \frac{1}{2} \int_0^{m_p} K_{12}(m, (m_p - m)) N(m) N(m_p - m) dm - \int_0^{m_p} K_{12}(m_p, m) N(m_p) N(m) dm \quad (3.14)$$

where  $\frac{dN(m_p, t)}{dt}$  represents the change of the number concentration with mass  $m_p$  as a function of time. The first term on the RHS is the increase in the number of particles of mass  $m_p$ , due to those formed from smaller ones. The second term on the RHS is the decrease of particles with mass  $m_p$  of due to coagulation with other particles. In Eq. 3.14  $K_{12}$  represents the abbreviated notation for the collision frequency function between the colliding particles having masses  $m_{p1}$  and  $m_{p2}$ . In the model described only Brownian coagulation is considered. Gravitational settling which could influence the collision frequency function as well is not taken into account due to the relatively small particle dimensions. Without gravitational settling, the particle collision frequency can be described as (Fuchs [20]):

$$K(d_{p1}, d_{p2}) = 2\pi(d_{p1} + d_{p2})(\mathbb{D}_{p1} + \mathbb{D}_{p2})\beta \quad (3.15)$$

where  $d_{p1}$  and  $d_{p2}$  are the colliding diameters, whereas  $\beta$  expresses the transition from diffusive to gas-kinetic coagulation regime. Figure 3.2 is a graphical representation of Eq. 3.15, showing that the maximum collision frequency for typical aerosol particles in the relevant size range between 1 nm and 0.1  $\mu m$  is at maximum  $K_{12} \approx 10^{-13}$ , using combustion temperatures around 1000 °C. The correction factor  $\beta$  as described in Eq. 3.15 is defined as (Fuchs [20]):

$$\beta = \left[ \frac{d_{p1} + d_{p2}}{d_{p1} + d_{p2} + 2g_{12}} + \frac{8(\mathbb{D}_{p1} + \mathbb{D}_{p2})}{\bar{c}_{12}(d_{p1} + d_{p2})} \right]^{-1} \quad (3.16)$$

where  $g_{12}$  is the mean distance from the surface of the sphere which is reached by the particles after covering a distance  $l_i$ , defined as (Fuchs [20]):

$$g_{12} = (g_1^2 + g_2^2)^{\frac{1}{2}}, \quad g_i = \frac{(d_{pi} + l_i)^3 - (d_{pi}^2 + l_i^2)^{\frac{2}{3}}}{3d_{pi}l_i} - d_{pi},$$

$$l_i = \frac{8\mathbb{D}_{pi}}{\pi\bar{c}_i}, \quad i = 1, 2 \quad (3.17)$$

The mean thermal velocity of the motion of a particle,  $\overline{c_{12}}$  is defined as (Hinds[24]):

$$\overline{c_{12}} = (\overline{c_1^2} + \overline{c_2^2})^{\frac{1}{2}} \quad \overline{c_i} = \left( \frac{48k_b T_g}{\pi^2 d_{pi}^3 \rho_p} \right)^{\frac{1}{2}}, \quad i = 1, 2 \quad (3.18)$$

The Stokes-Einstein equation is used to calculate the particle diffusion coefficient  $\mathbb{D}_p$  (Hinds[24]):

$$\mathbb{D}_p = \frac{k_b T_g C_c}{3\pi \mu_g d_p} \quad (3.19)$$

where  $C_c$  is the Cunningham correction factor and  $\mu_g$  is the dynamic viscosity of the flue gas. An empirically determined equation for the Cunningham correction factor for solid particles smaller than  $0.1 \mu m$  is given by Allen et al. [1]:

$$C_c = 1 + \text{Kn} \left[ 1.170 + 0.525 \exp \left( \frac{-0.780}{\text{Kn}} \right) \right] \quad (3.20)$$

The Knudsen number Kn is defined as:

$$\text{Kn} = \frac{2\lambda_g}{d_p} \quad (3.21)$$

where  $\lambda_g$  is the mean free path related to the kinematic viscosity:

$$\lambda_g = \frac{\mu_g}{\rho_g} \left( \frac{M_g \pi}{2R_u T_g} \right)^{\frac{1}{2}} \quad (3.22)$$

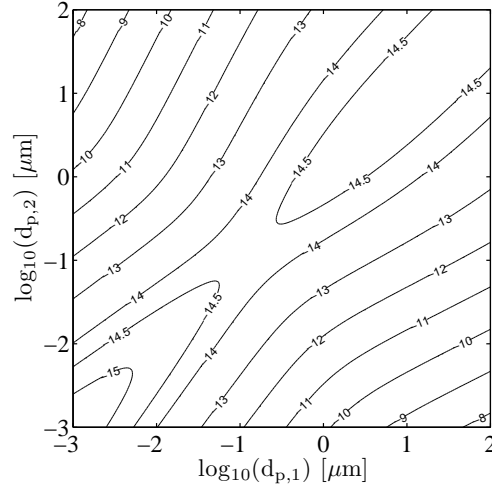


**Figure 3.2.** Collision frequency  $-\log_{10}(K_{12}) \left[ \frac{m^3}{s} \right]$  at a flue gas temperature of  $1000 \text{ } ^\circ C$

### 3.5 Total change of vapour pressure

The total change of the partial vapour pressure of a component due to gas to particle conversion as a function of the axial position in a heat exchanger passage can be divided in two parts. One part is caused by the formation and growth process of the aerosol particles,  $\frac{\partial p_{\alpha,part}}{\partial z}$ , and the other part is caused by the condensation process of aerosol forming vapours on the walls of a heat exchanger,  $\frac{\partial p_{\alpha,wall}}{\partial z}$ . So the change of the total vapour pressure can be written as:

$$\frac{\partial p_{\alpha,g}}{\partial z} = \frac{\partial p_{\alpha,part}}{\partial z} + \frac{\partial p_{\alpha,wall}}{\partial z} \quad (3.23)$$

#### 3.5.1 Change of vapour pressure due to particle formation and growth

The change of the mass density of the particles per unit volume due to condensation and homogeneous nucleation is denoted by  $\frac{d\rho_{part}}{dt}$ , and given by:

$$\frac{d\rho_{part}}{dt} = \frac{M_g}{M_\alpha} \sum_{d_p=0}^{d_p=\infty} \rho_{\alpha,p} N \pi d_p^2 \frac{\partial d_p}{\partial t} + \frac{M_g}{M_\alpha} \frac{\pi}{6} d_p^{*3} \rho_{\alpha,p} J, \quad (3.24)$$

where the first part on the RHS of Eq. 3.24 represents the change of mass density of aerosols due to growth, whereas the second part of the the RHS of Eq. 3.24 describes the change of mass density of aerosols due to homogeneous nucleation. In Eq. 3.24  $N$  is the number concentration of particles per unit volume having diameters in the size class between  $d_p$  and  $d_p + dd_p$ . The mass density change of the particle per unit time  $\frac{d\rho_{part}}{dt}$  is positive in the case of condensation, consequently the change of the partial vapour pressure is negative due to this process. The resulting vapour pressure change per unit length due to particle formation and growth  $\frac{\partial p_{\alpha,part}}{\partial z}$  is given by:

$$\frac{\partial p_{\alpha,part}}{\partial z} = -\frac{p_{tot}}{v\rho_g} \frac{d\rho_{part}}{dt}, \quad (3.25)$$

where  $p_{tot}$  represents the total pressure and  $v$  is the axial bulk velocity.

#### 3.5.2 Change of vapour pressure due to wall condensation

When axial diffusion inside the flue gas is neglected with respect to axial convection and radial diffusion, the change of the partial vapour pressure due to wall condensation,  $\frac{\partial p_{\alpha,wall}}{\partial z}$  can be described as (Bird et al. [6]):

$$\frac{\partial p_{\alpha,wall}}{\partial z} = \frac{4Sh\mathbb{D}}{D_{tube}v} (p_{\alpha,wall} - p_{\alpha,g}) \quad (3.26)$$

In Eq. 3.26,  $D_{tube}$  represents the tube diameter. The partial vapour pressure at the wall of the heat exchanger is denoted by  $p_{\alpha,wall}$ . The Sherwood number,  $Sh$ , is a dimensionless number required to calculate the mass-transfer rate. This number represents the ratio of the length scale (in this case the tube diameter,  $D_{tube}$ ) to the



diffuse boundary layer thickness. Analogy between heat and mass transfer is used to determine the Sherwood number. Since a fully developed laminar flow is assumed, the Nusselt number and consequently also the Sherwood number is constant at 3.66, see Bird et al. [6].

### 3.6 Change of flue gas temperature

Regarding the energy equation, two processes can be distinguished. First of all radial conduction towards the walls of the heat exchanger and secondly the latent heat release due to condensation. In the analysis presented it is assumed that axial conduction can be neglected compared to radial conduction, so the resulting energy equation has the following form (Bird [6]):

$$\frac{\partial T_g}{\partial z} = \frac{-4U}{D_{tube} v \rho_g c_p} (T_g - T_{water}) - \frac{\Delta H}{v \rho_g c_p} \frac{d\rho_{part}}{dt}, \quad (3.27)$$

where  $c_p$  and  $\rho_g$  are respectively the heat capacity and the density of the gas, whereas  $U$  represents the overall heat transfer coefficient. The product  $\Delta H \frac{d\rho_{part}}{dt}$  represents the energy release per unit volume due to condensation, where  $\Delta H$  represents the latent heat release. For the model presented it is assumed that the heat exchanger consists of a cylindrical tube surrounded by insulation material, see Fig. 3.1. Because the convective heat resistance over the cooling water and the insulation material is much larger than the combined heat resistance over the insulation material, tubing material and convective heat resistance between the flue gas and the tube, it is plausible that the insulation material on the cooling water side has the cooling water temperature. So the overall heat transfer coefficient can be expressed as (Janna [27]):

$$U = \frac{1}{\frac{1}{h} + \frac{R_1 \ln(R_2/R_1)}{k_{tube}} + \frac{R_2 \ln(R_3/R_2)}{k_{iso}}} \quad (3.28)$$

where  $h$  is the heat transfer coefficient of the hot flue gas, and  $k$  denotes the thermal conductivity, whereas the subscripts *tube* and *iso* refer to respectively the tube material and the insulation material. Because the concentration of aerosol forming vapour in the flue gas is relatively low, a diluted system may be assumed. Therefore, it is plausible that the additional source term, represented by the second term on the RHS of Eq. 3.27 is significantly lower compared to the convective term represented by the first term on the RHS of Eq. 3.27. Under these conditions a Nusselt relation may be used in order to calculate the heat transfer coefficient of the flue gas  $h$  which is defined as:

$$\text{Nu} = \frac{h D_{tube}}{k_g} \quad (3.29)$$

According to Janna [27], the Nusselt number for a fully developed laminar flow in a cylindrical tube under the assumption of a constant wall temperature is 3.66, see also Sec. 3.5.2.

Besides the average flue gas temperature  $T_g$  also the wall temperature has to be known in order to calculate the partial vapour pressure at the wall  $p_{\alpha,wall}$ , necessary to solve Eq. 3.26. In the case of an insulated tube, the wall temperature is mainly dependent on the thickness and thermal conductivity of the insulation material applied. Because the heat transferred from the flue gas towards the cooling water is equal to the heat transferred by convection only, a simple expression for the wall temperature follows:

$$T_{wall}(z) = T_g(z) - (T_g(z) - T_{water}) \frac{U(z)}{h(z)} \quad (3.30)$$

### 3.7 Solution procedure and initial conditions

The model presented basically consists of a General Dynamic Equation (GDE) (Eq. 3.3) as well as the partial differential equations regarding the vapour pressure (Eq. 3.23) and the flue gas temperature (Eq. 3.27). As the flow is assumed to be fully developed, the radial velocity equals zero. As we are interested in the vapour deposition towards the heat exchanger walls additional particle deposition mechanisms are neglected in the model. The boundary conditions necessary to solve the partial differential equations are given by:

$$\begin{aligned} \text{For } z = 0 : & \quad T_g = T_{g,ini} & \quad p_{\alpha,g} \leq p_{\alpha,sat}(T_g) \\ \text{For } r = R_1 : & \quad p_{\alpha,g} = p_{\alpha,sat}(T_w) \\ \text{For } r = R_3 : & \quad T_{water} = \text{Constant} \end{aligned} \quad (3.31)$$

where the subscript  $\alpha$  refers to the aerosol forming compound which is  $K_2SO_4$  and  $R_1$  and  $R_3$  represent respectively the inner radius of the tube and the surface that is directly in contact with the cooling water, see Fig. 3.1. The flue gas temperature near the entrance of the heat exchanger  $T_{g,ini}$  is assumed to be  $1030^\circ C$ , whereas the cooling water temperature  $T_{water}$  is assumed to be constant at  $90^\circ C$ . The physical properties of the flue gas like viscosity, thermal conductivity and heat capacity are taken from Rhine [36], whereas the ideal gas law is used in order to determine the density of the flue gas. Furthermore, the simulations are subjected to the conditions as described in Tab. 3.2.

For the initial PSD, the continuous PSD as described in Eq. 3.1 is approximated by a sectional lognormal particle size distribution. When the discretisation is fine enough it is plausible to assume that one particle size represents the entire range of particles within one size class. Calculating the growth rate of the particles evaluated at the boundaries of each size class shifts the number concentration to larger particle diameters. When particles formed by homogeneous nucleation are smaller than the smallest particle size class, a new size class is generated. The added extra particles per unit volume in the interval  $[z, z + \Delta z]$  can be calculated according to the following relation:

$$N_{k+1} = \int_z^{z+\Delta z} \frac{1}{v} \frac{T_n}{T_g} J dz. \quad (3.32)$$

The corresponding new particles size class  $k + 1$  equals the critical diameter  $d_p^*$ , see Eq. 3.10. In Eq. 3.32,  $J$  is the homogeneous nucleation rate as defined in Eq. 3.5 and  $v$  is the actual flue gas velocity. The quotient of  $T_n$  and  $T_g$  is required for normalisation such that the number concentration is always evaluated at normal temperature  $T_n$ , equaling  $0\text{ }^\circ\text{C}$ . Consequently the real number concentration in the tube section  $\frac{\pi}{4}D_{tube}^2\Delta z$  during each step size has to be recalculated by use of its local temperature. The partial differential equations 3.3, 3.23 and 3.27 are numerically integrated using a second-order explicit Adams Bashford method.

### 3.7.1 Determination of step size $\Delta z$

The step size used becomes of great importance in order to obtain simulation results that are well converged. Coagulation, condensation and nucleation are processes that have to be considered regarding the determination of the minimum axial step size. In order to determine the minimum step size required, simulations with various step sizes were performed. As already mentioned, the main focus is on the wall condensation process. However, this process is strongly related to the the geometric mean diameter (GMD) as well as on the number concentration of the particles formed. Therefore, the GMD and the number concentration of the particles formed at heat exchanger outlet were chosen to determine the minimum step size.

Coagulation could be excluded in the analysis regarding the minimum step size required, saving a lot of computation time. The reason for this was that the minimum characteristic step size for coagulation could be estimated by assuming simple monodisperse coagulation. For this case an analytical solution exists regarding the number concentration of particles as a function of time. Assuming that the maximum depletion of particles in the interval  $[z, z + \Delta z]$  should be less than 50 %, which means that  $N(z + \Delta z) \geq 0.5 \cdot N(z)$ , then the following expression can be used to determine the step size  $\Delta z$  (Hinds [24]):

$$N(z + \Delta z) = \frac{N(z)}{1 + N(z) K_{12} \frac{\Delta z}{v}}, \quad (3.33)$$

where  $K_{12}$  is the collision frequency function as described in Eq. 3.15. In Fig. 3.2 can be observed that the collision frequency  $K_{12}$  for aerosol particles up to  $0.1\ \mu\text{m}$  is at maximum  $\approx 10^{-13}$ . Inserting this value together with the assumption that the maximum depletion of particles in the interval  $[z, z + \Delta z]$  should be less than 50 %, yields that even for a number concentration of  $1 \cdot 10^{16}\ \text{Nm}^{-3}$  and a unity velocity the minimum step size  $\Delta z$  for coagulation should be less than  $1\ \text{mm}$ . As will be shown in Sec. 3.8.3, the maximum observed number concentrations is much lower than  $1 \cdot 10^{16}\ \text{Nm}^{-3}$ , so that the predicted step size is a real worst case estimation, considering coagulation only.

Furthermore, no insulation material around the tubes was applied for determining the minimum step size required. The reason for this is that for increasing heat transfer rates, particles are formed more rapidly as will be demonstrated in Sec. 3.8.4. As a result of homogeneous nucleation, more surface area for condensation is provided (especially when coagulation is fully excluded), so that the condensation process is

developing more rapidly. Therefore, the minimum step size required can be found for the maximum vapour pressure decrease of aerosol forming vapours i.e. for the highest cooling rate. As already mentioned, the variation of the total number concentration and the geometric mean diameter of the particles formed for different step sizes is a measure for convergence. Because of this the influence of the step size  $\Delta z$  is presented as a function these two parameters. The results of these simulations are depicted in Fig. 3.3 which shows the influence of the step size  $\Delta z$  on the predicted total number concentration and the geometric mean diameter of the particles formed for non insulated tubes with inner diameters of respectively 1, 5 and 10 mm.

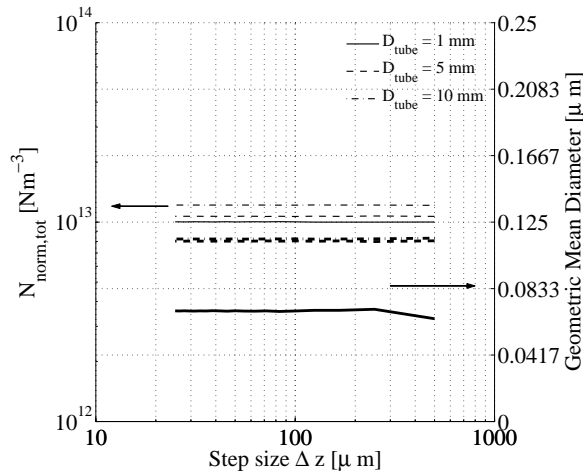


**Figure 3.3.** The effect of varying the step size  $\Delta z$  on the total number concentration and the geometric mean diameter of the particles formed for different tube diameters without applying insulation material.

Explanation: Initial conditions according to Tab. 3.2.

In Fig. 3.3 it can be observed that applying a step size  $\Delta z \leq 200 \mu\text{m}$  results in a quite good convergence regarding the predicted standardised total number concentration and the geometric mean diameter of the particles formed for all depicted tube dimensions. Consequently, applying conservation of mass yields that the predicted wall condensation rate and the corresponding fine particulate emission reduction is also well predicted using a step size  $\Delta z \leq 200 \mu\text{m}$ . The fine particulate emission reduction is also known as the  $\text{PM}_{10}$  emission reduction, denoting the particle fraction with an aerodynamic diameter  $< 1 \mu\text{m}$ . Increasing the step size result in scattering values regarding the predicted geometric mean particle diameter, especially for a tube dimension of 1 mm. Furthermore, it can be concluded that step size for coagulation, which was  $\approx 1 \text{ mm}$  in a worst case situation, was indeed larger than  $200 \mu\text{m}$ . Because of this all further results are generated when applying a step size  $\Delta z \leq 200 \mu\text{m}$ . In this way a convergence solution is assured.

### 3.8 Results

Calculations were performed to determine the concentrations of vapour which is transformed from the gaseous phase into the solid phase. Distinction can be made between homogeneous and heterogeneous nucleation on one side, and wall condensation on the other side. For the simulation potassium sulphate was assumed to be the only aerosol forming vapour. The parameters that can be adjusted in order to enhance wall condensation are:

- the initial inlet velocity,  $v_{ini}$ ,
- the tube diameter,  $D_{tube}$ ,
- the thickness of the insulation material,  $t_{iso}$ .

In order to make sure that the flow inside the heat exchanger tube is always laminar, the Reynolds number should always be smaller than 2300 at each position in the heat exchanger passage.

In chapter 2 an expression for the wall condensation rate is derived when wall condensation and heterogeneous condensation take place at the same moment and particle formation processes and particle deposition mechanisms towards the wall are neglected. A similar equation can also be derived when, besides wall condensation and particle condensation, also formation of particles occurs.

$$\varepsilon_{abs}(z) = \frac{\int_0^z \left( \frac{\partial p_{\alpha,wall}}{\partial z} \right) dz}{\int_0^z \left( \frac{\partial p_{\alpha,wall}}{\partial z} \right) dz + \int_0^z \left( \frac{\partial p_{\alpha,part}}{\partial z} \right) dz} \quad (3.34)$$

where  $\varepsilon_{abs}(z)$  is the wall condensation rate at a position  $z$ , whereas  $\frac{\partial p_{\alpha,wall}}{\partial z}$  and  $\frac{\partial p_{\alpha,part}}{\partial z}$  represent the partial vapour pressure decrease due to respectively wall condensation and particle condensation and formation as described in Eq. 3.26 and 3.25.

In reality the flue gas near the heat exchanger inlet already contains particles,  $\rho_{part,ini}$ . Using the initial values and boundary conditions as described in Sec. 3.3  $9 \text{ mg/Nm}^3$  of aerosol forming vapours have already been transformed into particles, which makes the use of the wall condensation rate debatable. Because of this an extension of the wall condensation rate has been derived, which now describes the PM<sub>1</sub> emission reduction  $\eta$ , defined as:

$$\eta(z) = 1 - \frac{\rho_{part,ini} + (1 - \varepsilon_{abs}(z))(\rho_{\alpha,rel} - \rho_{part,ini})}{\rho_{\alpha,rel}} \quad (3.35)$$

where  $\rho_{part,ini}$  is the initial particle concentration near the heat exchanger inlet, formed due to the excess of aerosol forming vapour in the flue gas and  $\rho_{\alpha,rel}$  is the concentration aerosol forming vapour compounds released to the flue gas. The maximum achievable PM<sub>1</sub> emission reduction decreases when the initial particle concentration near the heat exchanger inlet  $\rho_{part,ini}$  increases. So in the case when all vapour condenses on the walls of the heat exchanger ( $\varepsilon_{abs}(z_{max}) = 1$ ) the maximum

achievable  $PM_1$  emission reduction is limited to the quotient  $(\rho_{\alpha,rel} - \rho_{part,ini})$  and  $\rho_{\alpha,rel}$  which is for the conditions applied equal to  $\eta = 0.85$ .

Furthermore, it is noticed that all results presented are normalised to standard conditions. The standard conditions are depicted in Tab. 3.3.

**Table 3.3.** Definition of standard conditions

Normal temperature, $T_n$	$0 \text{ } ^\circ C$
Normal pressure, $p_n$	$1.014 \cdot 10^5 \text{ Pa}$

### 3.8.1 Effect of varying the initial flue gas velocity

One of the influencing parameters in order to enhance wall condensation could be the initial flue gas velocity. Therefore, the effect of the initial flue gas velocity on the wall condensation rate is investigated. Because the flue gas velocity changes over the heat exchanger length a more common quantity is used; the mass flow rate  $G$  which is defined as  $G = v\rho_g$  and has the dimension  $\left[\frac{kg}{(m^2 \cdot s)}\right]$ . The advantage of the mass flow rate is that this quantity remains constant over the heat exchanger length and is independent of the tube diameter.

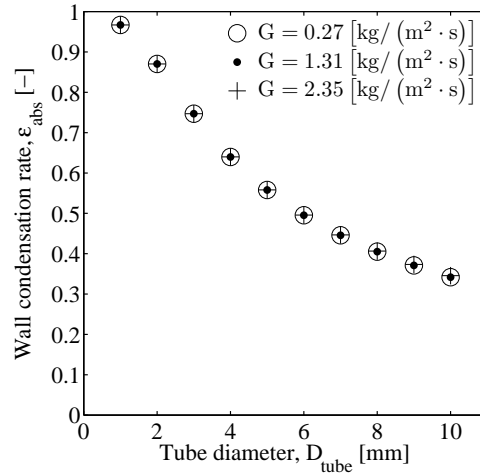


**Figure 3.4.** The effect of varying the mass flow rate  $G$  on the wall condensation rate  $\varepsilon$  for various tube diameters in the case when no insulation material is applied.

Explanation: Initial conditions according to Tab. 3.2.

Figure 3.4 show the wall condensation rate for several tube diameters and several mass flow rates in the case that no insulation material is applied. Two important effects can be observed: first of all the trend of decreasing the tube diameter into the

millimetre regime results in a significant wall condensation rate, up to almost 100 % for a tube diameter of 1 *mm*. When increasing the tube diameter, particle formation and condensation become the dominant effects. Consequently, the wall condensation rate becomes significantly lower. Another important effect that can be observed is that increasing the mass flow rate, so increasing the initial velocity, has no influence on the wall condensation rate. Apparently the influence of the mass flow rate on the contribution of homogeneous nucleation, condensation and coagulation is negligible. This observation leads to exclusion of the mass flow rate variation in the further analysis saving a lot of computation time.

However, regarding the heat transfer the effect of varying the flue gas velocity is immediately noticeable. Increasing the flue gas velocity or mass flow rate for equal tube dimensions results in increasing heat exchanger lengths required to cool down the flue gas temperature to an appropriate temperature. However, the main focus is to invest whether fine particulate emissions can be reduced by enhancing wall condensation, the effect of the flue gas velocity on heat transfer rate is therefore not further investigated.

### 3.8.2 Effect of varying the initial PSD

The results so far presented are all subjected to the initial PSD as described in Sec. 3.3. However, in real applications the initial number concentration and distribution of particles near the heat exchanger inlet are not constant over time. The coarse fly ash fraction mainly depends on the boiler load, flue gas velocities and the design of the combustion unit and the process control system used, see Brunner [11]. Contrary to the coarse fly ash fraction, the initial aerosol concentration and consequently the initial PSD regarding the aerosols mainly depends on the release of aerosol forming species from the fuel that can vary in short intervals due to changing conditions in the fuel bed. Therefore, the question arises what the influence of the initial PSD on the wall condensation rate is. In order to investigate this effect simulations were performed with several initial PSD's using several tube diameters without insulation material. For the simulations an initial geometric mean diameter equals to 62 *nm* and a typical initial geometric standard deviation  $\sigma_{g,ini}$  of 1.6 has been used. Regarding the initial concentration of aerosol forming vapours it is assumed that the saturation ratio  $S = 1$  near the heat exchanger inlet, corresponding to an initial aerosol forming vapour density of 51 *mg/Nm*<sup>3</sup>. The initial number concentration  $N_{norm,ini}$  is varied between  $1 \cdot 10^9$  *Nm*<sup>-3</sup> and  $1 \cdot 10^{14}$  *Nm*<sup>-3</sup>. The results of the simulation regarding the final number concentration and the corresponding geometric mean diameter are depicted in Fig. 3.5.

In Fig. 3.5 it can be observed that for the largest tube diameter presented (10 *mm*) formation of new particles could occur when the initial number concentration of particles,  $N_{norm,ini} \leq 3 \cdot 10^{13}$  *Nm*<sup>-3</sup>. Decreasing the tube diameter, yields that homogeneous nucleation is also suppressed for lower initial particle number concentrations. Furthermore, a remarkable trend can be observed for an initial particle number concentration,  $N_{norm,ini} \ll 3 \cdot 10^{13}$  *Nm*<sup>-3</sup>. The final particle number concentration for each tube dimension tends to a constant number concentration  $N_{norm,tot}$ . For a tube with a diameter of 1 *mm*, the resulting particle number concentration is at minimum

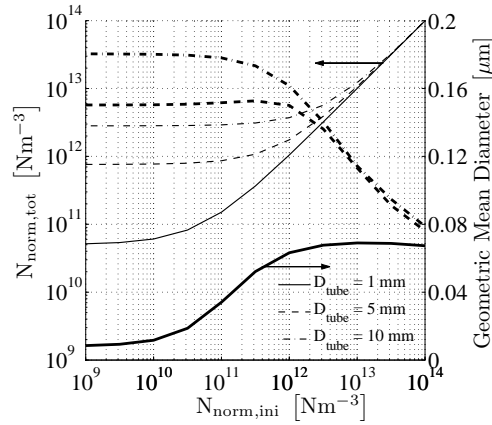


**Figure 3.5.** The effect of varying the initial normalised number concentration  $N_{norm,ini}$  on the final normalised number concentration  $N_{norm,tot}$  and the corresponding geometric mean diameter  $d_g$  in the case without applying insulation material.

Explanations: Initial conditions according to Tab. 3.2; all results are normalised to standard conditions, see Tab. 3.3.

$5 \cdot 10^{10} Nm^{-3}$ , whereas the resulting particle number concentration is at minimum  $3 \cdot 10^{13} Nm^{-3}$  using a tube dimension of 10 mm. Consequently, the geometric mean diameter also tends to a constant value when the initial number concentration is sufficiently small. The other way around yields that, when the initial number concentration of particles in the flue gas is sufficiently large ( $N_{norm,ini} \geq 3 \cdot 10^{13} Nm^{-3}$ ), formation of new particles is widely suppressed, indicated by the fact that the final number concentration is almost equal to the initial number concentration. Apparently homogeneous nucleation and coagulation processes are not relevant for initial particle number concentrations,  $N_{norm,ini} \geq 3 \cdot 10^{13} Nm^{-3}$ .

Because homogeneous nucleation results in relatively constant final particle number concentrations for the case that  $N_{norm,ini} \ll 3 \cdot 10^{13} Nm^{-3}$ , the corresponding geometric mean particle diameters are also rather constant for the various tube diameters. The reason that the GMD of the particles formed decreases with decreasing tube dimensions is caused by the fact that wall condensation becomes the dominant mechanism. As both the particle number concentration and the GMD tend to a constant value for  $N_{norm,ini} \ll 3 \cdot 10^{13} Nm^{-3}$  implies, when mass is conserved, that the wall condensation rate also exhibits the same trend, what also can be observed In Fig. 3.6. Adding more particles to the flue gas  $N_{norm,ini} \geq 3 \cdot 10^{13} Nm^{-3}$  means that more surface area is provided by the particles, so condensation of aerosol forming vapours on already formed particles rapidly becomes the dominant mechanism. As a consequence, the wall condensation rate rapidly decreases with the initial particle number concentration.



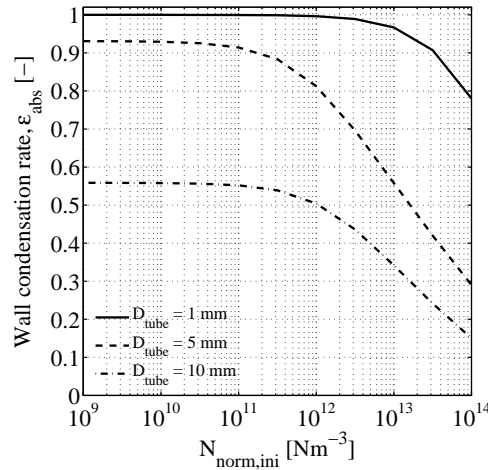


**Figure 3.6.** The effect of varying the initial number concentration  $N_{norm,ini}$  on the wall condensation rate  $\epsilon$  for various tube diameters without applying insulation material.

Explanations: Initial conditions according to Tab. 3.2; all results are normalised to standard conditions, see Tab. 3.3.

### 3.8.3 Influence of coagulation

In Sec. 3.7.1 it is already mentioned that neglecting coagulation saves a lot of computation time. For the further analysis it is therefore investigated whether coagulation may be excluded in such a way that the wall condensation rate and the  $PM_1$  emission reduction is still well predicted, thereby accepting that typical parameters to determine the PSD near the heat exchanger outlet like (GMD, geometric standard deviation and total number concentration  $N_{norm}$ ) could deviate. In Fig. 3.5 it can be observed that, having an initial particle number concentration  $N_{norm,ini} \geq 3 \cdot 10^{13} Nm^{-3}$ , homogeneous nucleation is widely suppressed. Under the assumption that particle deposition on heat exchanger surfaces is neglected, coagulation is the only process left over that might cause a variation in the particle number concentration. However, in order to initiate a substantial reduction of the particle number concentration, an initial particle number concentration in the order of of  $10^{13} Nm^{-3}$  is by far to low, taken into account that the residence time of the flue gas and consequently also the combustion particles is much less than 1 sec. As can be seen in Fig. 2.1, the time to reduce the number concentration by a factor 2 is more than 1 sec. So it appears that based on this simple analysis it is reconfirmed that coagulation is most probably of minor interest.

In order to proof that coagulation indeed may be neglected in the further analysis, simulations with and without coagulation have been performed subjected to the initial values as described in Sec. 3.7 for various tube diameters without insulation. The resulting particle size distributions for various tube diameters with and without coagulation are depicted in Fig. 3.7. In Fig. 3.7 it can be observed that the effect of

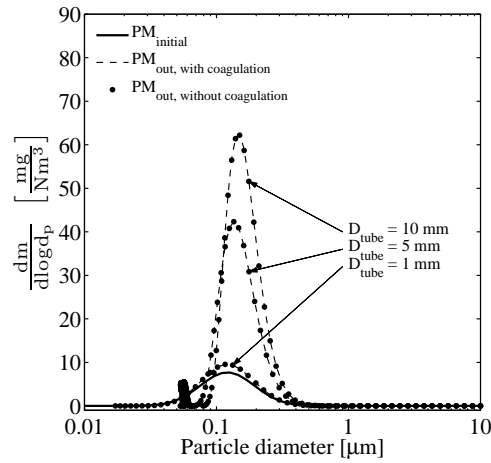


**Figure 3.7.** Effect of coagulation on the final normalised number concentration  $N_{norm,tot}$  and the corresponding geometric mean diameter  $d_g$  in the case without applying insulation material for various tube diameters.

Explanations: Initial conditions according to Tab. 3.2; all results are normalised to standard conditions, see Tab. 3.3.

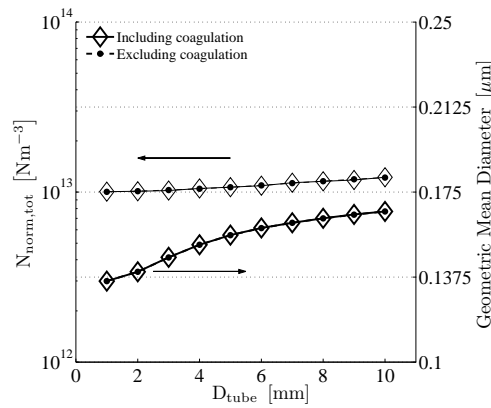


**Figure 3.8.** Effect of coagulation on the final number concentration  $N_{norm,tot}$  and the corresponding geometric mean diameter  $d_g$  in the case without applying insulation material for various tube diameters.

Explanations: Initial conditions according to Tab. 3.2; all results are normalised to standard conditions, see Tab. 3.3.

coagulation is not perceptible. The graphs with and without coagulation perfectly correspond to each other. The small bulge in front of the main peak of the PSD near the outlet of the heat exchanger  $PM_{out}$  for tubes with dimensions of respectively 5

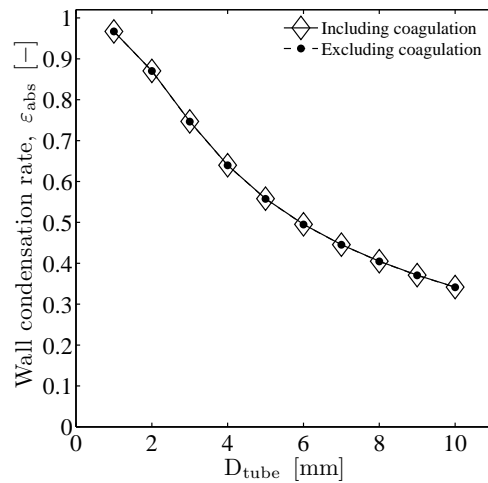


**Figure 3.9.** Effect of coagulation on the wall condensation rate  $\varepsilon$  for various tube diameters without applying insulation material.

Explanation: Initial conditions according to Tab. 3.2.

and 10 mm are caused by the fact that homogeneous nucleation has occurred during the cooling process. The additional particles formed due to homogeneous nucleation are rather low in number concentration, as can be observed in Fig. 3.8. Therefore, these particles mainly grow due to condensation, instead of colliding with the larger particles. Now it is not surprising that, due to conservation of mass, the wall condensation rates for the case with and without coagulation as depicted in Fig. 3.9 also perfectly match.

The results depicted in Fig. 3.7, 3.8, and 3.9 show that the effect of coagulation is almost not perceptible. Consequently, coagulation can be excluded in this study.

### 3.8.4 Effect of insulation on the wall condensation rate

Up to now the results presented are all generated without applying insulation material around the tubes. All effects are expressed in terms of wall condensation rates, geometric mean diameters and total number concentrations. Using the wall condensation rate instead of the PM<sub>1</sub> emission reduction is justified as the wall condensation rate is an independent variable. Varying the initial number concentration for instance results in different wall condensation rates, see Fig. 3.6. When the PM<sub>1</sub> emission reduction would be the parameter, the question arises through which phenomenon this result changes. This could be caused by the fact that the initial mass represented by the initial particles changes or due to a change of the wall condensation rate. Using the wall condensation rate does not have this problem. However, in practice the PM<sub>1</sub> emission reduction is of more interest. When the initial conditions remain constant, it is permitted to use the PM<sub>1</sub> emission reduction as an independent variable.

Therefore, the influence of applying insulation for equal initial conditions on the  $\text{PM}_{10}$  emission reduction is depicted in Fig. 3.10. As already mentioned, it is expected that applying insulation material yields higher wall condensation rates.

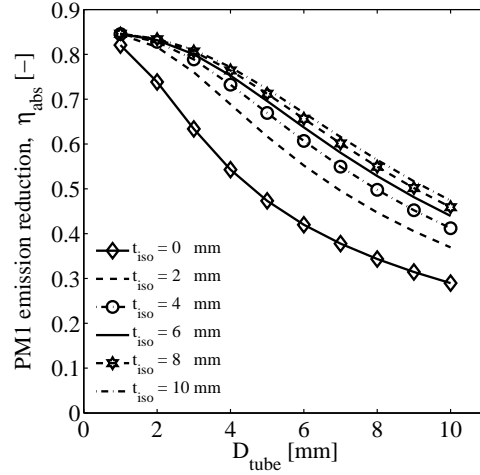


**Figure 3.10.** Effect of applying insulation material on the  $\text{PM}_{10}$  emission reduction for various tube diameters.

*Explanations:* Initial conditions according to Tab. 3.2;  $t_{iso}$  ... thickness of insulation material,  $\overline{R_3 - R_2}$  according to Fig. 3.1; all results are normalised to standard conditions, see Tab. 3.3  $\eta$  ... fine particulate emission reduction.

In Fig. 3.10 two clear trends can be observed. Decreasing the tube dimensions result in a significant reduction of the aerosol emissions  $\eta$ . This trend could also be observed in Fig. 3.4. Using a non insulated tube with an inner diameter of 1 mm results in a  $\text{PM}_{10}$  emission reduction of almost 85 %, the highest possible reduction when assuming that already formed particles cannot be separated from the flue gas. Increasing the tube diameter without applying insulation material rapidly results in a decrease of the  $\text{PM}_{10}$  emission reduction down to approximately 29 % using a tube with an inner diameter of 10 mm.

Secondly, applying insulation material indeed results in a significant increase of the  $\text{PM}_{10}$  emission reduction compared to the case without applying insulation material, which is the desired result. To illustrate this effect, without applying insulation material a  $\text{PM}_{10}$  emission reduction of 47 % could be achieved using a tube diameter of 5 mm. Applying insulation material with a thickness of 4 mm already results in a wall condensation rate of approximately 67 %, which is a significant improvement. Further increasing the thickness of the insulation material yields higher wall condensation rates, but the effect becomes less significant.

The principle of applying insulation material can be explained as follows. The driving force for cooling down the flue gas is mainly proportional to the difference of the flue gas temperature between the bulk  $T_g$  and at the wall  $T_w$ , see also Eq. 3.27.

In the case without insulation the wall temperature almost equals the water temperature  $T_{water}$ . Therefore, the flue gas temperature drops relatively fast. Applying insulation material results in a lower heat transfer coefficient  $U$ , so that the flue gas temperature decrease is toned down. According to Bird et al. [6] the mass transfer rate of the aerosol forming compounds is analogous to the heat transfer rate. Under the assumption that homogeneous nucleation is fully suppressed, the driving force for condensation is proportional to the difference in the partial vapour pressure at the wall and in the bulk for wall condensation on the one hand and the difference between the partial vapour pressure on the particle surface and in the bulk on the other hand. However, the saturated vapour pressure is strongly non linearly dependent on temperature, see Fig. 2.2. Small variations in the flue gas temperature rapidly result in large differences in the saturation vapour pressure. As a result of applying insulation, the wall temperature becomes slightly higher, whereas the saturation vapour pressure is due to its strong non linear dependency almost not influenced by this small temperature variation.

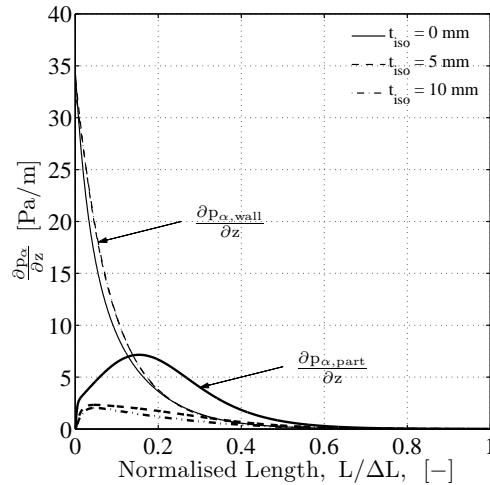


**Figure 3.11.** Effect of applying insulation material on a tube with an inner diameter of 5 mm on partial vapour pressure decrease due to wall condensation  $\frac{\partial p_{\alpha,wall}}{\partial z}$  and due to particle formation and growth  $\frac{\partial p_{\alpha,part}}{\partial z}$ .  
 Explanations:  $t_{iso}$  ... thickness of insulation material,  $R_3 - R_2$  according to Fig. 3.1; Initial conditions according to Tab. 3.2;  $\frac{\partial p_{\alpha,wall}}{\partial z}$  ... partial vapour pressure decrease due to wall condensation;  $\frac{\partial p_{\alpha,part}}{\partial z}$  ... partial vapour pressure decrease due to particle formation and growth.

The situation for condensation of potassium sulphate on already formed particles is somewhat different. In the high temperature region ( $T_g > 800$  °C), the vapour pressure at the particle surface is slightly lower compared to the vapour pressure in the bulk. Therefore, the particle condensation rate is relatively low at high flue gas temperatures. Applying insulation material results in a lower heat transfer rate. As

result of this, the particle temperature remains higher for a longer period of time, such that condensation on particles is suppressed and the wall condensation process is maintained. Therefore, the wall condensation process prevails when applying insulation material in relation to particle condensation. To illustrate this phenomenon, the partial vapour pressure decrease due to wall condensation on the one hand and particle formation and growth on the other hand is depicted in Fig. 3.11 for several insulation thicknesses. In Fig. 3.11 it can be observed that the partial vapour pressure decrease due to wall condensation,  $\frac{\partial p_{\alpha,wall}}{\partial z}$ , remain approximately constant over the entire insulation thickness range, whereas the partial vapour pressure decrease due to particle formation and growth,  $\frac{\partial p_{\alpha,part}}{\partial z}$ , decreases for increasing insulation thicknesses.

The advantage of applying insulation material is obvious. Applying insulation material results in lower fine particulate matter emissions to the atmosphere using the same tube diameter. The other way around, when applying insulation material around the tubes, larger tube dimensions can be used in order to achieve the same particulate emission reduction, which are less sensitive for blocking for instance with coarse fly ash particles. However, a major disadvantage of reducing the heat transfer rate i.e. applying insulation material, is that the effective length of a heat exchanger becomes longer for equal tube dimensions. Therefore, the pressure drop over the heat exchanger, which is proportional to its length, will increase when applying insulation material, see Janna [27]. Besides the advantage that more material is required when reducing the heat transfer rate, also the operational costs per unit produced power i.e. the energy demand of the flue gas fan, increases with the pressure drop. Because of this optimisation is required to arrive a cost efficient aerosol condensing heat exchanger.

### 3.9 Influence of the surface tension on the homogeneous nucleation rate

The formula describing the homogeneous nucleation process as described in Eq. 3.5 has originally been developed by Becker and Döring, Zeldovich and others [3, 57] and consists of a prefactor  $K$  and a term which includes the formation energy  $\frac{-\Delta G^*}{k_b T_g}$ . During the nucleation process clusters of molecules are continuously agglomerating and evaporating. When at a certain moment the concentration of molecules in one cluster is that high that the cluster size remains stable, a particle is formed with a critical diameter as described in Eq. 3.10 which is able to grow. However, the chance that such a critical particle is formed depends on the Gibbs free energy  $\Delta G^*$  which has to be overcome which exhibits a Boltzmann distribution, see Eq. 3.6.

Several forms regarding the kinetic prefactor  $K$  exist [54]. However, the precise form of the prefactor on the final nucleation rate  $J$  is not that important. This is caused by the fact that the homogeneous nucleation rate is mainly dominated by the term which includes the formation energy in the exponent, see Eq. 3.6. Therefore, the nucleation rate and the corresponding critical diameter  $d_{crit}$  are also dependent on the flue gas temperature  $T_g$  and the saturation ratio  $S$ . Figure 3.12 shows the influence of these parameters on the nucleation rate  $J$  for  $K_2SO_4$ . In Fig. 3.12 it

can be observed that a certain saturation ratio  $S$  is required in order to initiate substantial homogeneous nucleation, depending on the temperature. Decreasing the flue gas temperature rapidly has the consequence that significantly higher saturation ratios are required for this specific aerosol forming compound in order to initiate homogeneous nucleation. Because of this, homogenous nucleation of  $K_2SO_4$  is much more suppressed at lower flue gas temperatures. Besides plotting the homogenous nucleation rate, also the number of molecules in a critical cluster is plotted. Assuming a spherical droplet, the number of molecules in a critical cluster  $i$  can be calculated according to the following relation:

$$i = \frac{\pi d_{crit}^3}{6 \hat{v}_{ml}} \quad (3.36)$$

where  $d_{crit}$  is the critical diameter of the cluster, calculated according to Eq. 3.10 and  $\hat{v}_{ml}$  represents the molecular volume. The number of molecules in a critical cluster decreases for decreasing flue gas temperatures, under the assumption that the homogeneous nucleation rate remains constant. Furthermore, it can be observed that the nucleation theory does not hold for extremely high saturation ratios and relatively high flue gas temperatures. When the flue gas temperature is about  $1000\text{ }^\circ\text{C}$  and the saturation ratio is very high (e.g.  $S \geq 600$ ), the critical cluster size becomes in the order of one molecule.

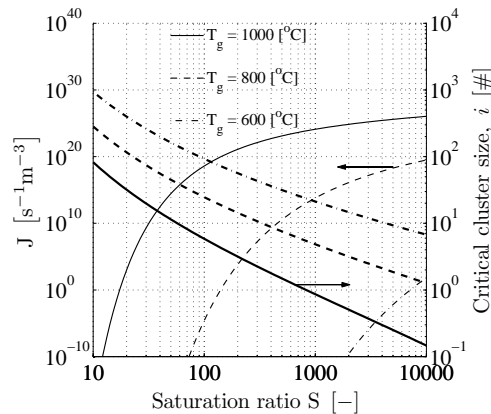


**Figure 3.12.** The influence of the saturation ratio  $S$  and temperature  $T_g$  on the homogeneous nucleation rate of  $K_2SO_4$  and corresponding critical cluster size.

From Eq. 3.6 it can be observed that the formation energy  $\Delta G^*$  is cubically dependent on the surface tension  $\sigma$ . Therefore, the formation energy is extremely sensitive to the surface tension. Small deviations in the surface tension could rapidly result in a significant change of the nucleation rate. Because of this, accurate data regarding the surface tension have to be known. However, no data regarding the macroscopic surface tension  $\sigma_\infty$  of potassium sulphate in solid state as a function of temperature are available. Therefore, an alternative parachor method has been used

in order to determine a fit regarding the macroscopic surface tension as a function of temperature. The parachor method itself has originally been developed by Macleod and Sugden [33, 43]. According to their theory, there exists a correlation between the surface tension and the molar densities of the liquid and vapour phase of a pure component system, correlated by a constitutive constant. This constant is called the parachor  $\mathcal{P}$ . The corresponding relation is given as:

$$\mathcal{P} = \frac{M_\alpha \sigma_\infty^{\frac{1}{4}}}{\rho_{l,s}} \quad (3.37)$$

where  $\rho_{l,s}$  is the difference between the density of the liquid and the density of the vapour in equilibrium with it. A major property of the parachor  $\mathcal{P}$  is that it is approximately constant over wide ranges of temperature. If the value of the  $\mathcal{P}$  remains constant, even in the solid state, than the macroscopic surface tension at low temperatures can easily be determined from the liquid data, such that the macroscopic surface tension is a function of the density only.

Accurate measurements regarding the macroscopic surface tension of molten potassium sulphate as a function of temperature up to 1200 °C, which are accurate within 1 % are given by Bertozzi et al. [5], whereas the density of the molten phase is detailed tabulated by Jaeger [26]. However, despite the accurate physical properties of potassium sulphate in liquid state, the parachor method on itself may still yield incorrect values [40] and is only first order accurate. Deviation in the macroscopic surface tension between the parachor method and experimentally determined macroscopic surface tensions for other substances up to 10 % are observed. Because of this a sensitivity analysis regarding the influence of the macroscopic surface tension on the nucleation rate have been performed, see Fig. 3.13.

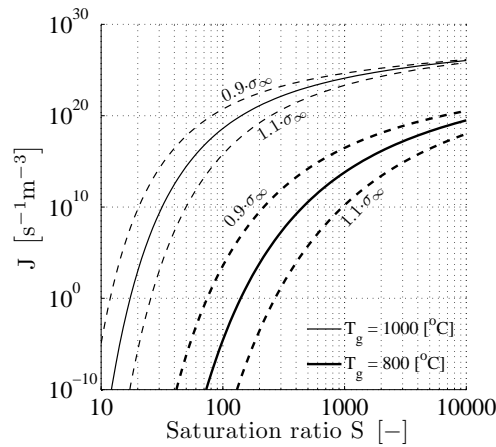


**Figure 3.13.** The influence of the variation of the macroscopic surface tension  $\sigma_\infty$  on the homogeneous nucleation rate of pure  $\text{K}_2\text{SO}_4$  for two different flue gas temperatures  $T_g$ .

For the sensitivity analysis, the macroscopic surface tension as a function of tem-



perature is varied by  $\pm 10\%$  of the nominal macroscopic surface tension. Two different temperatures ( $T_g = 1000^\circ\text{C}$  and  $T_g = 800^\circ\text{C}$ ) have been analysed in order to see the effect of the variation of the surface tension on the nucleation rate. In Fig. 3.13 it can be observed that 10 % variation of the macroscopic surface tension already results in a deviation of the nucleation rate of pure potassium sulphate up to several orders of magnitude.

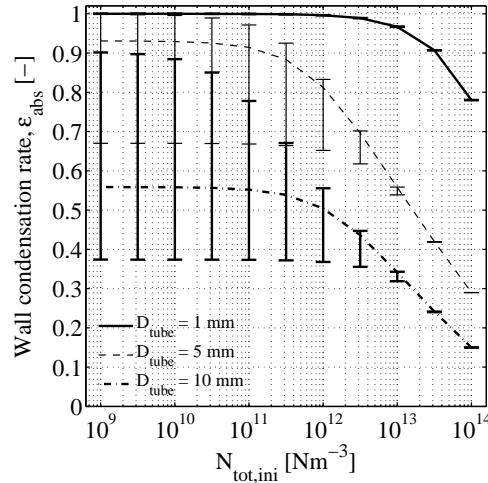


**Figure 3.14.** The absolute wall condensation rate  $\varepsilon_{abs}$  for several initial number concentrations in the case without applying insulation. The error bars represents the minimum and maximum absolute wall condensation rate when the macroscopic surface tension  $\sigma_\infty$  is varied within  $\pm 10\%$ .

Explanation: Initial conditions according to Tab. 3.2.

Because of the strong dependency of macroscopic surface tension on the nucleation rate the question arises what the influence of the macroscopic surface tension on the absolute calculated wall condensation rate  $\varepsilon_{abs}$  is. Therefore, the absolute wall condensation rates for several initial number concentrations without applying insulation material as depicted in Fig. 3.6 are recalculated with respect to a variation in the macroscopic surface tension of  $\pm 10\%$ , see Fig. 3.14. In Fig. 3.14 it can be observed that decreasing the tube dimensions results in smaller deviation with respect to the absolute wall condensation rate when small deviations in the macroscopic surface tension occur. This phenomenon can be explained by the fact that using small tube dimensions homogeneous nucleation is much more suppressed. Therefore, the uncertainty of the absolute wall condensation rate increases for increasing tube dimensions, especially when the initial particle number concentration is rather low. In Fig. 3.14 it can also be observed that for low initial number concentration and relatively large tube dimensions, variations in the absolute wall condensation rates up to more than 50 % could occur. Because of this it is highly doubtful whether the additional particles formed due to homogeneous nucleation as depicted in Fig. 3.5 are also formed

in reality. For high initial number concentrations  $N_{norm,ini} > 1 \cdot 10^{13} Nm^{-3}$  homogeneous nucleation is almost fully suppressed over the entire range of tube diameters even when varying the macroscopic surface tension. Therefore, the influence of the macroscopic surface tension on the wall condensation rate for high initial number concentration becomes less important.

### 3.10 Closure

A mathematical model describing the wall condensation process as well as the particle formation and growth process of aerosol forming vapour in a tubular heat exchanger has been developed. For the sake of simplicity only potassium sulphate is considered as condensing compound. The rate of diffusion of vapour molecules towards the wall of the heat exchanger is calculated by use of a Sherwood relation. For the description of particle formation classical nucleation theory has been used, whereas a diffusion model which includes a correction term for diffusion outside the continuum regime has been applied in order to calculate the radial growth process of the aerosols. Besides nucleation and condensation of aerosol forming vapours also coagulation of the aerosol particles has been applied in order to investigate its relevance.

During the analysis, several parameters have been varied in order to investigate their relevance. One effect that could be observed was that homogeneous nucleation is almost fully suppressed, at an initial number concentration of  $N_{norm,ini} \geq 1 \cdot 10^{13} Nm^{-3}$ . Because coagulation becomes only important for final particle number concentrations of  $N_{norm} > 1 \cdot 10^{16} Nm^{-3}$ , coagulation is of minor interest and could be excluded in the further analysis. A parameter which could easily be adapted even in real-scale applications is the initial flue gas velocity. Therefore, simulation with various initial flue gas velocities have been performed in order to investigate its relevance. The result was obvious. Varying the initial flue gas velocity does not have any influence regarding the  $PM_1$  emission reduction.

Besides parameters which do not influence the fine particulate emission reduction, also two parameters could be determined which have a significant influence on the fine particulate emission reduction. These parameters are the tube dimensions and the way of cooling the flue gas. Using a non insulated tube with an inner diameter of 1 mm under the assumption that already formed particles near the heat exchanger inlet could not be separated from the flue gas, results in a reduction of the fine particulate emission of slightly less than 85 %, which is almost the highest theoretically possible particulate emission reduction regarding the concept applied. Increasing the tube diameter rapidly results in significantly lower particulate emission reductions, down to approximately 29 % for a non insulated tube with an inner diameter of 10 mm. Applying insulation material around the tubes such that the time for wall condensation is enlarged results in even higher particulate emission reduction; up to approximately 20 %.

Furthermore, a sensitivity analysis regarding the particle formation process has been performed. From the analysis it could be observed that the final nucleation rate is extremely sensitive to the macroscopic surface tension. Unfortunately, no measurement results of the macroscopic surface tension in solid state of potassium sulfate

could be found in literature. As an alternative a linear relation between the macroscopic surface tension and the temperature, based on a parachor method is used. However, this method is only first order accurate. Therefore, the macroscopic surface tension has been varied  $\pm 10\%$  compared to the nominal macroscopic surface tension. The result of this relatively small deviation was that, for rather low initial number concentrations  $N_{norm,ini} \ll 1 \cdot 10^{13} Nm^{-3}$ , deviations of the predicted wall condensation rate up to more than 50 % could be observed. Because of this, highly accurate data of the surface tension are required in order to predict the wall condensation rate with an acceptable accuracy for low initial number concentrations. For small channel dimensions wherein wall condensation occurs the influence of nucleation, even for rather low surface tensions, becomes of minor relevance. Therefore, the analysis presented is still valid for the previously mentioned conditions.

## Chapter 4

# 2D model with particle formation and particle deposition in a heat exchanger

### 4.1 Introduction

In the previous chapters it is shown that the principle of condensing aerosol forming vapours in a heat exchanger with channel dimensions in the order of millimetres works. The first order estimation used in chapter 2 has been not detailed enough to design a heat exchanger. Therefore, a plug flow model including condensation of aerosol forming vapours and particle formation was developed that shows encouraging results with respect to the fine particulate matter reductions (chapter 3). However, besides deposition of aerosol forming vapours on heat exchanger surfaces also particle deposition occurs in heat exchanger passages. Therefore, a 2D model is presented that includes both vapour deposition and particle deposition on heat exchanger surfaces as well as condensation of aerosol forming vapours on already present particles and formation of new particles via homogeneous nucleation. The numerical code is implemented in MATLAB <sup>®</sup>.

Several researchers have investigated particle deposition mechanisms. Tsai et al. and He et al. [22] [44] for instance investigated the particle deposition rate in a plate-to-plate thermophoretic precipitator with a plate distance of 0.38 *mm*. Thermophoresis, lift force and Brownian motion were incorporated in the numerical calculations. Experiments as well as numerical simulations showed that particle deposition efficiencies up to 80 % were possible. However, the conditions applied are far away from what is possible from a practical point of view in real small-scale biomass combustion plants. Because of this, it is expected that such high particle deposition efficiencies can never be achieved in real-scale applications. Muñoz-Bueno et al. showed that

deposition of aerosols in a laminar tube resulted in much lower particle deposition efficiencies compared to what is investigated by Tsai et al. and He et al. Despite the fact that the conditions applied were not directly comparable to the conditions applied for small-scale biomass combustion plants, it is expected that considerable deposition of fine particulate matter can be achieved.

In this chapter, mechanisms causing particle deposition are described and simulations are performed to investigate their relevance. Based on literature, lift force and thermophoresis are determined as main forces causing particle deposition. As already mentioned, the model also includes vapour deposition on already existing surfaces, as well as formation of new particles via homogeneous nucleation as described in chapter 2. As common firetube boilers exhibit round tubes, all equations are applied to this geometry in this chapter. Equations expressed in Cartesian coordinates can be found in appendix A. In Sec. 4.3 the results of the simulations are presented. First the fine particulate emission reductions obtained by the 2D-model without particle deposition mechanisms are calculated, so that a comparison can be made with the plug flow model as derived in chapter 3. Therefore, the initial conditions used for the simulations in this chapter are equal to those for the plug flow model. Furthermore, also fine particulate emission reductions due to lift force and thermophoresis are presented. Finally, it is investigated whether particle deposition and condensation of aerosol forming vapours can be decoupled so that an universal parameter can be used to describe the wall condensation rate only, independent of the geometry applied.

## 4.2 Modeling approach

In order to predict the particle deposition efficiency due to lift force and thermophoresis acting on particles, particle trajectories have to be calculated. In a condensing environment with particle formation as well as particle growth this is not that straightforward. Therefore, assumptions and simplifications have been made.

The flow is considered to be hydrodynamically fully developed with a uniform flue gas inlet temperature i.e. as if the flow comes from a previous heat exchanger section without heat transfer. The particles near the heat exchanger have a low inertia and are assumed to follow the streamlines when no external forces act on the particles. Consequently, the particle flux near the heat exchanger inlet exhibits the same parabolic profile as the flue gas velocity. As it is a diluted flow with a particle concentration in the order of some  $mg/Nm^3$ , it can be assumed that the flue gas flow is not influenced by the aerosol particles. For the calculations it is assumed that when a particle reaches the wall, it sticks to it without rebound. Collisions and interactions between particles are not taken into account as the expected residence time in the heat exchanger and the number concentration are that low that coagulation becomes of minor interest, see Sec. 3.8.3.

As already mentioned in Sec. 3.3, potassium sulphate is assumed to be the main aerosol forming compound. Therefore, the analysis presented in this chapter is also limited to this aerosol forming compound only, saving a lot of computation time. Furthermore, the same initial conditions are applied as described in Tab. 3.2, however no insulation material is applied around the tubes. A graphical representation of the

situation is depicted in Fig. 4.1.

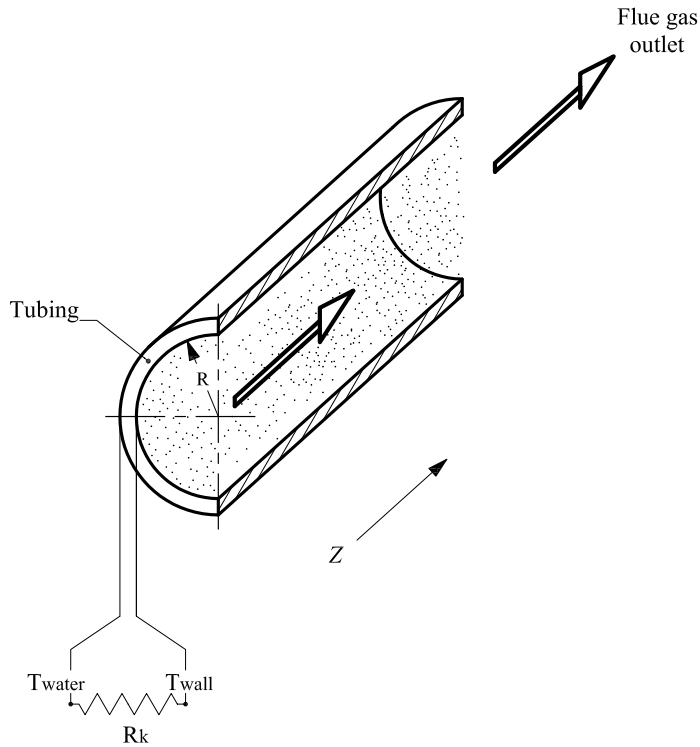


**Figure 4.1.** Schematic representation of one tube as it is applied in the aerosol condensing heat exchanger.

### 4.2.1 Momentum equation

For the calculation of the flow field a fully developed laminar flow near the heat exchanger inlet and no flow in radial direction is assumed. The initial axial velocity expressed in terms of cylindrical coordinates is given by, see Bird et al. [6]:

$$v_z(r) = 2 \frac{\dot{m}_g}{\rho_g \pi R^2} \left( 1 - \left( \frac{r}{R} \right)^2 \right). \quad (4.1)$$

where  $v_z(r)$  is the axial velocity as a function of the radial coordinate  $r$ ,  $\dot{m}_g$  the mass flow,  $\rho_g$  the density of the flue gas and  $R$  the inner radius of the tube. Temperature dependent physical properties have been applied in the analysis.

Conservation of momentum is applied for the calculation of the axial velocity, see Bird et al. [6]. The momentum equation in cylindrical coordinates can be written as:

$$0 = -\frac{dp}{dz} + \frac{1}{r} \frac{d}{dr} \left( \mu_g r \frac{dv_z}{dr} \right), \quad (4.2)$$

where the term  $\frac{dp}{dz}$  represents the pressure drop and  $\mu_g$  is the dynamic viscosity of the flue gas.

### 4.2.2 Energy equation

The energy equation for a cylindrical tube with a constant wall temperature is given by Bird et al. [6] and is given as,

$$\rho_g c_{p,g} v_z \frac{\partial T_g}{\partial z} = \left[ \frac{1}{r} \frac{\partial}{\partial r} \left( r k_g \frac{\partial T_g}{\partial r} \right) \right] + \mu_g \left( \frac{dv_z}{dr} \right)^2 - \Delta H \frac{d\rho_{part}}{dt}, \quad (4.3)$$

where  $\rho_g$  and  $c_{p,g}$  represent respectively the density and the heat capacity of the gas and  $T_g$  is the temperature of the gas. The first term on the right hand side of Eq. 4.3 represents the conductive term, the second term represents the viscous heating term and the third term is the latent heat release by the particles formed as expressed in Sec. 3.4. In the analysis presented it is assumed that the flow is so slow that viscous heating is not significant, and can therefore be neglected.

### 4.2.3 Continuity equation for aerosol forming species

The continuity equation for aerosol forming species in a cylindrical tube under assumption that the total pressure  $p_{tot}$  remains constant is given by Bird et al. [6]:

$$\frac{\partial p_\alpha}{\partial z} = \frac{p_{tot} M_g}{R_u \rho_g v_z} \frac{1}{r} \frac{\partial}{\partial r} \left( r \mathbb{D} \frac{1}{T_g} \frac{\partial p_\alpha}{\partial r} \right) - \frac{p_{tot}}{v_z \rho_g} \frac{d\rho_{part}}{dt} \quad (4.4)$$

The right hand side of Eq. 4.4 consists of two parts. The first term represents the vapour flux towards the cold heat exchanger wall. The second term is a so called source term, consisting of a part describing the particle formation process and a part describing the particle growth process (see Sec. 3.4). In Eq. 4.4  $M_g$  is the molar mass of the carrier gas,  $R_u$  is the universal gas constant and  $\mathbb{D}$  the diffusion coefficient, calculated by Chapman-Enskog's kinetic theory as described in Bird et al. [6].

### 4.2.4 Particle deposition

In order to calculate the particle trajectories, Newton's second law of motion is applied at any instant during the acceleration process, (Hinds, [24]).

$$\frac{d[\vec{v}_p(t) m_p(t)]}{dt} = \sum \vec{F}. \quad (4.5)$$

In Eq. 4.5,  $\vec{v}_p$  represents the particle velocity, whereas the mass of the particle is represented by  $m_p$ . Both parameters are time dependent when particle growth is taken into account.  $\sum \vec{F}$  represents all forces acting on the particle. Two external forces are considered in the calculations regarding the particle trajectory, namely lift

force  $F_{lift}$  and thermophoresis  $F_{th}$ . These forces work in opposite direction of the drag force  $F_{drag}$ . In the following sections all forces will be explained in more detail.

### Drag force

The first term on the right hand side of equation 4.5 is the drag force  $F_{drag}$ , given by Hinds [24]:

$$\vec{F}_{drag} = \frac{m_p C_D \text{Re}_p}{\tau_p 24} (\vec{v} - \vec{v}_p) \quad (4.6)$$

In equation 4.6,  $\tau_p$  represents the particle relaxation time:

$$\tau_p = \frac{(\rho_p - \rho_g) C_c d_p^2}{18\mu_g}, \quad (4.7)$$

where  $C_c$  is the Cunningham slip factor, describing the deviation from the free molecular regime to continuum behaviour, when the particle diameter is in the same order of magnitude as the molecular mean free path of the surrounding gas. The Cunningham slip factor for solid particles is empirically determined by Allen et al. [1] and is already described in Eq. 3.20.

In equation 4.6,  $C_D$  represents the drag coefficient, which is a function of the Reynolds number, based on the particle diameter. The drag coefficient is given by Hinds [24],

$$C_D = \frac{24}{\text{Re}_p} \quad \text{Re}_p < 1, \quad (4.8)$$

and

$$C_D = \frac{24}{\text{Re}_p} \left( 1 + \frac{1}{6} \text{Re}_p^{\frac{2}{3}} \right) \quad 1 < \text{Re}_p < 400. \quad (4.9)$$

where  $\text{Re}_p$  is the Reynolds number based on the particle diameter,

$$\text{Re}_p = \frac{\rho_g |\vec{v} - \vec{v}_p| d_p}{\mu_g}. \quad (4.10)$$

In Eq. 4.10  $|\vec{v} - \vec{v}_p|$  is the relative velocity between the flue gas and and the particle.

### Thermophoresis

When a temperature gradient is established in a gas, the aerosol particles in that gas experience a force in the direction of decreasing temperature. The motion of the particles resulting from that force is called thermophoresis. The magnitude of this force depends on the temperature gradient, as well as on the particle size. Increasing the particle size from the nanometre range to larger particle diameters implies that the Knudsen number changes from the free molecular regime ( $\text{Kn} > 2$ ) into the continuum regime ( $\text{Kn} < 2$ ). Waldmann et al. [53] derived an expression for the thermal force based on the nature of molecular reflection at the particle surface. One disadvantage



of this expression is that it is only valid when particles are within the free molecular regime. An empirical relation for the thermal force when  $\text{Kn} < 2$  is described in Hinds [24]. A disadvantage of the thermal forces described in Waldmann et al. and Hinds [53, 24] is that a discontinuity occurs when the particles are neither in the free molecular regime ( $\text{Kn} > 2$ ) nor in the continuum regime ( $\text{Kn} < 2$ ). He et al. [22] modified an expression (originally derived by Cha et al. and Wood [56, 12]) for the thermal force for the entire range of small and large Knudsen number. This modified expression for the thermal force is then given as:

$$\vec{F}_{th} = 1.15 \frac{\text{Kn}}{4\sqrt{2}\left(1 + \frac{\pi_1}{2}\text{Kn}\right)} \cdot \left[1 - \exp\left(-\frac{\alpha_1}{\text{Kn}}\right)\right] \cdot \left(\frac{4}{3\pi}\phi\pi_1\text{Kn}\right)^{\frac{1}{2}} \frac{k_b}{d_m^2} \nabla T_g d_p^2, \quad (4.11)$$

In Eq. 4.11,  $k_b$  represents Boltzmann's constant,  $d_m$  is the molecular diameter, whereas  $\alpha_1$  is determined as:

$$\alpha_1 = 0.22 \left[ \frac{\frac{\pi}{6}\phi}{1 + \frac{\pi_1}{2}\text{Kn}} \right]^{\frac{1}{2}} \quad (4.12)$$

$\pi_1$  is a quantity determined from an analysis of the friction drag on an aerosol particle and is given by:

$$\pi_1 = 0.18 \frac{\frac{36}{\pi}}{(2 - S_n + S_t) \frac{4}{\pi} + S_n} \quad (4.13)$$

In Eq. 4.13,  $S_n$  and  $S_t$  are respectively the normal and tangential accommodation coefficient. The accommodation coefficient is often used to improve the accuracy of calculations in the *slip flow* regime where the continuum assumption of zero flue gas velocity at the surface is inaccurate because flue gas slip occurs. According to Finger et al. [17], typical accommodation coefficients are close to one, and are therefore assumed to be unity during the calculations. The quantity  $\phi$  is:

$$\phi = 0.25 (9\gamma - 5) \frac{1}{\gamma - 1} \quad (4.14)$$

where  $\gamma$  represents the specific heat ratio.

### Lift force

Particles in a shear field experience a lift force perpendicular to the direction of the bulk flow. The shear lift originates from the inertia effects in a viscous flow around the particle. The expression for the inertia shear lift was firstly obtained by Saffman [38], and is given by:

$$\vec{F}_{lift} = K_{saff} \rho_g^{\frac{1}{2}} \mu_g^{\frac{1}{2}} (\vec{v} - \vec{v}_p) d_p^2 |\nabla \vec{v}|^{\frac{1}{2}} \text{sign}(\nabla \vec{v}). \quad (4.15)$$

The coefficient  $K_{saff}$  in equation 4.15 is the constant coefficient of Saffman's lift force [39], which is 1.615 in this equation and  $\nabla \vec{v}$  is the velocity gradient of the flue gas.

### 4.2.5 Solution method

Due to rotation symmetry, only discretisation in radial and axial direction is applied, so a system of  $n + 1$  grid points in axial direction and  $m + 1$  grid points in radial direction is generated (see Fig. 4.2). Discretisation of the momentum equation results in a set of  $m + 1$  equations. However, there are  $m + 2$  unknown variables (the velocities and the pressure drop). The mass balance over the cross section of the heat exchanger tube is used to come to a closed set of equations. Integration of the mass balance is performed using Simpson's rule (Heath [23]). A second-order explicit Adams Bashford method (Heath [23]) is used for integration in axial direction.

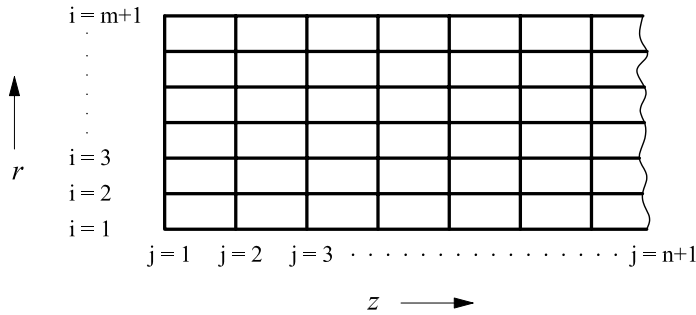


**Figure 4.2.** Discretisation grid for solving the momentum, energy and continuity equation

The step size is important to come to a well convergence solution. Coagulation, condensation and nucleation processes that have to be considered for determination of the minimum axial step size (see Sec. 3.7.1). Moreover, a stability analysis based on the energy equation is required for every tube dimension. The minimum required step size  $\Delta z$  to achieve a stable solution is given by:

$$\Delta z < \frac{c_{p,g} v_z \rho \Delta r^2}{2k_g} \quad (4.16)$$

For the calculations, 11 grid points in radial direction were applied. In the numerical routine, first the momentum, energy and continuity equations are solved before calculating the particle displacement.

Newly born particles formed by homogeneous nucleation are generated and released in the grid point itself. During the calculations, the numerical time step,  $\Delta t \gg \tau_p$ . Therefore, the terminal velocity can be used in order to calculate the new particle position at time  $t + \Delta t$ . According to Hinds [24], this terminal velocity is defined as:

$$\frac{d\vec{x}}{dt} = \vec{v}_{\tau_p} = \tau_p \frac{d\vec{v}_p}{dt}. \quad (4.17)$$

Equations 4.2, 4.3 and 4.4 are subjected to the following boundary conditions.

$$\begin{aligned}
 \text{For } r = 0 : \quad & \frac{\partial T_g}{\partial r} = 0 & \frac{\partial p_{\alpha,g}}{\partial r} = 0 & \frac{\partial v_z}{\partial r} = 0 \\
 \text{For } r = R : \quad & T_g = T_{water} & p_{\alpha,g} = p_{\alpha,sat}(T_w) & v_z = 0 \\
 \text{For } z = 0 : \quad & T_g = T_{g,ini} & p_{\alpha,g} \leq p_{\alpha,sat}(T_g) & 
 \end{aligned} \tag{4.18}$$

In Eq. 4.18, the subscript  $\alpha$  is referring to the aerosol forming compound, which is  $K_2SO_4$ . The inner tube radius is expressed by  $R$  (see Fig. 4.1). Regarding the flue gas inlet temperature  $T_{g,ini}$  an initial flue gas temperature of  $1030\text{ }^\circ C$  near the entrance of the heat exchanger is assumed, whereas the cooling water temperature  $T_{water}$  is assumed to be constant at a typical temperature of  $90\text{ }^\circ C$ . Due to the low thermal resistance of the tubing material  $R_k$ , the wall temperature at the inner side of the tube is assumed to be equal to the cooling water temperature which is correct in first order approximation. The physical properties of the flue gas like viscosity, thermal conductivity and heat capacity are taken from Rhine [36], whereas the ideal gas law is used in order to determine the density of the flue gas. Furthermore, the simulations are subjected to the conditions as described in Tab. 3.2.

### 4.3 Results

Simulations regarding aerosol emission reductions with varying tube dimension between  $1\text{ mm}$  up to  $10\text{ mm}$  have been performed. During these simulations, the mass flow rate  $G$  is kept constant at  $0.27\frac{kg}{(m^2 \cdot s)}$ , which corresponds to a flue gas velocity at heat exchanger inlet of  $1\frac{m}{s}$ . The background for choosing the mass flow rate is the fact that this quantity remains constant over the heat exchanger length and is independent of the tube diameter and inlet temperature. However, in Fig. 3.4 it can be observed that an arbitrary mass flow rate can be chosen without influencing the final results.

Due to lift force and thermophoresis, distinction can be made between particle emission reduction due to direct condensation of aerosol forming elements on heat exchanger walls and direct deposition of already formed particles. The precipitation efficiency  $\eta_{part}$  is defined as:

$$\eta_{part} = \frac{\rho_{part,dep}}{\rho_{\alpha,rel}} \tag{4.19}$$

where  $\rho_{part,dep}$  represents the concentration of fine particles per unit volume that deposit on heat exchanger walls due to external forces. The concentration of aerosol forming elements per unit volume in the flue gas in gaseous as well as in solid state is denoted by  $\rho_{\alpha,rel}$ . Regarding the deposition of fine particles it is noticed that this comprises the deposition of already existing particles near the inlet of the heat exchanger as well as the amount of vapour that is transferred into particles via gas to particle conversion mechanisms. Applying conservation of mass of the aerosol forming species yields the particulate emission reduction due to direct condensation of aerosol forming elements on heat exchanger walls, based on the total amount of aerosol forming elements released to the flue gas:

$$\eta_{vapour} = \frac{\rho_{rel} - (\rho_{part,dep} + PM_1)}{\rho_{\alpha,rel}} \quad (4.20)$$

where  $PM_1$  is the total particle concentration near the outlet of the heat exchanger per normal cubic metre with an aerodynamic diameter  $< 1\mu m$ . Summation of Eq. 4.19 and 4.20 gives the total absolute  $PM_1$  emission reduction:

$$\eta_{abs} = \eta_{part} + \eta_{vapour} = \frac{\rho_{\alpha,rel} - PM_1}{\rho_{\alpha,rel}} \quad (4.21)$$

where  $\eta_{abs}$  is the absolute  $PM_1$  emission reduction due to deposition of particles formed as well as due to direct condensation of aerosol forming vapours on heat exchanger surfaces.

### 4.3.1 Particulate emission reduction in a cylindrical tube without consideration of additional forces acting on aerosol particles

Under consideration of equal initial conditions and neglecting additional forces acting on aerosol particles, the results gained with the 2D-model should be comparable with particulate emission reductions obtained by the plug flow model as depicted in Fig. 3.10. Therefore, first simulation without additional forces acting on aerosol particles were performed. Therefore, the particle acceleration term as described in Eq. 4.5 was set to zero. The simulation results regarding the  $PM_1$  emission reduction obtained by the 2D model, together with the simulation results obtained by the plug flow model are depicted in Fig. 4.3.

In Fig. 4.3 it can be observed that the resulting  $PM_1$  emission reductions derived by the two models correspond reasonably well. Small deviations regarding the predicted  $PM_1$  emission reduction occur for relatively large tube dimensions. This is mainly caused by the fact that in the 2D model the temperature and aerosol forming vapour distribution near the heat exchanger inlet are uniformly distributed, contrary to the flue gas velocity profile. Consequently, the temperature distribution and the distribution of the aerosol forming vapours changes along the heat exchanger length from a uniform distribution to a parabolic distribution. Especially in the first part of the heat exchanger section, this development process is accomplished with relatively high gradients near the heat exchanger walls. These relatively high gradients cause slightly higher heat and mass transfer rates, see Bird et al. [6], which are not taken into account in the plug flow model. Because of this, differences regarding the  $PM_1$  emission reductions can be observed.

Besides calculating the absolute particulate emission reductions for various heat exchanger dimensions, also the corresponding particle number concentration  $N_{tot}$  and geometric mean diameter are determined, so that a direct comparison between the 2D-model and the plug flow model is possible. The results are depicted in Fig. 4.4.

In Fig. 4.4 can be observed that in general the final number concentration calculated according to the 2D-model is approximately 14 % higher compared to the plug flow model over the entire range of tube dimensions. Regarding the GMD, just the

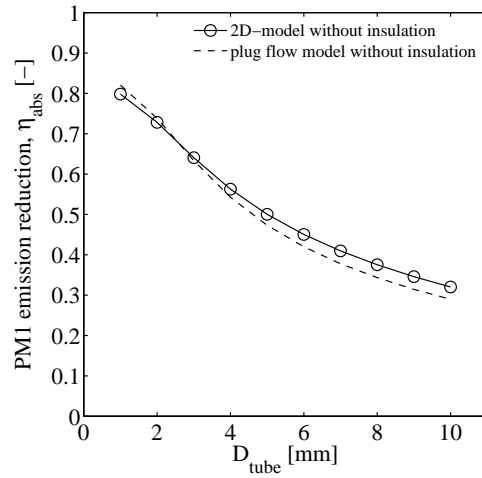


**Figure 4.3.** Comparison of the PM<sub>1</sub> emission reduction  $\eta_{abs}$  between the 2D model without additional forces and the plug flow model as described in chapter 3.

Explanation: Initial conditions according to Tab. 3.2.

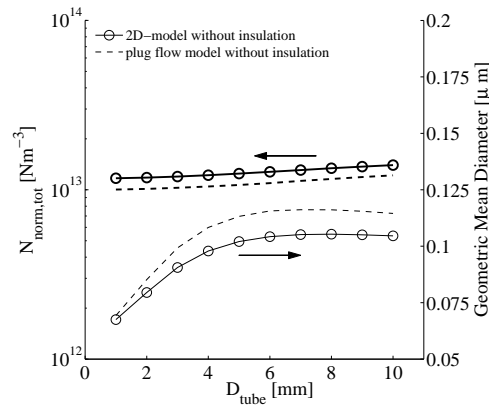


**Figure 4.4.** Comparison of the resulting particle number concentration  $N_{norm,tot}$  and the corresponding geometric mean diameter  $d_g$  between the 2D model without lift force and thermophoresis and the plug flow model.

Explanation: Initial conditions according to Tab. 3.2; all results are normalised to standard conditions, see Tab. 3.3.

opposite trend can be observed. The reason for this difference is mainly caused by the fact that the nucleation rate  $J$  strongly depends on temperature and saturation ratio. Due to the strong radial dependency of these parameters the predicted final number concentration in the 2D-model is slightly higher, resulting in slightly lower

geometric mean diameters.

### 4.3.2 Particulate emission reduction in a cylindrical tube with consideration of additional forces acting on aerosol particles

In the previous section the  $PM_{10}$  emission reduction without additional forces acting on aerosol particles is depicted. Due to temperature and velocity gradients occurring in a water cooled heat exchanger it is expected that under influence of these gradients lift force and thermophoresis might result in higher  $PM_{10}$  emission reductions.

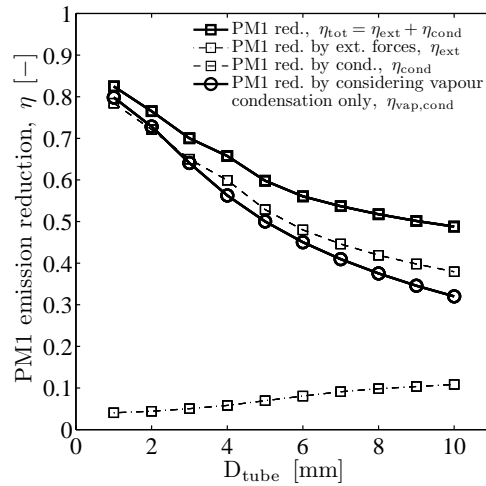


**Figure 4.5.** Calculated  $PM_{10}$  emission reduction,  $\eta_{tot}$  (continuous line with  $\square$ ) considering external forces,  $\eta_{ext}$  (dashed line with  $\square$ ) and direct condensation of aerosol forming vapours on heat exchanger surfaces,  $\eta_{cond}$  (dashed dotted line with  $\square$ ), compared to calculated  $PM_{10}$  emission reduction considering only direct condensation of aerosol forming vapours on heat exchanger surfaces,  $\eta_{vap,cond}$  (continuous line with  $\circ$ ).

The simulation results incorporating the effect of lift force and thermophoresis are depicted in Fig. 4.5. Distinction is made between direct deposition of fine particulate matter and  $PM_{10}$  emission reduction due to direct condensation of aerosol forming vapours. Furthermore, Fig. 4.5 also contains the  $PM_{10}$  emission reduction when lift force and thermophoresis are excluded in the analysis i.e. when  $PM_{10}$  emission reduction only occur due to direct condensation of vapour molecules.

In Fig. 4.5 it can be observed that the total  $PM_{10}$  emission reduction by incorporating lift force and thermophoresis is higher compared to the case when these mechanisms are excluded, which is the expected trend. The influence of both  $PM_{10}$  emission reduction processes is investigated by subdividing the  $PM_{10}$  emission reduction in a part that describes direct deposition of fine particulate matter and a part that describes direct condensation of vapour molecules on heat exchanger walls.

Due to the lift force and thermophoresis the particle trajectories exhibit a non linear motion, which will be outlined in Sec. 4.4. Because of this the particle concentration in the vicinity of the walls becomes higher, resulting in a larger surface area represented by the already formed aerosol particles. As a result of this, particles in the vicinity of the wall sweep the flue gas clean of aerosol forming vapours i.e. first aerosol growth and formation occur in the vicinity of the wall, resulting in a decrease of aerosol forming vapours in the flue gas, after which these particles deposit on heat exchanger walls. Consequently, applying conservation of mass, the resulting fine particulate emission reduction becomes higher.

A remarkable trend regarding the  $PM_{10}$  emission reduction due to direct vapour deposition can be observed. Including particle deposition results in higher direct vapour deposition rates. The reason for this trend is caused by the mutual influence of the particle deposition rate on the direct vapour deposition rate, resulting in different partial vapour pressure profiles. Therefore, the  $PM_{10}$  emission reduction with particle deposition differs from the case when particle deposition is excluded.

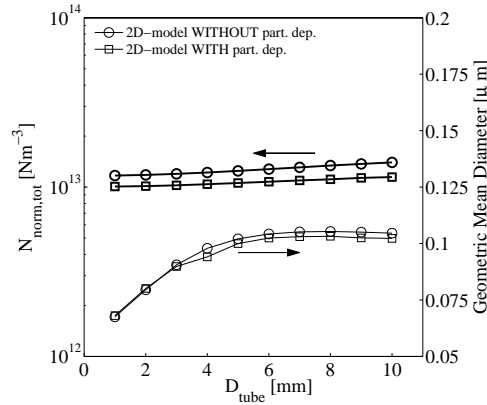


**Figure 4.6.** The final number concentration  $N_{norm,tot}$  and the corresponding geometric mean diameter with and without particle deposition mechanisms.  
Explanation: Initial conditions according to Tab. 3.2; all results are normalised to standard conditions, see Tab. 3.3.

The trend that direct deposition of already formed particles becomes of minor interest for smaller tube dimension can be explained as follows. Due to the fact that decreasing tube dimensions result in higher direct vapour deposition rates on heat exchanger surfaces yields that applying conservation of mass, the particles depositing on heat exchanger walls become smaller. It is noticed that this explanation only holds when the effect of the particle size on the deposition rate is of minor importance in the relevant particle size range. The effect of the particle size on the particle deposition rate will be discussed in Sec. 4.4. In Fig. 4.6, which shows resulting GMD and final number concentration  $N_{tot}$  near the heat exchanger outlet, it can be observed that the resulting GMD, and in first order approximation also the size of the depositing particles, are in the range between  $0.07 \mu m$  and  $0.1 \mu m$ . For increasing tube

dimensions, exhibiting lower direct vapour deposition rates towards heat exchanger walls, the resulting particle dimensions should become larger. However, due to the cubic dependency of the particle size and due to formation of new particles this trend becomes less perceptible.

Comparing the final number concentration, when additional particle deposition mechanisms are included in analysis, with the situation without additional particle deposition it can be observed that the resulting final number concentration is slightly lower compared to the case when additional particle deposition is excluded. The final number concentration is approximately 15 % lower over the entire range of tube dimensions. The difference in the geometric mean diameter is, due to its cubic dependency, much less perceptible, less than 3 %.

## 4.4 Analysis of particle deposition mechanisms

In this section the additional particle deposition mechanisms in cylindrical tubes, as described in Sec. 4.2.4, are investigated in more detail. This is done by analysing each relevant mechanism causing particle deposition. As can be observed in Fig. 4.5 the contribution of additional particle deposition mechanisms has a noticeable influence on the  $PM_{10}$  emission reduction. In the analysis presented thermophoresis and lift force are considered. Other forces like gravitational settling can be neglected due to the low mass of the aerosol particles.

Thermophoresis is the force that rather small aerosol particles experience under influence of a temperature gradient, whereas lift force is a force caused by a velocity difference between the particle and the carrier gas and the velocity gradient. On the other hand drag force and the change of momentum due to changing particle mass, prevent particle deposition. Drag force is the force in direction opposite to the particle motion, resulting from the viscous term. The change of momentum caused by condensation can easily be derived from Newton's second law of motion which is defined as (Hinds [24]):

$$\sum \vec{F} = \frac{d[\vec{v}_p(t) m_p(t)]}{dt} = m_p \frac{d\vec{v}_p(t)}{dt} + \vec{v}_p(t) \frac{dm_p}{dt} \quad (4.22)$$

In a non condensing environment the last term on the right hand side of Eq. 4.22, which is the change of momentum due to changing particle mass, is equal to zero.

The additional forces acting on the aerosol particles are related to velocity and temperature gradients. For investigation of the influence of the additional forces, condensation is excluded from the analysis. The advantage of this approach is that the influence of all other forces can easily be generalised. Generalisation of the velocity and temperature field is performed using a dimensionless radius and length. The dimensionless radius is defined as the ratio between the actual radius  $r$  and maximum radius  $R$  so that the dimensionless radius is defined as  $\frac{r}{R}$ . The dimensionless length of the heat exchanger is normalised with respect of the maximum radius  $R$  and the Peclet number  $Pe$ , so that the dimensionless length is defined as  $\frac{l}{RPe}$ , where  $l$  is the actual heat exchanger length. The Peclet number  $Pe$  relates the rate of advection of a flow to its rate of diffusion and is defined as:



$$Pe = \frac{2Rv_z}{\alpha} \quad (4.23)$$

where  $\alpha$  represents the thermal diffusivity,  $\frac{k_g}{\rho_g c p_g}$ .

In Fig. 4.7, presenting the axial velocity profile on several positions in a heat exchanger passage, it can be seen that, especially in the beginning, the flue gas velocity decreases rapidly, due to the change in density of the flue gas. Contrary to the velocity profile, the temperature profile is assumed to be uniform near the heat exchanger inlet e.g. as if the flow comes from a previous heat exchanger section without heat transfer. As a result of this high temperature gradients occur especially in the wall region near the heat exchanger inlet, see Fig. 4.8.

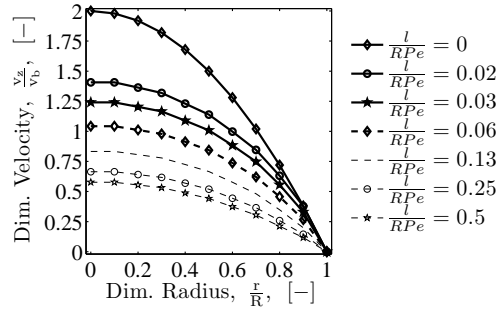


**Figure 4.7.** Dimensionless velocity profile inside heat exchanger at various dimensionless positions.

Explanations:  $r$  ... actual tube radius;  $R$  ... maximum tube radius;  $l$  ... actual heat exchanger length;  $Pe$  ... Peclet number;  $v_z$  ... flue gas velocity;  $v_b$  ... average initial bulk velocity of flue gas; initial conditions according to Tab. 3.2.

The simulation results for transport and deposition of particles, released at several initial positions near the heat exchanger inlet are depicted in Fig. 4.9. For the simulations an initial flue gas velocity of  $1030 \text{ }^\circ\text{C}$  is assumed. When gravitational settling is neglected, the results are independent of the angular position of the tubes. As can be observed in Fig. 1.1, the aerosol fraction consists of particle with an aerodynamic diameter  $< 1 \text{ }\mu\text{m}$ . In general the geometric mean diameter of the particle size distribution is around  $0.10 \text{ }\mu\text{m}$ , whereas the head and the tail of the aerosol distribution contains particles around  $0.01 \text{ }\mu\text{m}$  and  $1.00 \text{ }\mu\text{m}$ . Consequently, calculations are subjected to the extreme particle sizes as well as to the mean particle size that can be observed in the aerosol distribution, viz.  $0.01 \text{ }\mu\text{m}$ ,  $0.10 \text{ }\mu\text{m}$  and  $1.00 \text{ }\mu\text{m}$ .

In Fig. 4.9 it can be observed that particles with an aerodynamic diameter of  $0.10 \text{ }\mu\text{m}$  show a tendency to move faster towards the wall, compared to particles with an initial aerodynamic diameter of respectively  $0.01 \text{ }\mu\text{m}$  and  $1.00 \text{ }\mu\text{m}$ . Apparently a maximum particle size dependent deposition velocity exists. Furthermore, it can be observed that particles released in the vicinity of wall move faster towards the wall, compared to particles near the centre of the tube. Indicating that particles in the

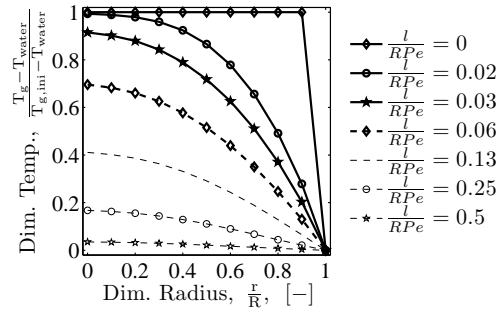


**Figure 4.8.** Dimensionless temperature profile inside heat exchanger at various positions as a function of the dimensionless radius.

Explanations:  $r$  ... actual tube radius;  $R$  ... maximum tube radius;  $l$  ... actual heat exchanger length;  $Pe$  ... Peclet number;  $T_{water}$  ... cooling water temperature; initial conditions according to Tab. 3.2.

vicinity of the wall experience a larger external force, indicated by a sharply curved particle trajectory.

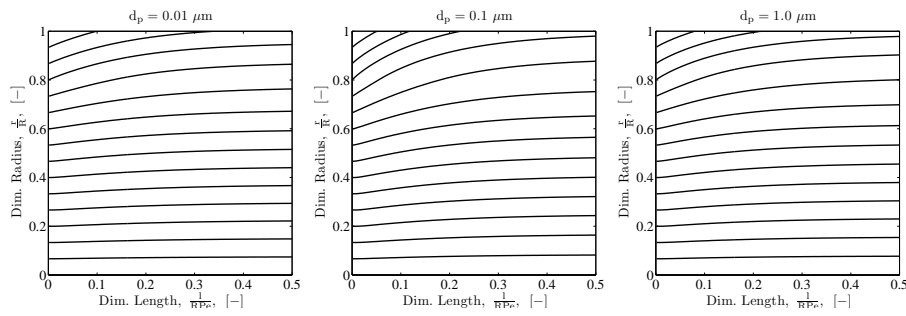


**Figure 4.9.** Particle trajectories for various particle dimensions released at several initial positions near the entrance of a heat exchanger passage.

Explanations:  $l$  ... actual heat exchanger length;  $Pe$  ... Peclet number;  $d_p$  ... aerodynamic particle diameter; initial conditions according to Tab. 3.2.

In order to investigate the contribution of each particle deposition mechanism (except the additional force resulting from the condensation process), typical accelerations for particles released at a dimensionless radius of  $0.75R$  near the heat exchanger inlet as a function of the dimensionless length are investigated (see Fig. 4.10). In Fig. 4.10 it can be observed that thermophoresis and drag are competing processes, whereas acceleration due to lift is of minor relevance compared to the other mechanisms. The reason for this is twofold. Firstly, the relative velocity between particle and carrier gas is, due to its low inertia, very low. Secondly, the flow is assumed to be fully developed, resulting that the velocity gradient near the entrance is low

compared to a developing flow. These two phenomena yield that the force resulting from lift as described in Eq. 4.15 can be excluded in the further analysis. As a consequence of neglecting lift force in the analysis, the resulting particle acceleration is mainly dominated by thermophoresis and drag. This directly implies that the relative particle velocity is strongly subjected to the temperature gradient. This also explains the sharply curved particle trajectory near the wall as can be observed in Fig. 4.9.

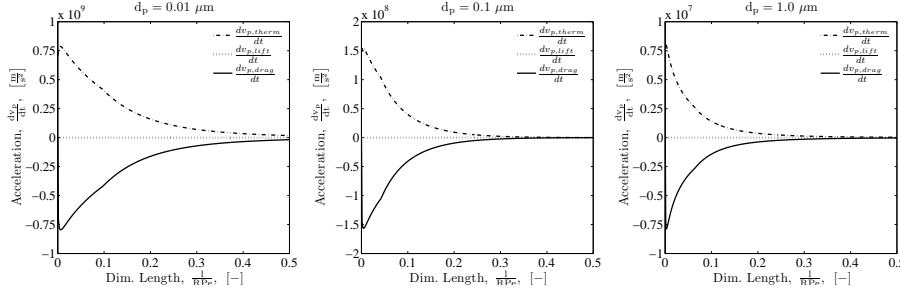


**Figure 4.10.** Radial particle acceleration for various particle dimensions released at a dimensionless radius  $\frac{r}{R}$  of 0.75 near the entrance of a heat exchanger passage.

Explanations:  $l$  ... actual heat exchanger length;  $Pe$  ... Peclet number;  $d_p$  ... aerodynamic particle diameter;  $\frac{dv_{p,therm}}{dt}$  particle acceleration due to thermophoresis;  $\frac{dv_{p,lift}}{dt}$  particle acceleration due to lift;  $\frac{dv_{p,drag}}{dt}$  particle acceleration due to drag; initial conditions according to Tab. 3.2.

Because all other external forces except thermophoresis and drag are irrelevant regarding the particle deposition rate, the resulting force can easily be analysed in more detail. In equation 4.11 it can be observed that the thermophoretic force, besides the temperature gradient, also depends on the particle size and the flue gas temperature, summarised in the Knudsen number  $Kn$ . The resulting thermophoretic deposition velocity according to Newton's second law of motion is:

$$\vec{v}_{th} = \frac{\vec{F}_{th}}{m_p} \tau_p \quad (4.24)$$

where  $\vec{F}_{th}$  is calculated according to equation 4.11. A graphical representation of the normalised thermophoretic velocity for several temperatures is depicted in Fig. 4.11. In Fig. 4.11 it can be observed that particles having diameters slightly larger than  $0.1 \mu m$  show the highest deposition velocity per unit temperature gradient over a wide range of temperatures. Decreasing the flue gas temperature in general results in a lower average thermophoretic velocity. This trend is caused by the fact that the mobility of the surrounding gas molecules is strongly temperature dependent and increasing temperatures result in increasing mobilities. Relatively large particles e.g  $Kn \ll 1$ , exhibit relatively low normalised thermophoretic velocities. The reason for this is the fact that these particles are much larger compared to the mean free path of the surrounding gas molecules and are therefore less sensitive to colliding gas

particles. Furthermore, it can be observed that small particles e.g  $Kn \gg 1$ , are not that sensitive to temperature variations in general.

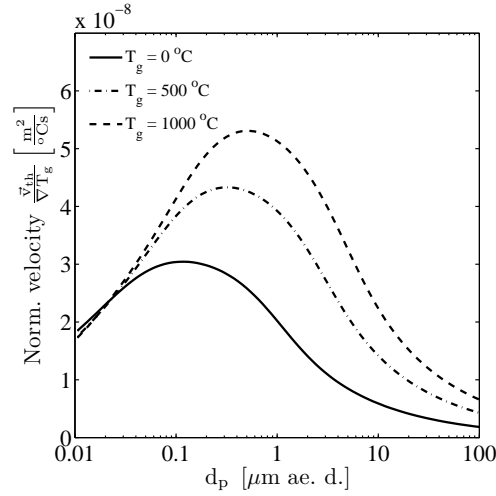


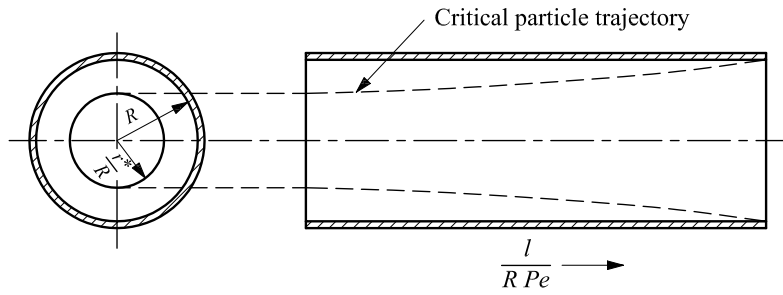
**Figure 4.11.** Thermophoretic velocity  $\tilde{v}_{th}$  normalised with the temperature gradient  $\nabla T_g$  as function of the particle diameter  $d_p$ .

In order to calculate the amount of particles depositing due to thermophoresis, a particle deposition rate can be defined which is the flux of particles depositing on heat exchanger surfaces divided by the total flux of particles through the heat exchanger. In order to predict the deposition rate of particles of one specific size, it is sufficient to calculate the critical particle trajectory for that specific particle size as proposed by Lin et al. [32]. The critical particle trajectory is defined as the trajectory of a particle with a specific diameter just depositing at the end of the heat exchanger, see Fig. 4.12. Particles entering the heat exchanger at an initial position  $> r^*$  will deposit somewhere on the heat exchanger wall, whereas particles entering the heat exchanger at a position  $< r^*$  will leave the heat exchanger.

When assuming a hydrodynamically fully developed flow, the thermophoretic particle deposition rate  $\eta_{th}$  can easily be calculated as a function of the critical particle trajectory by use of the following relation:

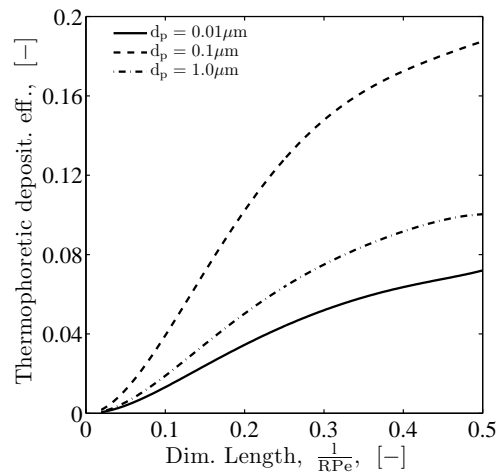
$$\eta_{th} = \frac{\int_{r^*}^R 4\pi \left(1 - \left(\frac{r}{R}\right)^2\right) r dr}{\pi R^2} \quad (4.25)$$

Figure 4.13 shows cumulative particle deposition rates as functions of the axial dimensionless coordinate for particles with various diameters. In general it can be seen that the particle deposition rates tend to approach an asymptotic value, caused by low thermal gradients for increasing axial positions. Furthermore, it can be observed that the cumulative deposition rate is non linearly proportional to the particle size,



**Figure 4.12.** Schematic representation of the critical particle trajectory in a cylindrical tube.

i.e. particles with a size of  $0.10 \mu\text{m}$  show a larger cumulative deposition rate than particles of  $0.01 \mu\text{m}$  and  $1.00 \mu\text{m}$ . The total deposition rate for  $0.10 \mu\text{m}$  particles is approximately 18 % using a dimensionless length of 0.5, whereas the deposition rates for particles having diameters of  $0.01 \mu\text{m}$  and  $1.00 \mu\text{m}$  are respectively 7 % and 10 % for a dimensionless heat exchanger length of 0.5. So the tendency that particles with a typical diameter of  $0.10 \mu\text{m}$  move faster towards the wall resulting in higher wall deposition rates, as observed in Fig. 4.9, could be quantified by use of Fig. 4.13.



**Figure 4.13.** Cumulative thermophoretic deposition efficiency for various aerodynamic diameters as a function of the normalised length.

Explanations:  $l$  ... actual heat exchanger length;  $R$  ... maximum tube radius;  $Pe$  ... Peclet number; initial conditions according to Tab. 3.2.

In first order approximation the depositing particles have diameters equal to the GMD near the heat exchanger outlet, which is approximately  $0.1 \mu\text{m}$ . Formation of

new particles can be assumed to be limited, by comparing the final number concentrations obtained by the 2D-model with and without additional particle deposition mechanisms, see Fig. 4.6. Using these approximations, a particle deposition rate due to thermophoresis of about 18 % is expected as can be seen in Fig. 4.13.

Besides a thermophoretic deposition rate as described in Eq. 4.25, also a thermophoretic deposition rate based on the absolute  $\text{PM}_{10}$  emission reduction  $\eta_{abs}$  and the particle emission reduction due to direct deposition of particles  $\eta_{part}$  can be derived. It is noticed that this relation only holds when thermophoresis is the dominating deposition mechanisms. This alternative thermophoretic deposition rate is defined as:

$$\eta_{th} = \frac{\eta_{part}}{1 - \eta_{abs} + \eta_{part}} \quad (4.26)$$

Calculations of the alternative thermophoretic deposition rate as described in Eq. 4.26 based on the results obtained in Fig. 4.5 show that the alternative thermophoretic deposition rate varies between 14 % and 19 %. This result is in good agreement with what is expected assuming no particle formation and an average size of the depositing particles of  $0.1 \mu\text{m}$ , see Fig. 4.13.

## 4.5 Conversion from cylindrical coordinates to arbitrary coordinates

Up to now only heat exchangers with cylindrical cross sectional areas have been modeled and investigated as current boiler designs exhibit this geometry. From the modeling results it can be observed that the smaller the tube dimensions, the higher the fine particulate emission reductions are. As heat exchanger passages in the order of millimetres are required, plate type heat exchangers also have to be considered for this application.

Several different heat exchanger designs have been investigated in order to find alternative heat exchanger geometries applicable to aerosol reduction for small-scale biomass combustion plants. In electrical equipment for instance, heat exchangers which consist of a base plate on which straight rectangular fins are mounted through which cooling air flows are commonly used for cooling electronic components [4, 27]. The efficiency of these heat exchangers strongly depends on the thermal conductivity of the material applied. One major advantage of the structure applied is that these heat exchangers show a good optical accessibility and therefore cleaning is not that difficult. Besides this also in automotive and air conditioning industry compact heat exchanger designs like finned tube heat exchangers are commonly used [27]. These heat exchangers comprise a multitude of small channel allowing a sandwich structure to maintain structural integrity while minimising material use. One similarity of the investigated heat exchangers was that the channel dimensions were mainly rectangularly shaped. Because of this it is likely that the final heat exchanger design for aerosol emission reductions is also based on such a structure.

For heat transfer and pressure drop calculations, results are commonly expressed using a characteristic dimension of the conduit cross section, the so called hydraulic diameter. The hydraulic diameter  $D_h$  is defined as [27]:

$$D_h = \frac{4A}{O} \quad (4.27)$$

where  $A$  is the cross sectional area and  $O$  is the wetted perimeter of the cross section.

Contrary to the mass transfer of aerosol forming vapours, heat transfer is not that sensitive to the presence of already formed particles in the flow. Therefore, it is necessary to determine whether scaling by use of the hydraulic diameter is permitted when heat transfer and mass transfer occur simultaneously in the presence of already formed particles. Therefore, the model as derived in Sec. 4.2 is transformed into a Cartesian coordinate system. The resulting equations are described in appendix A. The transformation from cylindrical coordinates to Cartesian coordinates results in different momentum, energy and continuity equations. Using a Cartesian and a cylindrical coordinate system the influence of the geometry (i.e. rectangularly shaped flue gas channels and cylindrically shaped flue gas channels) on the particulate emission reduction can be investigated.

Using a Cartesian coordinate system, the calculations of Sec. 4.2 are repeated for a exchanger consisting of two parallel plates with a distance  $2B$ , see Fig. 4.14. When the plate distance is much smaller than the width, ( $B \ll W$ ), the so called *edge effects* are negligible and the analysis presented can be restricted to transport in longitudinal and transversal directions, denoted by  $x$  and  $z$  in Fig. 4.14.

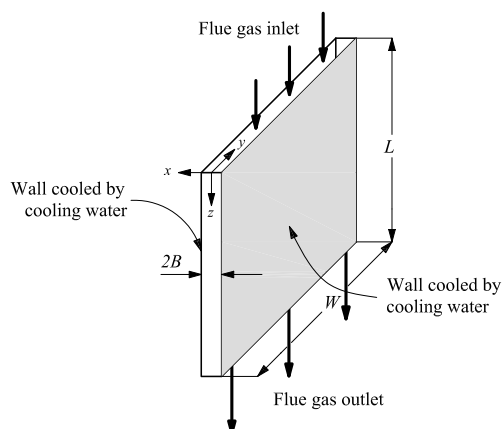


**Figure 4.14.** Schematic drawing of a plate type heat exchanger, with the plate distance much smaller than the plate width  $B \ll W$ .

In Fig. 4.15 it can be concluded that for small diameters the hydraulic diameter indeed is a relevant parameter to relate the behaviour of different geometries. When additional particle deposition mechanisms are excluded from the analysis, i.e. when direct vapour deposition is the only mechanism causing fine particulate emission reductions, a maximum difference in the  $PM_{10}$  emission reduction of less than 4 % can be observed. Compared to cylindrical cross sections, slightly higher  $PM_{10}$  emission reductions can be observed using a plate type heat exchanger when additional particle

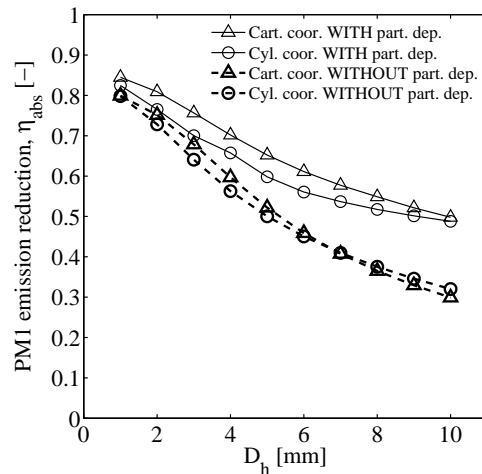


**Figure 4.15.** Comparison of the PM<sub>1</sub> emission reduction  $\eta_{abs}$  with lift force and thermophoresis (continuous line) and without particle deposition mechanisms (dashed line) for two different heat exchanger designs as a function of the hydraulic diameter  $D_h$ .

Explanationss: lines with  $\triangle$  ... heat exchanger with a rectangular cross section as described in Fig. 4.14; lines with  $\circ$  ... heat exchanger with a circular cross section.

deposition mechanisms are included, which amounts to approximately 25 %.

## 4.6 Closure

In this chapter a 2D model describing aerosol formation and growth as well as deposition of vapours and precipitation of aerosol particles on heat exchanger surfaces in a laminar heat exchanger are presented. Literature shows that with respect to particle deposition, thermophoresis and lift force are mechanisms causing particle deposition due to respectively temperature gradients and velocity gradients. Since gravitational settling was neglected in the analysis due to the low particle mass, the results presented in this chapter are independent of the orientation of the heat exchanger.

At first, simulations concerning particle deposition were performed. Therefore, the results obtained could easily be compared with results obtained according to the plug flow approach as described in chapter 3. A good agreement between the plug flow approach and the two dimensional model could be observed. Entrance effects that are not incorporated in the plug flow model cause slight deviations from the 2D model, however deviation between both models are within 10 %.

Secondly also simulations with additional particle deposition mechanisms have been performed. Simulation results show for 1 mm tube dimensions an increase of the aerosol reduction from 80 to 82 % when these particle deposition mechanisms are included. Increasing tube dimensions show that lift force and thermophoresis become of more importance. Including these particle deposition mechanisms yields that the



calculated aerosol emission reductions increases from 32 to 49 %. The reason for this trend is mainly due to the fact that the direct deposition of aerosol forming vapours on heat exchanger surfaces decreases for increasing tube dimensions. Applying conservation of mass shows that the depositing particles are larger in size compared to the depositing particles for smaller tube dimensions.

Furthermore, also the relevant particle deposition mechanisms are analysed in more detail. After investigation of the particle deposition mechanisms included in the model, it appears that thermophoresis and drag force are the only relevant competing processes. Based on the analysis presented the thermophoretic deposition efficiency for round tubes containing particles with a size of around  $0.1 \mu m$  should be about 18 %. Unfortunately, in a condensing atmosphere also particle growth and formation of new particles could occur. However, assuming that the size of the depositing particle is of equal size as the geometric mean diameter near the heat exchanger outlet and assuming no formation of new particles, an alternative thermophoretic deposition rate could be defined. This alternative thermophoretic deposition rate is recalculated from the absolute  $PM_1$  emission reduction  $\eta_{abs}$  and the particle emission reduction due to direct deposition of particles  $\eta_{part}$ . Based on the alternative approach, thermophoretic deposition rates between 14 % and 19 % could be observed which is in good agreement to what is expected from the analysis. This gave the desired result that the particle depositing mechanisms are well implemented in the model, so that the predicted fine particulate emission reductions are reliable.

For designing an aerosol condensing heat exchanger it is useful to have universally applicable models which are independent of the heat exchanger geometries applied. Because in heat exchange calculations the hydraulic diameter is often used as a characteristic length scale to predict the convective heat transfer coefficient, it is obvious to investigate whether this parameter could also be used in combined heat and mass transfer applications. In contrast to heat transfer, the mass transfer rate is rather sensitive to the presence of already formed particles. Because of this, a comparison regarding the fine particulate emission reductions between cylindrical and plate type heat exchangers has been made. The results showed that excluding additional particle deposition mechanisms results in comparable  $PM_1$  emission reductions. When additional particle deposition mechanisms are taken into account, slightly higher  $PM_1$  emission reductions could be observed for narrow sized plate type heat exchangers.

# Chapter 5

## Experiments: Proof of concept

### 5.1 Introduction

Parallel to the numerical analysis of wall condensation, experiments with several heat exchanger designs were performed in a slip stream of a pilot-scale biomass combustion plant to verify the models developed and to assess the applicability of heat exchangers with small passages in biomass combustion applications.

In this chapter the experimental setup and the testing procedure are described for analysing the different aerosol condensing heat exchangers. The geometries of the first aerosol condensing heat exchangers stay close to conventional hot water boiler designs i.e. flue gas flows through the tubes, whereas the tubes are surrounded by cooling water. Using this setup it was possible to verify the numerical models developed as described in chapter 3 and 4 by experimental results. The experimental results of these heat exchangers are given in Sec. 5.3.4

Due to some practical limitations with one of the water cooled heat exchangers additional measurements with a gas to gas heat exchanger were required to prove the concept that condensation of aerosol forming vapours indeed can be stimulated, resulting in lower fine particulate matter emissions. The experimental results obtained with the gas to gas heat exchanger are given in Sec. 5.4.3.

### 5.2 Methodology

#### 5.2.1 Biomass combustion plant used for experiments

A grate fired biomass combustion plant with a horizontally moving grate was used for experiments, see Fig. 5.1. The intake of the biomass fuel depends on the load. The movement of the grate also depends on the load. The biomass combustion plant consists of a primary and a secondary combustion zone. Contrary to the primary combustion zone, the secondary combustion zone consists of two ducts. Furnace

temperatures are measured continuously in several zones and are controlled by flue gas recirculation below and above the grate. For heat transfer the biomass combustion plant is equipped with a flame tube boiler comprising a fire tube and two ducts of flame tubes with inner diameters of  $1\frac{1}{2}$ ". The first and second duct of the flame tube boiler have respectively 30 and 16 tubes. The nominal boiler capacity amounts to  $180\text{ kW}_{th}$ . Furthermore, the combustion plant as shown in Fig. 5.1 is equipped with a control system keeping the oxygen level in the flue gases constant.

The heat exchangers tested were connected in a slip stream to the secondary combustion zone (see Fig. 5.1). To allow for easy replacement of the heat exchangers, a flexible mount was realised. The flow through the heat exchanger and the measurement section was established by a separate flue gas fan. The flue gas velocity in the heat exchanger tested and the measurement section was manually controlled. The measurement section after the test heat exchanger consist of a  $1\frac{1}{4}$ " tube.

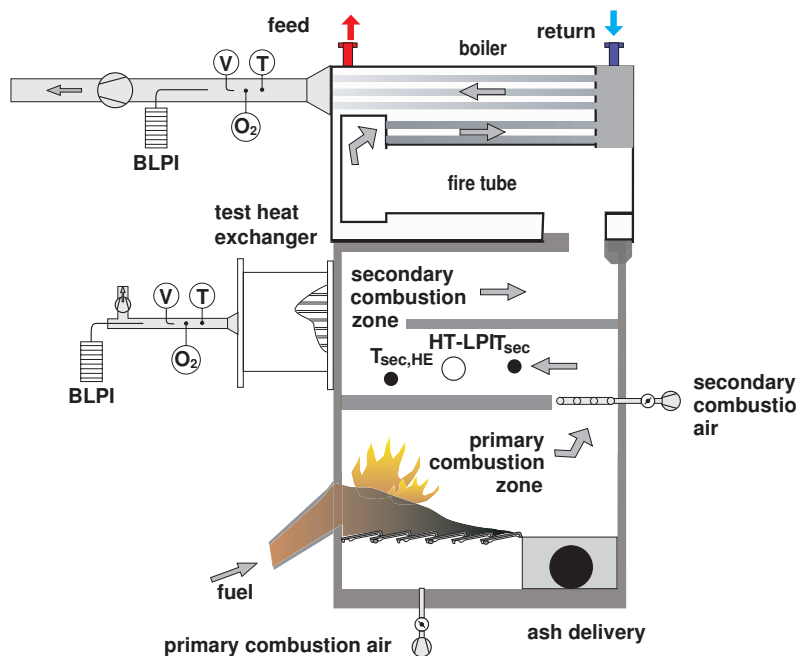


**Figure 5.1.** Experimental set-up of the biomass combustion plant with measurement points in the secondary combustion zone and downstream the boiler and heat exchanger tested.

Explanations: V ... measurement position for the flue gas velocity; T ... measurement position for the flue gas temperature; O<sub>2</sub> ... measurement position for measuring the oxygen content; BLPI ... measurement position for Berner-type low pressure impactors; HT – LPI ... measurement position for high temperature low pressure impactors; T<sub>sec</sub> ... thermocouple measuring the flue gas temperature in the secondary combustion zone; T<sub>sec,HE</sub> ... thermocouple measuring the flue gas temperature in the secondary combustion zone in front of the heat exchanger.

The fuel used for the experiments consists of chemically untreated wood chips with a typical dimension of a couple of centimetres which is a fuel that is commonly applied in small-scale biomass combustion plants. The fuel is stored in a container with a capacity to run the plant for approximately 4 to 5 days. Consequently, several fuel batches were required for the experiments.

### 5.2.2 Requirements for the experimental aerosol condensing heat exchangers

The flue gas flow in commonly used firetube boilers is turbulent to obtain a high heat transfer coefficient. Increasing the Reynolds number results in an increase of the convective heat transfer between the walls of the heat exchanger and the bulk of the flow, but causes a high pressure drop and consequently requires a lot of energy [27]. Contrary to turbulent flow heat exchangers, laminar flow heat exchangers ( $Re < 2300$ ) are based on conductive heat transfer causing a lower pressure drop, but require a larger heat exchanging surface. The volume and amount of material used can be kept in the same order by decreasing the size of the channels, thus maintaining structural integrity while increasing the heat exchanging surface.

Several laminar flow heat exchangers with different heat exchanger passages were designed and tested to proof the working principle and the practical applicability. The boundary conditions concerning the design of these exchangers are derived from physical and practical limitations:

- The Reynolds number based on the hydraulic diameter of the heat exchanger passage should always be below 2300 in order to obtain a laminar flow.
- The flue gas temperature downstream the heat exchanger should be less than  $200\text{ }^{\circ}\text{C}$  to make sure that the condensation process of all volatilised species in the flue gas is fully completed and to achieve a thermal efficiency comparable with common boiler designs.
- The pressure drop over the heat exchanger should be less than  $350\text{ Pa}$  to be comparable with usually applied boiler designs.

The designs of the heat exchangers tested to proof the concept of stimulating condensation of aerosol forming vapours are explained in Sec. 5.3.1, 5.3.2 and 5.4.1.

### 5.2.3 Measurement techniques

The aim of the experiments was to determine the fine particulate matter emissions downstream the heat exchangers tested and downstream the boiler for comparison. Nine stage Berner-type-low-pressure impactors (BLPI) and upstream nozzles for isokinetic sampling were used for measuring the particle size distribution (PSD) of the aerosols downstream the boiler and the aerosol condensing heat exchanger, see Fig. 5.1. The BLPI is heated up to flue gas temperature in order to avoid condensation of water inside the impactor. An extensive description of this impactor is given in Brunner [9].

For normalisation of the particulate matter emission to standard conditions (dry flue gas and 13 vol.%  $O_2$ ) it is necessary to measure parameters like oxygen content and flue gas temperatures. Therefore, devices measuring the flue gas temperature and oxygen content, denoted with respectively  $T$  and  $O_2$  in Fig. 5.1, are installed in the measurement section downstream the heat exchanger tested and in the flue gas duct downstream the boiler. For measuring the flue gas temperatures downstream the heat exchangers tested and the boiler, as well as the flue gas temperature in the secondary combustion zone ( $T_{sec}$ ), type K thermocouples were used. A data acquisition system was used in order to sample data continuously. Prandtl tubes were used for measuring flue gas velocities (see Fig. 5.1).

#### 5.2.4 Determination of the chemical composition of fuels and aerosols

Wet chemical analysis of the fuel and the aerosols have been performed to determine its chemical composition. Based on the chemical composition of the fuel in combination with release factors obtained from literature it is possible to estimate the concentration aerosol forming compounds in the flue gas. Performing wet chemical analysis of the aerosols sampled by use of impactors downstream the heat exchanger tested as well as downstream the boiler provides information whether the aerosol condensing heat exchanger influences the chemical composition of the emitted aerosols. The methods for analysing the fuel samples as well as the aerosols are extensively described in [9].

#### 5.2.5 Calculations regarding the maximum potential for aerosol formation

Several fuel batches were required for experiments. Due to the inhomogeneity of the fuel, the potential for aerosol formation and the aerosol composition differs for each fuel batch. As a result of this, the concentration of aerosols and the resulting particle size distribution, varies in time during the experiments. In order to estimate the concentration of aerosols, samples from different fuel batches were analysed to determine the chemical composition. Based on an average fuel composition the concentration of aerosol forming compounds in the flue gas can be estimated based on release factors as described in Sec. 3.2, resulting in the maximum potential for aerosol formation.

#### 5.2.6 Definitions of emission reduction efficiencies

By use of the setup as shown in Fig. 5.1 it is possible to investigate the influence of the different heat exchanger designs on the fine particulate emission reduction. This is done by determining the aerosol concentration by use of two impactor measurements at the same time downstream both the aerosol condensing heat exchangers and the boiler. Hereby it is possible to determine a fine particulate emission reduction, compared to ordinary boiler designs. The average relative particulate emission reductions related to the ordinary boiler design  $\overline{\eta_{rel,exp}}$  obtained by using both impactor measurements can easily be calculated according to the following relation:

$$\overline{\eta_{rel,exp}} = \frac{1}{n} \sum_{i=1}^n \left( 1 - \frac{PM_{1,HE,i}}{PM_{1,boiler,i}} \right) \quad (5.1)$$

In Eq. 5.1,  $PM_{1,HE}$  and  $PM_{1,boiler}$  represent the particle fraction with an aerodynamic diameter  $< 1 \mu m$  of one coupled set of measurements expressed in  $mg/Nm^3$  (related to dry flue gas 13 vol.%  $O_2$ ). The subscripts *HE* and *boiler* refer to respectively the aerosol condensing heat exchanger and the boiler. The total number of impactor measurements that are performed simultaneously for each heat exchanger dimension is represented by  $n$ . It has to be noticed that since the average particulate emission reduction is nonlinear in the input parameters, the calculated average relative particulate emission reduction,  $\overline{\eta_{rel,exp}}(PM_{1,HE}, PM_{1,boiler})$ , is not equal to  $\eta_{rel,exp}(\overline{PM_{1,HE}}, \overline{PM_{1,boiler}})$ .

Besides determining the aerosol emission reduction, also the element reduction (emission related to a certain element) has been determined for some impactor measurements. Therefore, the aerosols downstream the aerosol condensing heat exchanger and the boiler, sampled by use of the impactors, have been subjected to a wet chemical analysis concerning K, S, Cl, Na, Zn and Pb. As a certain concentration of aerosols is required to determine its chemical composition, the impactor stages containing almost no aerosols are excluded in the analyses. The element reduction is calculated according to the following relation:

$$\eta_{element} = 1 - \frac{\sum_{j=1}^k X_{el,HE,j}}{\sum_{j=1}^k X_{el,boiler,j}} \quad (5.2)$$

In Eq. 5.2,  $X_{el}$  is the concentration of the particular element in the aerosols on impactor stage  $j$ . The subscripts *HE* refer to the aerosol condensing heat exchanger whereas the subscript *boiler* refer to the boiler.

### 5.3 Laminar flow shell and tube heat exchanger

The first heat exchangers tested stay close to the conventional boiler design with the exception of smaller tube dimensions and laminar flow profile. Heat exchangers with three different tube dimensions were tested, having diameters of 12.5, 6.2 and 1.07 mm. By use of these heat exchangers it was possible to see whether the predicted trend obtained from the theoretical analysis could also be found in practice. For the sake of simplicity abbreviations for the different heat exchanger designs have been introduced, see Tab. 5.1.

In this section, firstly a brief description of the heat exchangers used is given after which the fuel analysis and the particulate emission reductions will be discussed.

**Table 5.1.** Abbreviations for the different heat exchangers tested.Explanation:  $D_h$  ... hydraulic diameter.

abbreviation	$D_h$
HE1	12.50 mm
HE2	6.20 mm
HE3	1.07 mm

### 5.3.1 Description HE1 and HE2 with variable tube dimensions of 12.50 and 6.20 mm

One water cooled shell and tube heat exchanger with variable inner tube diameters was developed, see Fig. 5.2. Water flows around the circular tubes. Five or fifteen tubes with tube diameters of 12.50 (HE1) respectively 6.20 mm (HE2) were used for the experiments. A thermostatic valve near the cooling water outlet was used to control the water temperature by flow regulation. The tubes inside the heat exchanger have a fixed length of one metre and can easily be exchanged by tubes with other diameters. The side of the heat exchanger which is directly in contact with the flue gas is covered with an insulation plate to prevent condensation of aerosol forming species in front of the heat exchanger, instead of inside the heat exchanger. The insulation plate minimises the temperature drop of the flue gas in front of the inlet of the heat exchanger due to radiation.

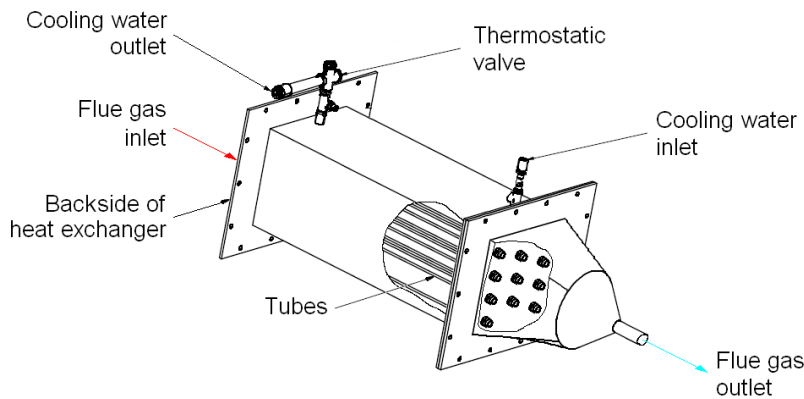


**Figure 5.2.** Schematic drawing of a shell and tube heat exchanger with exchangeable tube dimensions having a fixed length of 1 m. Five tubes were applied for tubes HE1 ( $D_h = 12.50$  mm), whereas fifteen tubes were applied for HE2 ( $D_h = 6.20$  mm)

### 5.3.2 Description of HE3 with a tube dimension of 1.07 mm

It was not possible to use the same heat exchanger construction as described before for tubes with an inner diameter in the order of one millimetre as the maximum pressure drop would be exceeded. Because of this, a completely new heat exchanger consisting of 664 tubes with an inner diameter of 1.07 mm was designed and tested (HE3), see Fig. 5.3. The reason for choosing this tube dimension was the commercial availability of the material.

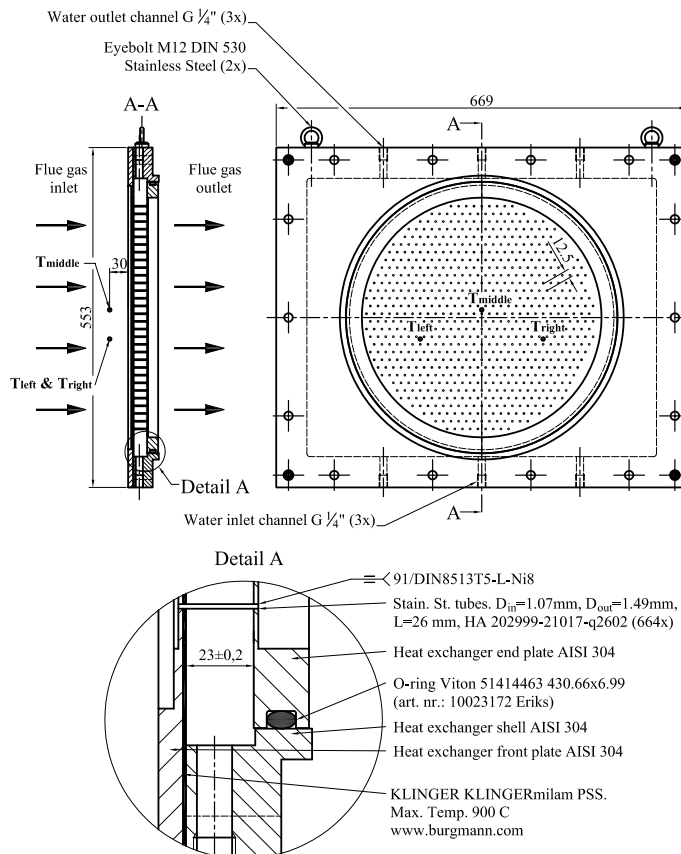


**Figure 5.3.** Schematic drawing of a shell and tube heat exchanger with tube dimensions of 1.07 mm and a fixed length of 23 mm (HE3). The measurement positions for determining the flue gas inlet temperature are determined by  $T_{left}$ ,  $T_{middle}$  and  $T_{right}$

The design consists of a heat exchanger front plate and a heat exchanger end plate between which the tubes are welded, see Fig. 5.3. The tubes have a fixed length of 23 mm laid out on a 12.5 mm triangular pitch. A heat exchanger shell covers the end plate and the tubes. Cooling water flows through the shell and around the tubes. An O-ring connection seals the shell and end plate. Using this design the heat exchanger



is statically determined to minimise thermal stresses. Due to the narrow pitch it was not possible to insert an insulation plate on the side of the heat exchanger facing towards the furnace, e.g. on the flue gas inlet side.

### 5.3.3 Design calculations concerning the laminar flow shell and tube heat exchanger

For the calculation of the temperature profile, round tubes with a constant wall temperature are assumed. As the concentration of aerosol forming vapours is in the range of milligrams per normal cubic metre, latent heat release is neglected. When axial conduction is neglected compared to radial conduction, the resulting energy equation has the following form (Bird et. al [6]):

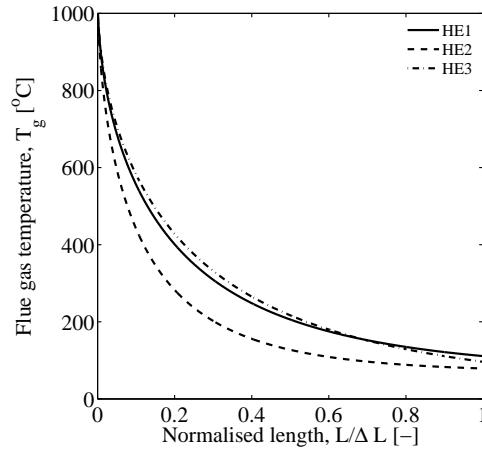


**Figure 5.4.** Calculated flue gas temperature for two different tube dimensions as a function of the normalised length for the water cooled heat exchanger. The real length for HE1 ( $D_h = 12.50 \text{ mm}$ ) and HE2 ( $D_h = 6.20 \text{ mm}$ ) is 1 m, whereas the real length for HE3 ( $D_h = 1.07 \text{ mm}$ ) is 23 mm.

$$\frac{\partial T_g}{\partial z} = \frac{-4h}{D_{tube} v \rho_g c_{p,g}} (T_g - T_w), \quad (5.3)$$

where  $T$  is the temperature and  $D_{tube}$  the tube diameter. The subscripts  $g$  and  $w$  refer to respectively the flue gas and the heat exchanger wall, whereas  $z$  represents the axial coordinate. An adapted Nusselt relation for the heat transfer coefficient  $h$  for a thermally and hydrodynamically developing entrance region was applied [51]. Due to a sophisticated cooling system, the wall temperature  $T_w$  was assumed to be constant at 70 °C for HE1 and HE2. Contrary to the previous heat exchanger no sophisticated cooling water system was available for HE3. Ordinary tap water with an average temperature of approximately 20 °C was used as cooling medium. The initial flue gas temperature  $T_{g,ini}$  for all simulations was typically 1000 °C. In order

to make the calculations comparable to the experimental results, the mass flows as measured after the aerosol condensing heat exchangers, are used as input parameter for the calculations.

In Fig. 5.4 it can be observed that the calculated outlet temperatures for the heat exchangers are below 200 °C, satisfying the boundary conditions described. Conservation of mass, in combination with temperature dependent physical properties is applied to calculate the Reynolds number. It is sufficient to determine the Reynolds number near the flue gas outlet for investigation whether the flow is laminar because gases exhibit the property that the kinematic viscosity which is defined as  $\nu_g = \frac{\mu_g}{\rho_g}$  increases for decreasing temperatures. The Reynolds number based on the physical properties near the heat exchanger outlet was always below 2300.

### 5.3.4 Results from test runs with laminar flow shell and tube heat exchangers

#### Fuel characterisation

Chemical analyses of the fuel applied were performed to determine the moisture content as well as the ash content and the concentrations of the most relevant ash and aerosol forming elements. The results of these analyses are depicted in Tab. 5.2. Distinction is made between the different heat exchanger dimensions. Unfortunately, no fuel analyses were available for HE3. From Tab. 5.2 it can be observed that there are some differences in the fuel composition. In general the standard deviation of the elements in the fuel for HE1 are higher than the standard deviation for HE2. The reason for this is the fact that one fuel batch during test runs with HE1 contained significantly more ash and aerosol forming elements compared to the other two fuel batches.

The slightly higher ash content for HE2 compared to HE1 can be explained by the higher Ca and Si contents, which are both ash forming elements. Regarding the sodium content a strong difference can be observed between both fuels. Whereas the sodium content amounts to 100 mg/kg (d.b.) during experiments with HE1, the sodium content during experiments with HE2 was with 21 mg/kg (d.b.) almost a factor of 5 lower. Furthermore, it can be observed that the concentration of heavy metals in the fuel is rather low and showed some large fluctuations.

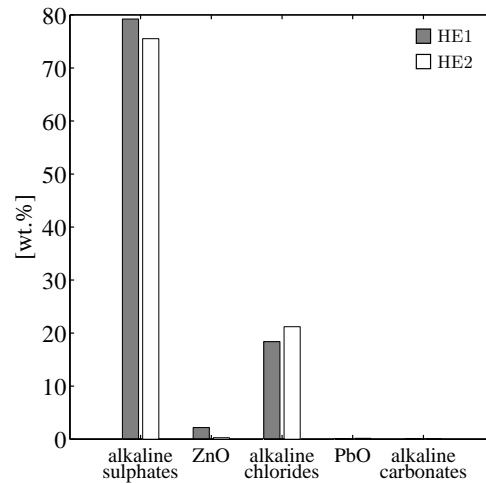
The flue gas composition and consequently also the maximum potential for aerosol formation is estimated as described in Sec. 3.2. Calculations showed that the total concentration of aerosol forming species released to the flue gas during experiments with HE1 were about 75 mg/Nm<sup>3</sup>. As all aerosol forming vapours are transformed into aerosol, calculations showed that almost 80 wt.% of the aerosols should consist of alkaline sulphate. Besides alkaline sulphate also a large share of alkaline chloride is calculated in the aerosols; more than 18 wt.%. The remaining small part mainly consists of ZnO (2 wt.%) and a small share of PbO (< 1 wt.%). The share of alkaline carbonate is almost not perceptible, << 1 wt.%. A graphical representation of the estimated aerosol composition is represented in Fig. 5.5.

The total estimated concentration of aerosol forming compounds in the flue gas during experiments with HE2 is of about 58 mg/Nm<sup>3</sup>. Calculations showed that,

**Table 5.2.** Composition wood chips used for the experiments.

Explanation: d.b. ... dry base; w.b. ... wet base; STD ... standard deviation.

parameter	unit	HE1	HE2
		average value & STD <sup>a</sup>	average value & STD <sup>b</sup>
Moisture	wt. % (w.b.)	29 ± 7.8	28 ± 1.8
Ash	wt. % (d.b.)	1.4 ± 0.6	0.9 ± 0.1
S	mg/kg (d.b.)	166 ± 39	134 ± 5
Cl	mg/kg (d.b.)	100 ± 52	80 ± 6
Ca	mg/kg (d.b.)	3063 ± 1020	2251 ± 364
Si	mg/kg (d.b.)	1028 ± 709	529 ± 480
Mg	mg/kg (d.b.)	312 ± 114	270 ± 17
K	mg/kg (d.b.)	930 ± 337	758 ± 119
Na	mg/kg (d.b.)	100 ± 1	21 ± 6
Zn	mg/kg (d.b.)	20 ± 19	8 ± 5
Pb	mg/kg (d.b.)	< 5 <sup>c</sup>	14 ± 6

<sup>a</sup> based on 3 fuel samples<sup>b</sup> based on 5 fuel samples<sup>c</sup> below detection limit**Figure 5.5.** Aerosol composition calculated from the fuel composition during experiments performed with the water cooled heat exchanger.

under the assumption that all aerosol forming vapours that are released to the flue gas are transformed into aerosols, 75 wt.% of the aerosols consists of alkaline sulphate

and 21 wt.% consists of alkaline chlorides. Furthermore, it is expected that the shares of PbO and ZnO are both  $< 1$  wt.%. Based on the provided fuel composition, it is expected that no alkaline carbonate are formed during experiments with HE2.

### Process control parameters

For the test runs it was relevant to keep the temperature upstream the heat exchanger as high as possible ( $\approx 1000$  °C) to avoid excessive nucleation of aerosol forming vapours in the secondary combustion zone. During experiments with HE3 quite stable temperatures around 1000 °C could be achieved in the secondary combustion zone, denoted by  $T_{sec}$  in Tab. 5.3 and 5.4.

**Table 5.3.** Overview over the average process conditions and corresponding standard deviation during the impactor measurements downstream the three different aerosol condensing heat exchanger designs.

Explanations:  $n$  ... number of coupled set of BLPI measurements;  $T_{sec}$  ... flue gas temperature in secondary combustion zone;  $T_{out}$  ... flue gas temperature in measurement section.

	HE1	HE2	HE3
$n$	13	26	6
$T_{sec}$ [°C]	$956.6 \pm 45.9$	$998.3 \pm 23.7$	$1000.4 \pm 5.9$
$T_{out}$ [°C]	$107.6 \pm 16.9$	$78.0 \pm 3.7$	$47.6 \pm 6.1$

**Table 5.4.** Overview over the average process conditions and corresponding standard deviation during the impactor measurements downstream the ordinary boiler.

Explanations:  $D_h$  ... hydraulic diameter;  $n$  ... number of coupled set of BLPI measurements;  $T_{sec}$  ... flue gas temperature in secondary combustion zone;  $T_{out}$  ... flue gas temperature in flue gas duct.

	HE1	HE2	HE3
$n$	13	26	6
$T_{sec}$ [°C]	$949.8 \pm 41.0$	$991.9 \pm 21.8$	$1000.4 \pm 5.9$
$T_{out}$ [°C]	$145.4 \pm 26.0$	$211.2 \pm 10.2$	$252.3 \pm 3.7$

On average, the temperature in the secondary combustion zone during experiments with HE1 was slightly lower, whereas the average temperature during experiments with HE2 was on average almost equal to that of test runs with HE3 (see Tab. 5.3 and Tab. 5.4). Concerning the standard deviations, experiments with HE1 and in less extend also for HE2 are much larger compared to test runs performed with HE3. This observation indicates that the conditions applied for test runs with HE1 and HE2 were not quite stable. However, it is expected that  $T_{sec}$  during all impactor measurements was high enough to avoid major particle formation before the heat exchanger inlet.

As the impactor measurements during test runs downstream the boiler and HE1 and HE2 were not performed perfectly isochronous, yields that  $T_{sec}$  during impactor measurements downstream the boiler (see Tab. 5.4) can deviate compared to  $T_{sec}$  during impactor measurements downstream HE1 and HE2 (see Tab. 5.3). Comparison show that this difference is on average less than  $7\text{ }^{\circ}\text{C}$ . As the impactor measurements during test runs downstream the boiler and HE3 are performed simultaneously, no difference can be observed regarding  $T_{sec}$ .

Comparing the measured flue gas temperatures downstream HE1 and HE2, then a rather good agreement between the measured and the theoretically determined flue gas temperatures can be observed, see Fig. 5.4. The measured flue gas temperature downstream HE3 is lower compared to what is predicted. One reason for this deviation is the absence of an insulation plate of the cold surface of the heat exchanger facing towards the furnace (see Sec. 5.3.1 and 5.3.2), most probably resulting in lower flue gas inlet temperatures and consequently also lower flue gas outlet temperatures, which will be discussed in more detail later on.

Comparing the flue gas temperatures downstream the boiler (see Fig. 5.4), it can be observed that the differences are quite large. The reason for these differences are most probably caused by the fact that during test runs with HE1 and HE2 the furnace was operating at partial load. Contrary to the coarse fly ash emissions, aerosol emissions are hardly influenced by the load (see, Brunner [9]). Because of this, aerosol emissions can still be compared to each other. Another possibility is that the biomass combustion plant in the age of the first test runs with HE1 was completely new. Consequently, the boiler tubes in the furnace were not contaminated with deposits, resulting in higher heat transfer rates compared to the situation when the boiler was contaminated with deposits.

## Impactor measurements

Aerosol emission measurements have been determined downstream the three heat exchangers tested as well as downstream the ordinary boiler. The aerosol emissions for HE1 are based on 13 repetitive BLPI measurement, whereas 26 BLPI measurements are performed in order to determine the aerosol emission for HE2. Regarding the experiments with the smallest tube dimension (HE3), only 6 repetitive measurements have been performed.

Aerosol concentrations (particles  $< 1\text{ }\mu\text{m}$ ) related to dry flue gas and  $13\text{ vol.}\%$   $\text{O}_2$  measured downstream the boiler and the three different aerosol condensing heat exchangers are presented in Fig. 5.6. The results in Fig. 5.6 are shown as box plots. The upper and lower limit of the boxes represent respectively the 1<sup>st</sup> and 3<sup>rd</sup> quartile of the measurement results, while the line in the boxes indicates the median value. The error indicators as shown in Fig. 5.6 represents respectively the minimum and maximum aerosol concentration.

In Fig. 5.6 it can be observed that the measured aerosol concentration downstream the boiler and the aerosol condensing heat exchanger during the experiments with HE1 and HE2 scattered much more than the aerosol concentration measured at the same positions during experiments with the smallest heat exchanger dimension (HE3). Furthermore, the trend can be observed that the aerosol concentrations downstream

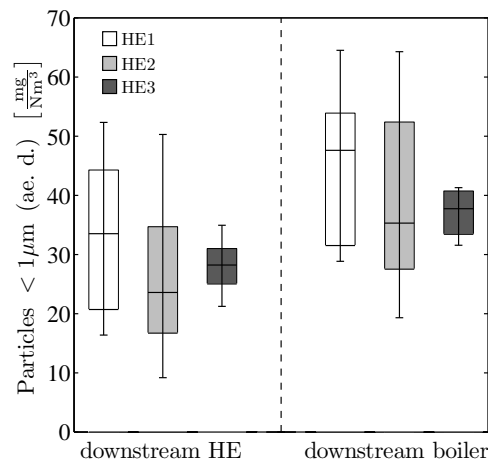


**Figure 5.6.** Concentration of aerosols in the flue gas sampled directly at boiler outlet and downstream the aerosol condensing heat exchangers at a flue gas temperature in the secondary combustion zone of approximately  $1000\text{ }^{\circ}\text{C}$ .

Explanations: All concentrations related to dry flue gas and  $13\text{ vol.}\% \text{ O}_2$ ; ae. d. ... aerodynamic particle diameter;  $D_h$  ... hydraulic diameter; number of BLPI measurements: HE1, 13 measurements; HE2, 26 measurements and HE3, 6 measurements; the boxes indicate the quartiles 25 % to 75 %, the line in the box displays the median value; the error indicator represents the maximum and minimum values.

the aerosol condensing heat exchangers are in general lower compared to the aerosol emissions downstream the boiler.

One reason for fluctuations in the aerosol emission is the fact that due to the inhomogeneity of the fuel the concentration of aerosol forming elements released to the flue gas changes. Consequently, the potential for aerosol formation also changes. Besides inhomogeneity of the fuel composition, there is also another important effect that causes fluctuations in the aerosol emissions in grate fired biomass combustion plants. When the grate is moving, fresh fuel becomes available for combustion. As the potential for aerosol formation is strongly depending on the stage of the combustion process, yields that the potential for aerosol formation strongly depends on the movement of the grate. As the movement of the grate was approximately 9 min. for full load, yields that concentration of aerosol forming species released to the flue gas also strongly fluctuates within this time. This observation is already mentioned in Brunner [9]. As impactor measurements are relatively short term measurements (sampling time  $\approx 3\text{ min.}$ ), the measured aerosol concentration depend on the actual fuel composition, as well as on the stage of the combustion process during the sampling periode.

The maximum potential for aerosol formation for test runs with HE2 based on fuel analysis and release factors obtained from literature (see, Tab. 3.1) is about  $58\text{ mg}/Nm^3$ , whereas the measured aerosol concentration is on average  $40.2\text{ mg}/Nm^3$ .

From this observation can be derived that measured aerosol concentration downstream the boiler is approximately 30 % less, compared to the estimated aerosol concentration. Apparently 30 % of the aerosols and aerosol forming vapours end up in the furnace and boiler.

Larger differences can be observed between estimated aerosol concentrations and measured aerosol concentration during test runs with HE1. Whereas the estimated aerosol concentration during experiments with HE1 amounts to  $75 \text{ mg}/\text{Nm}^3$ , the measured average aerosol concentrations amounts to  $43.6 \text{ mg}/\text{Nm}^3$ . This observation results in a difference of more than 40 %, based on estimated aerosol concentrations. One reason for this larger difference is caused by the fact that the fuel used for test runs with HE1 was less homogeneously (see Tab. 5.2). One fuel sample for test runs with HE1 contained much more aerosol forming elements compared to the other two fuel samples (up to 100 % more potassium and 50 % more sulphur). Consequently, the estimated concentration of aerosol forming species released to the flue gas also becomes significantly higher.

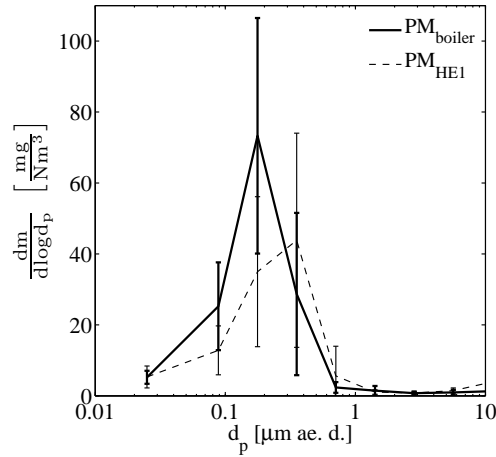


**Figure 5.7.** Typical particle size distributions, determined with a 9-stage Bernertype low pressure impactor (BLPI) downstream the ordinary boiler and HE1 ( $D_h = 12.50 \text{ mm}$ ). Explanations: All concentrations are expressed in in  $\text{mg}/\text{Nm}^3$  and related to dry flue gas and 13 vol.%  $\text{O}_2$ ; number of BLPI measurements: 13; subscript *boiler* ... boiler outlet; subscript *HE1* ... aerosol condensing heat exchanger outlet; ae. d. ... aerodynamic particle diameter.

The average particle size distributions for the different series of test runs are depicted in Fig. 5.7 to 5.9. All particle size distributions exhibit an approximately logarithmic normal distribution. Furthermore, it can be observed that the average PSD of the aerosols downstream the aerosol condensing heat exchangers as well as downstream the boiler always show one clear peak which is usually between  $0.125 \mu\text{m}$  and  $0.5 \mu\text{m}$ .

The PSD's of the aerosols downstream the aerosol condensing heat exchanger as

well as downstream the boiler regarding test runs with HE1 show quite large fluctuations, indicated by the relatively large error bars, see Fig. 5.7. As already mentioned, one fuel batch contained significantly more aerosol forming species compared to the other fuel batches. As this effect influences the total aerosol concentration (see, Fig. 5.6), this will also have an influence on the particle size distribution.

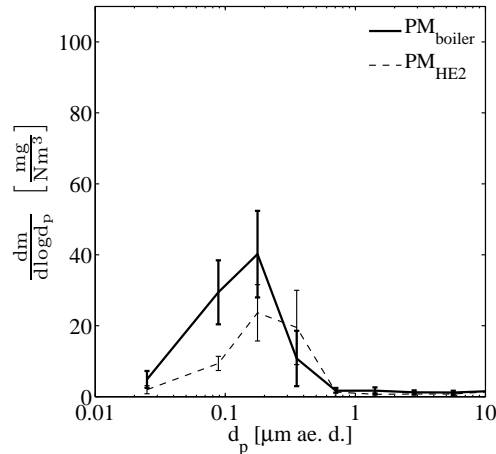


**Figure 5.8.** Typical particle size distributions, determined with a 9-stage Bernertype low pressure impactor (BLPI) downstream the ordinary boiler and HE2 ( $D_h = 6.20 \text{ mm}$ ).

Explanations: All concentrations are expressed in in  $\text{mg}/\text{Nm}^3$  and related to dry flue gas and 13 vol.%  $\text{O}_2$ ; number of BLPI measurements: 26; subscript *boiler* ... boiler outlet; subscript *HE2* ... aerosol condensing heat exchanger outlet; ae. d. ... aerodynamic particle diameter.

For the test runs performed with HE2 the average PSD of the aerosols downstream the boiler shows a distinct peak between  $0.125 \mu\text{m}$  and  $0.25 \mu\text{m}$ , see Fig. 5.8. Compared to the average PSD of the aerosols downstream the boiler during test runs with HE1, the peak of the average PSD of the aerosols for HE2 is not that high. This is mainly caused by the fact that the concentration of aerosol forming elements in the fuel during test runs with HE2 were lower and much more homogeneously compared to the aerosol forming elements in the fuel during test runs with HE1 (see Tab. 5.2). Consequently, the average PSD of the aerosols during test runs with HE2 as well as downstream the boiler during these measurements show less fluctuations compared to the PSD of the aerosols during test runs with HE1. For HE2, individual PSD's of the aerosols sampled downstream the heat exchanger tested were usually around the 3<sup>rd</sup> and 4<sup>th</sup> stage i.e. between particle sizes of  $0.125 \mu\text{m}$  and  $0.5 \mu\text{m}$ . This explains the relatively large fluctuations around these stages. In general, the average aerosol concentrations in each impactor stage during test runs with HE2 are lower than the average aerosol concentrations in the same impactor stages sampled downstream the boiler, indicating that this heat exchanger works as expected.

Test runs with HE3 show that the concentration particles  $> 0.5 \mu\text{m}$  downstream



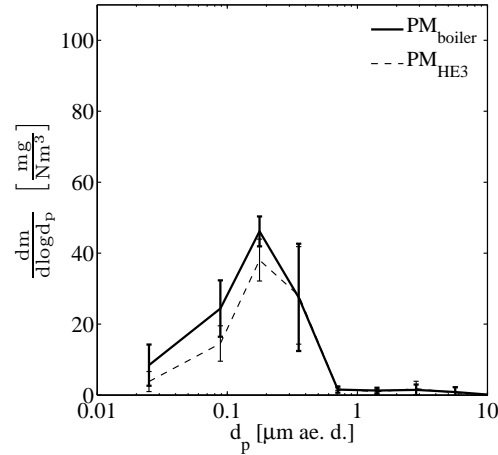


**Figure 5.9.** Typical particle size distributions, determined with a 9-stage Bernertype low pressure impactor (BLPI) downstream the ordinary boiler and HE3 ( $D_h = 1.07 \text{ mm}$ )  
 Explanations: All concentrations are expressed in in  $\text{mg}/\text{Nm}^3$  and related to dry flue gas and 13 vol.%  $\text{O}_2$ ; number of BLPI measurements: 6; subscript *boiler* ... boiler outlet; subscript *HE3* ... aerosol condensing heat exchanger outlet; ae. d. ... aerodynamic particle diameter.

the heat exchanger tested as well as downstream the boiler are negligible, see Fig. 5.9. Small differences in the average aerosol concentrations between the boiler and HE3 can be observed for cut diameters  $< 0.5 \mu\text{m}$ . As already could be observed in Fig. 5.6, this indicates that the aerosol emission reduction obtained by this heat exchanger is rather low.

Based on simultaneously performed BLPI measurements downstream the aerosol condensing heat exchangers and the boiler, the aerosol emission reduction is calculated for each coupled set of measurements. Performing multiple coupled sets of BLPI measurements and taking the average value of each aerosol emission reduction obtained by each coupled set of measurements results in an average aerosol emission reduction related to the ordinary boiler design  $\overline{\eta_{rel,exp}}$  (see Eq. 5.1).

The resulting average relative aerosol emission reductions  $\overline{\eta_{rel,exp}}$  obtained with the three different heat exchangers compared to ordinary boiler designs are depicted in Fig. 5.10. From theory (chapter 2, 3 and 4) it is expected that decreasing the tube dimensions of the aerosol condensing heat exchanger should result in lower aerosol emissions. However, in Fig. 5.10 can be observed that this theory only holds for test runs with HE1 and HE2. Test runs performed with HE1 shows a reduction of fine particulate matter compared to ordinary boiler designs of  $28 \pm 11 \%$ . Further decreasing the tube diameter of the aerosol condensing heat exchanger to  $6.20 \text{ mm}$  (HE2) results in an increasing aerosol emission reduction compared to ordinary boiler designs of  $36 \pm 14 \%$ . According to theory, the resulting aerosol emission reductions performed by test runs with HE3 ( $D_h = 1.07 \text{ mm}$ ) should be significantly higher compared to the previous aerosol condensing heat exchangers which have larger di-

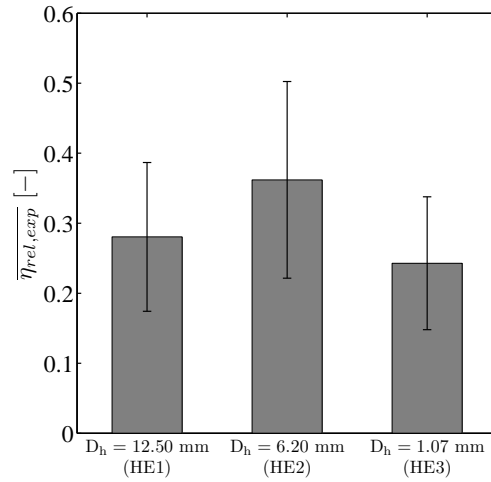


**Figure 5.10.** Overview of the average aerosol emission reductions obtained with the water cooled aerosol condensing heat exchangers compared to ordinary boiler design.

Explanations: Aerosol emission reductions are calculated according to Eq. 5.1; all aerosol emission reductions are expressed in in  $mg/Nm^3$  and related to dry flue gas and 13 vol.%  $O_2$ ; number of BLPI measurements: HE1, 13 measurements; HE2, 26 measurements and HE3, 6 measurements.

ameters. However, measurement results showed an opposite trend. Experiments with HE3 result in an average aerosol emission reduction of  $24 \pm 9$  %, which is the lowest of all three experimentally tested water cooled heat exchangers. Because of this unexpected trend, the working principle of HE3 is investigated in more detail.

### 5.3.5 Analysis of the working efficiency concerning HE3

In order to investigate why the trend resulting from the experiments performed with HE3 is not in agreement to what is theoretically expected, additional temperature measurements in front of this heat exchanger were performed. The reason for performing these measurements is inspired by the fact that no insulation plate is mounted on the side of this aerosol condensing heat exchanger facing towards the furnace, contrary to HE1 and HE2. As a result of this lack of insulation, heat transfer in front of the heat exchanger could be significantly, resulting in relatively low flue gas temperatures in the vicinity of the heat exchanger inlet. Subsequently, the aerosol forming vapours in front of the heat exchanger inlet can become supersaturated, resulting that particle formation and/or condensation can occur in that region. When these aerosol formation and/or condensation processes are already in an advanced stage, the basic principle of stimulating condensation of aerosol forming vapours on heat exchanger surfaces becomes suppressed, resulting in lower fine particulate emission reductions. In order to verify this statement the flue gas temperature on three positions at a dis-

tance of 30 mm from the heat exchanger inlet was measured. The three temperature measurement positions are shown in Fig. 5.3 and are indicated by  $T_{right}$ ,  $T_{middle}$  and  $T_{left}$ .

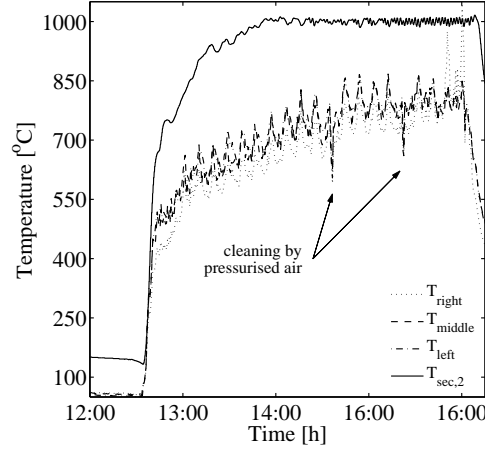


**Figure 5.11.** Flue gas temperatures in front of HE3 ( $D_h = 1.07$  mm). The measurement positions  $T_{right}$ ,  $T_{middle}$  and  $T_{left}$  are shown in Fig. 5.3, whereas the position of the flue gas temperature in the secondary combustion zone  $T_{sec}$  is shown in Fig. 5.1

One important parameter for the furnace control is the flue gas temperature inside the secondary combustion zone  $T_{sec}$ . Its measurement position is upstream the aerosol condensing heat exchanger inlet, see Fig. 5.1. In comparison to the thermocouple measuring  $T_{sec}$ , the thermocouples close to the heat exchanger inlet are influenced by radiative heat transfer from the thermocouple towards the cold plate of the heat exchanger. Therefore, it is necessary to correct the measured temperature for radiative heat loss. An estimation of the radiative heat loss is made by writing the energy balance over the thermocouple. In a steady state situation, the convective heat transfer is a product of the radiative heat loss from the thermocouple towards the cold surface of the heat exchanger and conduction inside the thermocouple itself. Under assumption of negligible conduction inside the thermocouple, which is reasonably valid for small thermocouple dimensions of 1 mm, the convective heat transfer is in balance with the radiative heat transfer, so that the corrected flue gas temperature is given by:

$$T_g = T_{tc} + \frac{\epsilon_k k_b}{h_{tc}} (T_{tc}^4 - T_{surf}^4) \quad (5.4)$$

where  $T_g$  is the flue gas temperature whereas  $T_{tc}$  and  $T_{surf}$  are respectively the temperature measured by the thermocouple and the cold heat exchanger surface that is typically 200 °C. In Eq.5.4,  $k_b$  is Boltzmann's constant and  $D_{tc}$  is the thermocouple diameter which is 1 mm. A typical value for the emissivity  $\epsilon_k$  is 0.8 (see VDI [51]),

whereas  $h_{tc}$  is the convective heat transfer coefficient which is approximately  $30 \frac{W}{m^2K}$  determined by a Nusselt relation.

If  $T_{sec}$  is high enough, major aerosol formation inside the secondary combustion zone should be suppressed. This statement is supported by measurement results by use of high temperature low pressure impactor (HT – LPI) described in Brunner [9]. In Fig. 5.11 it can be observed that  $T_{sec}$  is quite stable at approximately  $1000 \text{ }^\circ\text{C}$  in the time period between 14.00 and 16.00 hours. On measuring the flue gas temperature in front of the heat exchanger at positions as shown in Fig. 5.3 simultaneously, it can be observed that the flue gas inlet temperature was on average approximately  $240 \text{ }^\circ\text{C}$  lower than what was expected based on information provided by the thermocouple measuring  $T_{sec}$ . Due to this significant temperature drop in front of the heat exchanger it is expected that aerosol formation and condensation could already occur before the flue gas enters the heat exchanger. Consequently, a part of the aerosol forming vapours that should condense on heat exchanger surfaces is now already transformed into particles which are much more difficult to precipitate from the flue gas compared to the aerosol forming vapours (see Fig. 4.5).

One major practical limitations during the measurements was that heat exchanger passages of the size of  $1.07 \text{ mm}$  were extremely sensitive to blocking with coarse fly ash particles, resulting in an increase of the pressure drop over the heat exchanger. Consequently, the mass flow rate decreases, resulting a reduction of the heat exchanging efficiency. To minimise the pressure drop, the heat exchanger passages had to be cleaned almost once per hour. Due to the narrow structure of the heat exchanger mechanical cleaning was rather difficult. Contaminants in the heat exchanger passages were removed by means of blowing pressurised air in counterflow direction. In this way the pressure drop over the heat exchanger rapidly decreased.

Another practical limitation is that manufacturing a water cooled heat exchanger with heat exchanger passages in the millimetre regime is very labour intensive and requires dedicated production methods that are much more expensive than ordinary production methods. As a result of this it is expected that the production costs for such heat exchangers are even in mass fabrication far too high to become economically attractive.

### Chemical composition of aerosols sampled downstream the boiler and the aerosol condensing heat exchanger

Wet chemical analysis of the first four BLPI-stages from measurements downstream one test run with HE2 as well as downstream the ordinary boiler were performed in order to gain insight whether the heat exchanger design influences the chemical composition of the aerosols emitted. In Fig. 5.12, the element composition of aerosols are depicted. Furthermore, also the emission reduction per element is included, which is calculated according to the relation, given in Eq.5.2. The average flue gas temperature in the furnace during the impactor measurements was about  $910 \text{ }^\circ\text{C}$ .

In Fig. 5.12, it can be observed that the aerosols mainly consist of K, Cl and S. The contribution of Na, Zn and Pd is of minor interest regarding the total aerosol emission. From the data it can be derived that K, Na and S were all reduced by

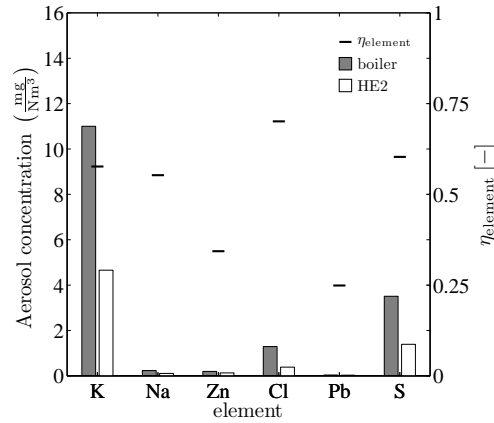


**Figure 5.12.** Comparison of the concentration of aerosol forming elements at boiler outlet and downstream HE2 ( $D_h = 6.20 \text{ mm}$ ) at flue gas temperatures in the secondary combustion zone of about  $910 \text{ }^\circ\text{C}$ .

Explanation: All concentrations related to dry flue gas and  $13 \text{ vol.}\% \text{ O}_2$ .

approximately 55 %, which is in agreement with the total aerosol emission reduction which was 53 % for that particular measurement. Contrary to this, the reduction of Cl was much higher. This is caused by the fact that Cl is mainly bound as KCl. As KCl condenses at rather low temperatures ( $\approx 600 \text{ }^\circ\text{C}$ ), almost no KCl is condensed before the heat exchanger inlet. Consequently, this compound can high efficiently be precipitated in the aerosol condensing heat exchanger.

The reduction of Zn in the aerosols was rather low, (34 %). The reason for this is the fact that after oxidisation, the resulting saturation vapour pressure of ZnO is rather low. Consequently, a large share of ZnO is already transformed into particles before it enters the heat exchanger. As the precipitation efficiency of the heat exchanger for particles is rather low, most of the ZnO is emitted.

In Fig. 5.13, comparison of the chemical composition of the aerosols sampled downstream HE2 and downstream the boiler are depicted. Besides this, also an estimation of the aerosol composition based on the fuel composition (see Tab. 5.2) and release factors obtained by literature (see Sec. 3.2) is included.

In Fig. 5.13 it can be observed that the estimated concentration of alkaline sulphate based on fuel analysis (75 wt.%) is slightly lower compared to the wet chemical analysis performed for the aerosols sampled downstream the boiler (79 wt.%). Regarding the alkaline sulphate concentration, slightly lower values (74 wt.%) can be observed in the aerosols downstream HE2.

As the flue gas that is flowing to the boiler has to pass two combustion zones and a firetube before it enters the boiler, the residence time at high temperatures is longer compared to the situation when the flue gas flows to the aerosol condensing heat exchanger (see Fig 5.1). Because the sulphation process as described in Sec. 3.2 is strongly time and temperature dependent, yields that this process is kinetically

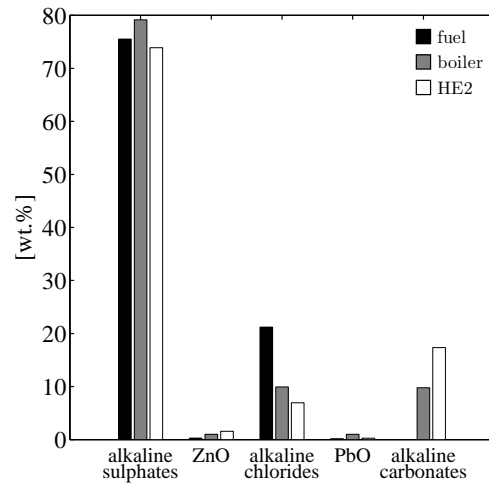


**Figure 5.13.** Comparison of the aerosol composition based on a fuel analysis and determined by wet chemical analysis of the aerosols sampled downstream the boiler outlet and downstream HE2 ( $D_h = 6.20 \text{ mm}$ ) at flue gas temperatures in the secondary combustion zone of about  $910 \text{ }^\circ\text{C}$ .

Explanation: All concentrations related to dry flue gas and  $13 \text{ vol.}\% \text{ O}_2$ .

limited. As a result of this lower concentrations of KCl and KOH can be transformed into alkaline sulphate. Consequently, a larger KOH concentration is available that, together with  $\text{CO}_2$ , can be transformed into alkaline carbonate. This trend can clearly be observed in Fig. 5.13, which shows a alkaline carbonate concentration in the aerosols sampled downstream HE2 of  $17 \text{ wt.}\%$ , whereas the concentration in the aerosols sampled downstream the boiler amounts to  $10 \text{ wt.}\%$ . Based on the fuel analyses and release factors, no alkaline carbonate is expected. From the wet chemical analysis it can also be observed that the alkaline chloride concentration downstream the boiler ( $10 \text{ wt.}\%$ ) and the aerosol condensing heat exchanger ( $7 \text{ wt.}\%$ ) are both lower than what is expected, based on fuel analyses and release factors obtained by literature ( $18 \text{ wt.}\%$ ). This can be caused by several mechanisms. The most obvious reason is that the Cl concentration in the flue gas was lower than what was expected, also resulting in higher alkaline carbonate concentrations. However, this does not explain the difference in alkaline chloride concentrations between the aerosol condensing heat exchanger and the boiler. The reason for this is most probably caused by the fact that a part of the Cl is already condensed on heat exchanger surfaces instead of transformed into aerosol particles, the aim of the aerosol condensing heat exchanger.

Concerning the PbO content a small share can be observed downstream the boiler, whereas almost no PbO can be observed downstream the heat exchanger tested as well as based on calculations. However, as already mentioned, these concentrations are so low that almost no conclusion can be derived from this observation. Furthermore, based on the procedure as outlined in Sec. 3.2, a small share of ZnO is expected

(2 wt.%). Wet chemical analysis showed that the ZnO concentration in aerosols downstream the boiler is about 1 wt.%, whereas the ZnO concentration downstream HE2 is almost 2 wt.%. As already mentioned, ZnO is mainly formed immediately above the fuel bed after which a substantial part of it is able to nucleate homogeneously. As condensation prevail instead of particle precipitation in the aerosol condensing heat exchanger, the absolute concentration of ZnO particles downstream the boiler and the aerosol condensing heat exchanger are almost equal (see also Fig. 5.12). As a part of the total aerosol emission, ZnO will increase when the other substances are condensed in the heat exchanger. This explains the higher concentration ZnO downstream the aerosol condensing heat exchanger.

## 5.4 Compact laminar counterflow gas to gas heat exchanger

Experiments performed with a water cooled heat exchanger having a tube diameter of 1.07 mm (HE3) were not successful. Due to the lack of insulation in front of the heat exchanger inlet, heat transfer in the vicinity of the heat exchanger inlet was already significant, resulting in lower flue gas temperatures before the flue gas enters the convective path. While a flue gas inlet temperature of approximately 1000 °C was expected, based on temperature measurements inside the secondary combustion zone, the flue gas inlet temperature in the vicinity of the heat exchanger inlet was approximately 760 °C. As a result of this relatively low temperature, aerosol formation already occurred in front of the heat exchanger inlet resulting in a deficient condensation rate of aerosol forming vapours on heat exchanger surfaces.

To check the validity of the approach a 20 kW<sub>th</sub> narrow channeled gas to gas heat exchanger originally developed for recuperative burners (see, Van Kemenade [47, 49]) was used as an aerosol condensing heat exchanger. For the sake of simplicity this heat exchanger will be denoted as HE4. Due to its construction, radiative heat transfer was minimised such that particle formation in front of the heat exchanger is suppressed.

### 5.4.1 Description of HE4, the compact laminar counterflow gas to gas heat exchanger

The gas to gas heat exchanger is made of heat resistant stainless steel. To obtain a sufficient heat exchanging surface the heat exchanger is constructed as a counter flow heat exchanger in between two halves of a cross flow heat exchanger. Furthermore, the plates are formed such that each cooling channel is in full contact with a flue gas channel. A scheme of the compact laminar counterflow gas to gas heat exchanger is depicted in Fig. 5.14.

The flue gas inlet of the heat exchanger is connected with the secondary combustion zone of the pilot-scale furnace. A mass flow controller with a maximum capacity of 1.25 Nm<sup>3</sup>/min (not shown in Fig. 5.14) was used to achieve a constant mass flow of the cooling air through the gas to gas heat exchanger. The hot cooling air is freely exhausted. The ducts are isosceles triangles with a base of 6 mm and a height of

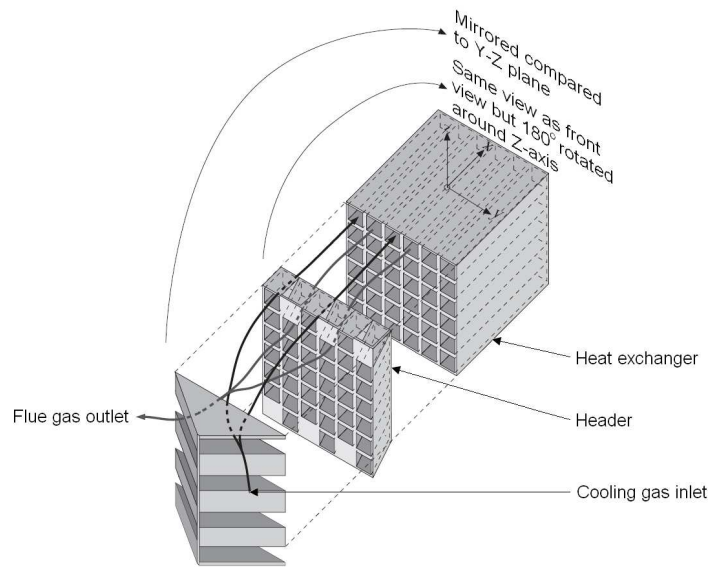


**Figure 5.14.** Schematic picture of the used gas to gas heat exchanger, originally developed to transfer 20 kW of heat.

2.5 mm. All angles are rounded with with a radius of 1 mm, resulting in a hydraulic diameter of approximately 2.22 mm. The channels depicted in Fig. 5.14, are drawn as square ducts to illustrate the counter current flow concept of this gas to gas heat exchanger. Each row of the gas to gas heat exchanger consists of 28 channels, whereas the number of rows is 75. The connection of the channels and the housing on both sides of the heat exchanger is accomplished by a header, which consists of a three dimensional structure. The effective length of the heat exchanger is 100 mm, whereas the maximum entrance length of the header on the furnace side is 55 mm. The exit length of the header (not drawn in Fig. 5.14) varies due to the complex geometry between 4 mm and 130 mm.

### 5.4.2 Design calculations concerning HE4

Due to the complex geometry of the gas to gas heat exchanger a numerical code originally developed by Van Kemenade [47] is used to determine the temperature profile. For the calculation, equal heat capacity flows ( $\dot{m}c_p$ ) and a fully developed laminar flow profile were assumed for both media.

The temperature profile for both the flue gas and the cooling air flow as a function of the normalised length by neglecting the entrance effects is depicted in Fig. 5.15. For the calculations an initial flue gas temperature and an initial cooling air temperature of respectively 1000 °C and 20 °C were assumed. In Fig. 5.15 it can be observed that the calculated outlet temperature of the flue gas for equal capacity flows should be lower than 200 °C, which should be sufficient in order to complete the condensation



process.

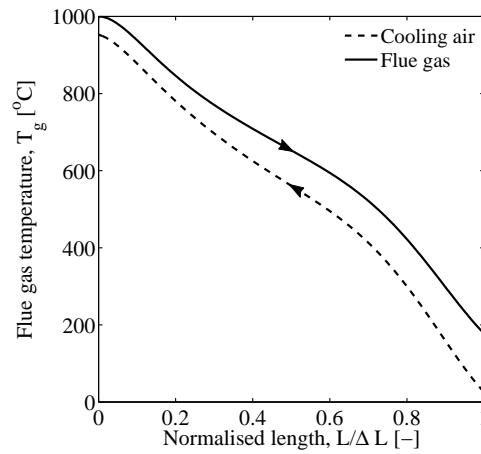


**Figure 5.15.** Calculated flue gas and cooling air temperature in the gas to gas heat exchanger (HE4) as a function of the normalised length.

### 5.4.3 Results from test runs with HE4

The application of a gas to gas heat exchanger was inspired by the fact that using this heat exchanger type relatively easily information can be provided on the working principle of the aerosol condensing heat exchanger. Because of this no fuel analysis data nor wet chemical analysis were performed during experiments with this heat exchanger type.

### Process control parameters

During the BLPI measurements downstream HE4 and the ordinary boiler  $T_{sec}$  was quite stable around 1000 °C, see Tab. 5.5. Deviations between the theoretically determined flue gas outlet temperature and the measured flue gas temperature downstream the gas to gas heat exchanger (HE4) are caused by the fact that the gas to gas heat exchanger was originally developed to transfer 20 kW of heat, whereas the heat transferred during the experiments was limited to approximately 7.5 kW. The reason for this lower heat transfer was caused by the fact that transferring 20 kW of heat corresponds to a pressure drop of 1000 Pa, exceeding the maximum pressure drop of 350 Pa. Due to the limited capacity of the flue gas fan, not the full capacity of the heat exchanger could be used. Consequently, the gas to gas heat exchanger was not well balanced resulting in lower flue gas temperatures at the outlet.

**Table 5.5.** Overview over the average process conditions during the impactor measurements downstream the gas to gas heat exchanger (HE4) and the ordinary boiler.

Explanations:  $n$  ... number of coupled set of BLPI measurements;  $T_{sec}$  ... flue gas temperature in secondary combustion zone;  $T_{out}$  ... flue gas temperature in measurement section.

	HE4	Boiler
$n$	6	6
$T_{sec}$ [°C]	$1004 \pm 28$	$1004 \pm 28$
$T_{out}$ [°C]	$67 \pm 18$	$216 \pm 4$

### Impactor measurements

Six BLPI measurements downstream HE4 as well as downstream the ordinary boiler were performed to determine the concentration of aerosols and the average particle size distribution of the aerosols.

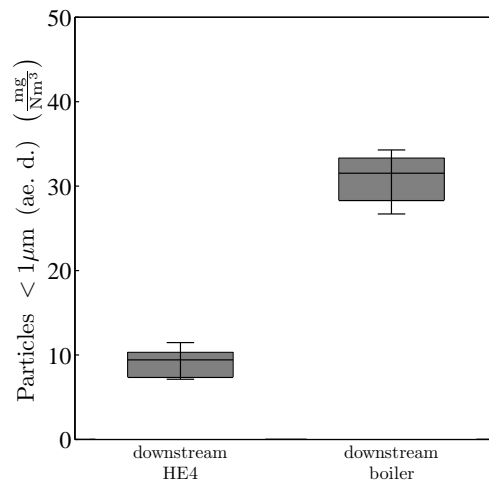


**Figure 5.16.** Concentration of aerosols in the flue gas sampled directly at boiler outlet and downstream HE4 ( $D_h \approx 2.22$  mm) at a flue gas temperature in the secondary combustion zone of approximately 1000 °C.

Explanations: All concentrations related to dry flue gas and 13 vol.%  $O_2$ ; ae. d. ... aerodynamic particle diameter; number of BLPI measurements: boiler outlet 6, at heat exchanger outlet 6; the boxes indicate the quartiles 25 % to 75 %, the line in the box displays the median value; the error indicator represents the maximum and minimum values.

Aerosol concentrations (dry flue gas and 13 vol.%  $O_2$ ) measured downstream HE4 and the boiler are presented in Fig. 5.16. The results in Fig. 5.16 are shown as box plots. The upper and lower limit of the boxes represent respectively the 1<sup>st</sup> and 3<sup>rd</sup>

quartile of the measurement results, while the line in the boxes indicates the median value. The error indicators as shown in Fig. 5.16 represents respectively the minimum and maximum aerosol concentration.

In Fig. 5.16 it can be observed that average aerosol concentration downstream the boiler was  $30.9 \text{ mg}/\text{Nm}^3$ . Because no fuel analysis was available, no comparison between expectations based on release factors from literature can be made. The concentration of aerosols downstream HE4 amounted to  $9.2 \text{ mg}/\text{Nm}^3$ , which is significantly lower compared to previous observations with HE1 to HE3, indicating that the aerosol emission reduction obtained by HE4 is much higher.

The average PSD of the aerosols downstream HE4 and the boiler are depicted in Fig. 5.17. In Fig. 5.17 a clear peak regarding the PSD of the aerosols downstream the heat exchanger can be observed which is between a particle size of  $0.125 \text{ }\mu\text{m}$  and  $0.25 \text{ }\mu\text{m}$ , whereas the aerosol peak after the boiler is between cut diameters of  $0.125 \text{ }\mu\text{m}$  and  $0.5 \text{ }\mu\text{m}$ . Furthermore, it can be observed that the average concentration of particles for each particle size class downstream HE4, is lower compared to the concentration measured downstream the boiler resulting in an aerosol emission reduction, much higher compared to previous observations with HE1 to HE3.

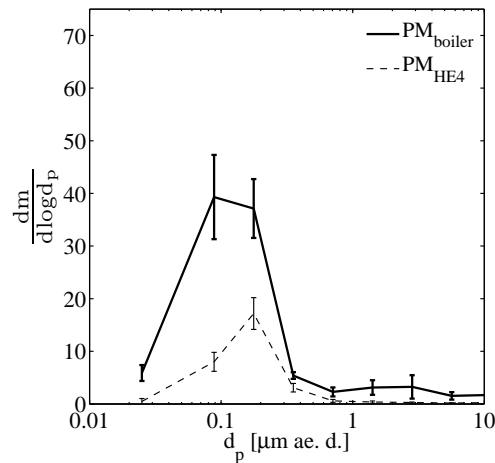


**Figure 5.17.** Typical particle size distributions, determined with a 9-stage Bernertype low pressure impactor (BLPI) downstream HE4 ( $D_h = 2.22 \text{ mm}$ ). Explanations: All concentrations are expressed in  $\text{mg}/\text{Nm}^3$  and related to dry flue gas and  $13 \text{ vol.}\% \text{ O}_2$ ; number of BLPI measurements: 6; subscript *boiler* ... boiler outlet; subscript *HE4* ... aerosol condensing heat exchanger outlet; ae. d. ... aerodynamic particle diameter.

The measured aerosol concentrations of each coupled set of measurement downstream both the gas to gas heat exchanger and the boiler as well as the resulting fine particulate emission reduction obtained by each measurement are depicted in Fig. 5.18. From results depicted in Fig. 5.18 it can be observed that the aerosol emission reductions were quite constant for all six measurements. The resulting average fine particulate emission reduction was  $70 \pm 3 \%$ . This observation gave the desired

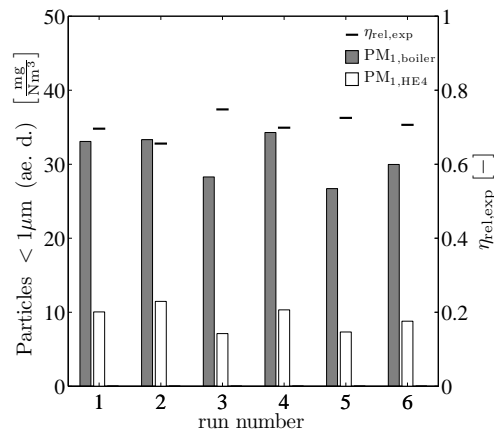


**Figure 5.18.** Overview of the measured particle fraction  $< 1 \mu\text{m}$  determined with a 9-stage Bernertype low pressure impactor (BLPI) downstream the ordinary boiler and the gas to gas exchanger outlet and the corresponding fine particulate emission reduction  $\eta_{rel,exp}$  calculated according to Eq. 5.1.

Explanations: All concentrations are related to dry flue gas and 13 vol.%  $O_2$ ; number of BLPI measurements: 6; subscript *boiler* ... boiler outlet; subscript *HE* ... aerosol condensing heat exchanger outlet; ae. d. ... aerodynamic particle diameter.

result that condensation of aerosol forming vapours on heat exchanger surfaces indeed can be stimulated.

## 5.5 Comparison of experiments with theory

A comparison between measurement results and simulation results are made to check the trend that decreasing tube dimensions indeed result in higher fine particulate emission reductions, as described in chapters 2 - 4. For simulations, inlet conditions as described in Tab. 3.2 are used in compliance with the fact that no insulation material is applied around the tubes. These conditions are in first order approximation comparable to the conditions as used during the experiments with experimentally tested water cooled heat exchangers. For comparison, the plug flow model (chapter 3) as well as the 2D model (chapter 4) have been subjected to the experimental results.

The particulate emission reductions obtained by the simulation results are directly related to the concentration of aerosol forming compounds in the flue gas (see Eq. 4.21). Contrary to this, the experimental results are related to the particulate matter emissions downstream the boiler (see Eq. 5.1). When no aerosol forming compounds condense in the boiler and no particles are precipitated in the firetube and the boiler, direct comparison is permitted. However, as already mentioned in Sec. 5.3.4, approximately 30 % of the aerosol forming compounds that are released from the fuel to the flue gas cannot be detected downstream the boiler. Consequently, the theoretical absolute particulate emission reductions,  $\eta_{abs,theo}$  (simulation results), are always

higher compared to the relative particulate emission reduction,  $\eta_{rel,theo}$  (experimental results). To make the experimentally determined results comparable to what is expected based on the models derived, losses of these aerosols and aerosol forming vapours have to be considered. Because of this, a relation between the theoretical relative particulate emission reduction,  $\eta_{rel,theo}$ , and the theoretical absolute particulate emission reduction,  $\eta_{abs,theo}$ , is given such that the measurement results could be compared to what is theoretically expected, which is:

$$\eta_{rel,theo} = \frac{\eta_{abs,theo} - \eta_{boiler}}{1 - \eta_{boiler}}, \quad (5.5)$$

The absolute concentration of aerosols and aerosol forming species ending up in the fretube and the boiler is represented by  $\eta_{boiler}$ , and amounts to 30 % (see Sec. 5.3.4).

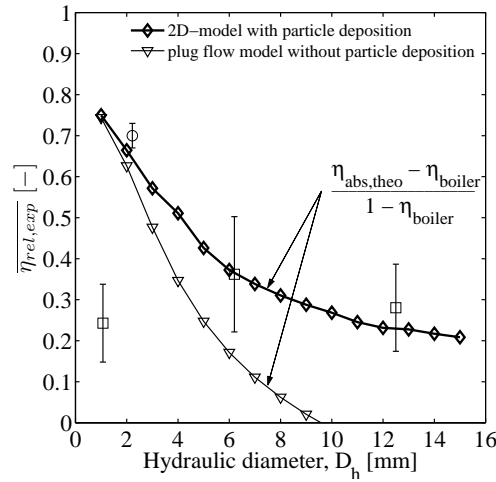


**Figure 5.19.** Theoretical calculated fine particulate emission reductions compared with average measured fine particulate emission reductions obtained with different aerosol condensing heat exchanger designs related to ordinary boiler design,  $\overline{\eta_{rel,exp}}$ .

Explanations: All concentrations are related to dry flue gas and 13 vol.%  $O_2$ ;  $\square$  ... laminar flow water cooled heat exchangers (see Sec. 5.3);  $\circ$  ... gas to gas heat exchanger (see Sec. 5.4); continuous line with  $\diamond$  ... theoretical predicted fine particulate emission reduction compared to ordinary boiler design according to model as described in chapter 4.  $\eta_{boiler}$  ... concentration of particles and aerosol vapours that end up on surfaces in the fretube and in the boiler.

A comparison between theoretically predicted aerosol emission reductions and measured aerosol emission reductions is depicted in Fig. 5.19. Comparing both models (plug flow model without particle deposition and 2D model with particle deposition) to each other, then large differences can be observed, especially for increasing tube dimensions. The reason for this trend is already given in Sec. 4.3.2. For increasing tube diameter, the wall condensation process becomes of less importance. Consequently, more aerosols are formed, resulting in that particle deposition by external

forces becomes of more importance. However, to predict the aerosol emission reductions by use of numerical simulations, an expansion from the plug flow model to a 2D model was required. Therefore, the additional effort to expand the plug flow model to a 2D model was justified.

Despite uncertainties regarding the fuel composition, actual release rates of aerosol forming elements, and scattering measured aerosol emission reductions, still a good agreement can be observed for the 2D model. The experiments with HE1 and HE2, are in agreement with simulation results. Furthermore, it can be observed that the results obtained with HE3 is an outlier, which is already explained in Sec. 5.3.5.

Direct comparison between the experimental results obtained with HE4 and the simulation results as shown in Fig. 5.19 is strictly speaking not permitted. This is caused by several effects. First of all, simulations are performed for firetube boilers with a constant wall temperature, whereas the wall temperature in the gas to gas heat exchanger is essentially not constant. This implies that the resulting axial temperature gradient of the flue gas is much lower than in water cooled heat exchangers. As described in Sec. 3.8.4, it is expected that this should result in increasing fine particulate emission reductions. However, this effect becomes of minor importance for smaller channel dimensions. Comparing the obtained fine particulate emission reduction with the simulation results as presented in Fig. 5.19, the measured fine particulate emission reduction obtained with the gas to gas heat exchanger is in agreement with expectations. This finding confirms the trend that decreasing the hydraulic diameter of the channels indeed results in significant aerosol emission reductions.



## Chapter 6

# Experiments: Towards a commercial design

In chapter 5 it is proven that decreasing the channel dimensions into the millimetre regime indeed results in significant aerosol reductions compared to ordinary boiler designs. Aerosol emission reductions up to 70 % can be achieved using a gas to gas heat exchanger with a hydraulic diameter of approximately 2.22 mm (HE4). However, using a gas to gas heat exchanger for small-scale biomass applications is not meaningful. Therefore, new heat exchangers were designed subjected to the same boundary conditions as described in Sec. 5.2.2 exhibiting geometries that are from an economic point of view more attractive. Besides boundary conditions as described in Sec. 5.2.2 and a more attractive design, the newly designed heat exchangers should also be able to heat up water directly.

To determine the aerosol emission reductions of the new heat exchanger designs, the same setup, measurement procedure and calculation procedure as described in Sec. 5.2 were applied. Apart from determining the PSD of the aerosols by use of BLPI measurements downstream the boiler and the heat exchanger tested, also high-temperature-low-pressure-impactor HT – LPI measurements inside the secondary combustion zone were performed for the new heat exchanger designs. The working principle of this impactor is identical to the working principle of the BLPI, except that this device can operate at temperatures up to 1000 °C. Therefore, it is possible to determine the aerosol concentration in the hot flue gas before it enters the convective path by use of this HT – LPI. A detailed description of this impactor is given by Brunner [9]. For analysing the chemical composition of the aerosols sampled, also SEM/EDX analyses as described in Brunner [9] were performed.

### 6.1 Insulated plate type heat exchanger

The results obtained with the gas to gas heat exchanger (HE4), as described in Sec. 5.4, showed significant reductions of fine particulate matter emissions. Since water is commonly employed as cooling medium in biomass combustion plants, an



alternative heat exchanger design is made combining the functions of water heating and reduction of fine particulate matter. Furthermore, the heat exchanger passages should have a good accessibility, so that the heat exchanger can easily be cleaned.

### 6.1.1 Description of HE5, insulated plate type heat exchanger

As an intermediate step towards a more commercial heat exchanger design, a  $7.5 \text{ kW}_{\text{th}}$  prototype heat exchanger was produced and tested. As for the previous heat exchangers tested, also an abbreviate notation is used to refer to this heat exchanger, denoted by HE5. As the capacity flow ( $\dot{m}c_p$ ) of the cooling water is by far larger than the capacity flow of the flue gas, the flow configuration is not relevant (van Kemenade [49]) and a cross flow pattern was adopted. In order to achieve better accessibility plates instead of tubes were employed. The plate distance should be sufficiently large such that blocking with coarse fly ash particles is prevented, e.g. large hydraulic diameters are required. As can be observed from theory, large hydraulic diameters in combination with a sufficient particulate emission reduction is only possible by toning down the flue gas temperature decrease. In order to achieve this, insulation material was applied between the flue gas passages and the cooling water sides. A schematic representation of the resulting heat exchanger is shown in Fig. 6.1.

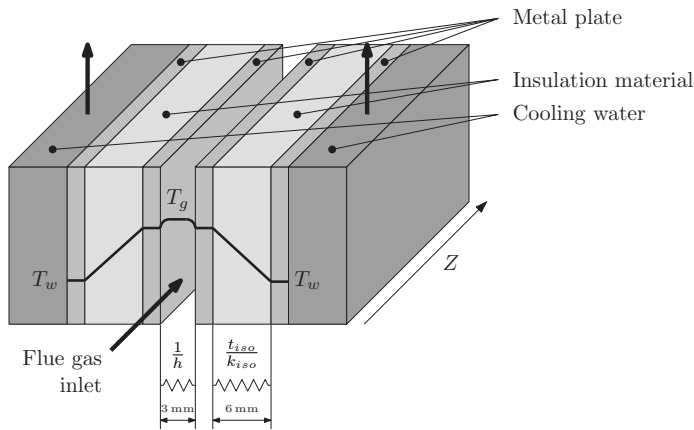


**Figure 6.1.** Schematic picture of insulated plate type heat exchanger (HE5)

One passage of the heat exchanger consists of two heat resistant parallel plates. The flue gas temperature will drop very rapidly when cooling water channels are in direct contact with the flue gas. Supported by the results as described in Sec. 3.8.4 it is expected that the right combination of insulation thickness and channel dimension results in a significant reduction of fine particulate matter emissions.

The heat exchanger that is designed and produced consists of a frame, made of a top and bottom header connected with each other via 16 rows of tubes, see Fig. 6.2. The distance between the top and bottom header is  $374 \text{ mm}$ . Cooling water flows through the headers and the tubes. Each row of tubes consists of 15 rectangular tubes

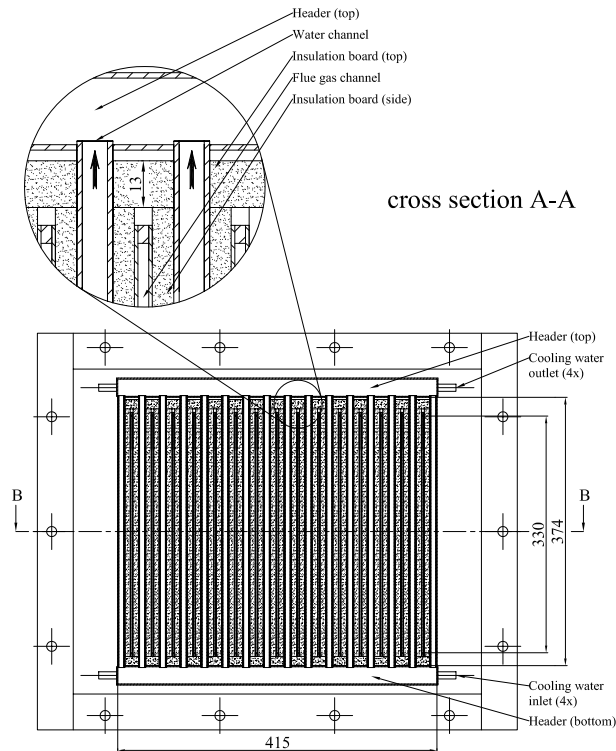


**Figure 6.2.** Cross sectional front view A – A of Fig. 6.3 of the insulated plate type heat exchanger (HE5).

with dimensions of  $30 \times 10 \times 1.5 \text{ mm}$ , welded to each other on the short side, resulting in tube rows of  $450 \text{ mm}$  length, see Fig. 6.3. The total width of the heat exchanger is  $415 \text{ mm}$ . So the frame consist of 15 openings with a height of  $374 \text{ mm}$  and a width of  $17 \text{ mm}$  wherein the flue gas channels that are covered with insulation material are positioned.

All sides of the flue gas channels, made of  $1 \text{ mm}$  thick heat resistant stainless steel AISI 310, are covered with insulation board. Based on the commercial availability of the insulation material, a  $6 \text{ mm}$  thick insulation board is used to cover both sides of the flue gas channel, whereas a  $13 \text{ mm}$  thick insulation board is used to cover the top and bottom part of the flue gas channel. The tubes on the furnace side through which the water flows are covered with a  $20 \text{ mm}$  thick insulation board to avoid radiative heat transfer. In this way a high flue gas inlet temperature could be achieved, such that nucleation and condensation of aerosol forming vapours near the inlet of the heat exchanger is assumed to be suppressed. Using these dimensions the resulting heat exchanger passage has a width of  $3 \text{ mm}$ , whereas the height of the flue gas passage is

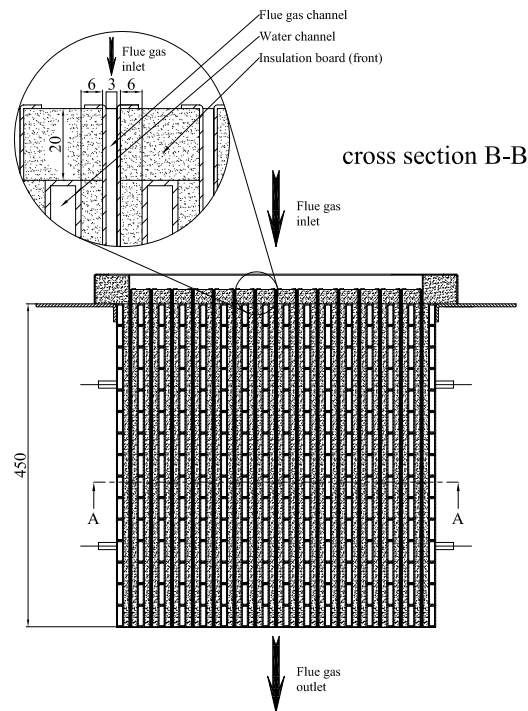


**Figure 6.3.** Cross sectional top view B – B of Fig. 6.2 of the insulated plate type heat exchanger (HE5).

330 mm, resulting in a hydraulic diameter  $D_h \approx 6 \text{ mm}$ . It is noticed that choosing a flue gas passage with a plate distance of 3 mm was not based on any scientific background but was only determined based on experience. It is expected that using such flue gas passage dimension is sufficient to avoid major problems by blocking with coarse fly ash particles.

Based on the results shown in Fig. 3.10, it is expected that due to stimulated condensation of aerosol forming vapours on heat exchanger surfaces only, fine particulate emission can be reduced by approximately 65 %. Furthermore, thermophoresis causing a particle movement towards the channels, will result in an additional fine particulate emission reduction, such that the final fine particulate emission reduction applying a flue gas temperature of approximately 1000 °C will be higher.

### 6.1.2 Design calculations concerning HE5

For the calculation of the temperature profile inside the heat exchanger the contribution of the latent heat release due to condensation of aerosol forming elements is neglected. Consequently the heat balance written over the cold and hot medium for a small section of the heat exchanger passage  $dz$ , can be described as:

$$dQ = \dot{m}_g c_{p,g} dT_g = \dot{m}_c c_{p,c} dT_c \quad (6.1)$$

where  $Q$  denotes the heat flow,  $\dot{m}$  the mass flow,  $c_p$  the heat capacity of the medium and  $T$  the temperature of the medium. The subscripts  $g$  and  $c$  denote the hot (flue gas) and the cold medium (cooling water) respectively. The heat transferred between the two media over the surface can be written as:

$$dQ = HU (T_g - T_c) dz \quad (6.2)$$

where  $H$  is the height of the flue gas passage and  $U$  is the overall heat transfer coefficient. In a water cooled heat exchanger the mass capacity flow ( $\dot{m}c_p$ ) of the cooling water is much larger than the mass capacity flow of the flue gas. Consequently, temperature variations of the cooling water are much smaller compared to the temperature variations of the flue gas,  $dT_c \ll dT_g$ , so combining Eq. 6.1 and 6.2 for the hot flue gas gives:

$$\frac{dT_g}{dz} = \frac{HU}{\dot{m}_g c_{p,g}} (T_g - T_c) \quad (6.3)$$

The flue gas mass flow  $\dot{m}_g$  through a heat exchanger passage remains constant, whereas the heat capacity of the flue gas  $c_{p,g}$  only slightly depends on temperature. Considering that the heat capacity of the flue gas only varies between approximately 1000 and 1200  $\frac{J}{kgK}$ , while varying the flue gas temperature from 273 to 1373 K [36], yields that a mean heat capacity of 1100  $\frac{J}{kgK}$  can be used for the calculations. The overall heat transfer coefficient comprises contributions of:

- the convective heat resistance between the cooling water and the metal channel,
- the conductive heat resistance of the metal channel,
- the heat resistance of the thermal insulation, a porous construction subjected to the following heat transfer mechanisms:
  - conduction of the material fibers,
  - conduction of the enclosed gas,
  - radiation in the pores of the fiber board,
- the conductive heat resistance of the metal plate,
- the convective heat resistance between the flue gas and the plate.

The convective heat resistance between the fluid and the channels and the heat resistance over the metal surfaces itself are negligible in the overall heat transfer coefficient compared to the heat resistance of the thermal insulation and the convective heat resistance between the flue gas and the plate. So the heat transfer coefficient  $U$ , expressed in Eq. 6.3 can be defined as:

$$U = \frac{1}{\frac{1}{h} + \frac{t_{iso}}{k_{iso}}} \quad (6.4)$$

where  $h$  is the heat transfer coefficient of the hot gas,  $t_{iso}$  is the thickness of the insulation material and  $k_{iso}$  denotes the thermal conductivity of the insulation material. According to Janna [27], the Nusselt number for a fully developed laminar flow between two parallel plates under the assumption of a constant wall temperature is approximately 7.51.

$$\text{Nu} = \frac{D_h h}{k_{cond}} \quad (6.5)$$

The hydraulic diameter  $D_h$  in Eq. 6.5 is equivalent to two times the plate distance  $t$  so the heat transfer coefficient  $h$  is only a function of the temperature through the conductivity of the gas  $k_{cond}$  [27]. According to Bird [6], the thermal conductivity of a monatomic gas can be expressed as:

$$k_{cond} = \frac{\sqrt{(mk_b T/\pi)}}{\pi d_m^2} \quad (\text{monatomic gas}) \quad (6.6)$$

Equation 6.6 is the thermal conductivity of a dilute gas composed of rigid spheres with diameter  $d_m$ . In Eq. 6.6,  $k_b$  is Boltzmann's constant and  $m$  is the mass of one molecule. Equation 6.6 predicts that the thermal conductivity of a monatomic gas can be fitted as a square root function of temperature  $T$ . However, in order to obtain an analytical solution for the temperature distribution inside one heat exchanger passage, the square root dependency of the temperature on the thermal conductivity of the flue gas is represented by a linear relation in the operating range, defined as:

$$k_{cond} = aT_g \quad (6.7)$$

In Eq. 6.7,  $a$  is determined using a linear fit for the heat conductivity of air ( $a = 7.0 \cdot 10^{-5} \frac{W}{mK^2}$ ). A quite good agreement between the linear fit and literature data in the relevant temperature range can be observed as depicted in Fig. 6.4.

Also the heat resistance of the thermal insulation is a function of the temperature. For an insulation material with a high porosity the heat conductivity of the material itself can be neglected compared to the conductivity of the enclosed gas. For the radiative heat transfer the porous structure can be treated as an optically thick medium, the photons travel only a limited distance before being absorbed again. The *Rosseland approximation* [37] [45] is used, introducing a term in the effective heat conduction coefficient with a third power dependency on the temperature:

$$k_{eff} = k_{cond} + k_{rad} = aT + bT^3 \quad (6.8)$$

where the subscripts *cond* and *rad* indicate the conductive and radiative contribution in the effective heat conductivity respectively. The constant  $b$  in Eq. 6.8 is determined using the data sheet provided by the insulation supplier ( $b = 6.0 \cdot 10^{-11} \frac{W}{mK^4}$ ), whereas constant  $a$  is equal to the constant for the thermal conductivity of air, denoted in Eq. 6.7, see Fig. 6.4.

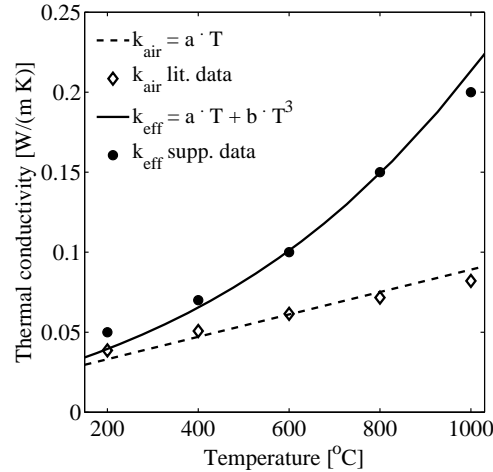


**Figure 6.4.** Dashed line: Linearised thermal conductivity of air compared with literature data  $\diamond$  [VDI. *Wärmeatlas*, 6th ed.; VDI-Verlag GmbH, Düsseldorf, 1991]. Continuous line: Applying *Rosseland approximation* for the thermal conductivity of insulation material compared with literature data  $\bullet$  [Data obtained by supplier].

For large temperature differences between the cooling water and the flue gas, it is necessary to evaluate Eq. 6.8 at an average temperature. This is achieved by integrating Eq. 6.8 over the temperature difference over the insulation material and dividing the whole integral by the temperature difference itself:

$$k_{iso} = \frac{1}{(T_g - T_c)} \int_{T_c}^{T_g} k_{eff}(T) dT = (T_g + T_c) \left( \frac{1}{2}a + \frac{1}{4}b(T_g^2 + T_c^2) \right) \quad (6.9)$$

For the analytical solution, a small error is introduced evaluating the thermal conductivity of the insulation material over the cooling water temperature  $T_c$  and the gas temperature  $T_g$ . The thermal conductivity should be evaluated on the wall temperatures on both sides of the insulation material. The assumption that the wall temperature equals the water temperature on the cooling water side is reasonable due to the heat transfer coefficient on the waterside. However, the wall temperature on the gas side is slightly lower than the gas temperature. In contrast to the analytical model, this effect is implemented in the numerical approach.

In order to provide an analytical solution the overall heat transfer coefficient  $U$  can be expressed as:

$$U = \frac{1}{\frac{2t}{\text{Nu}} \frac{1}{aT_g} + \frac{t_{iso}}{(T_g+T_c)\left(\frac{1}{2}a + \frac{1}{4}b(T_g^2+T_c^2)\right)}} \quad (6.10)$$

Substituting Eq. 6.10 into Eq. 6.3 results in an expression for the temperature gradient of the gas:

$$\frac{dT_g}{dz} = \frac{2H(T_g - T_c)}{\dot{m}_g c_{p,g} \left( \frac{2t}{\text{Nu}} \frac{1}{aT_g} + \frac{t_{iso}}{(T_g+T_c)\left(\frac{1}{2}a + \frac{1}{4}b(T_g^2+T_c^2)\right)} \right)} \quad (6.11)$$

where the subscripts  $h$  and  $c$  denote the hot and the cold medium respectively. It is noticed that Eq. 6.11 is an irreducible equation. By assuming a constant cooling water temperature  $T_c$  and constant physical properties the inverse solution  $z(T_g)$  can be found analytically by separation of variables:

$$\begin{aligned} z(T_g) = & \frac{1}{2} \frac{\dot{m}_g c_{p,g} t_{iso} \ln \frac{T_g+T_c}{T_{g,0}+T_c}}{H(a+bT_c^2)T_c} - \frac{\dot{m}_g c_{p,g} t \ln \frac{T_g-T_c}{T_{g,0}-T_c}}{H\text{Nu}(a+bT_c^2)T_c} - \frac{\dot{m}_g c_{p,g} T_c t \ln \frac{T_g-T_c}{T_{g,0}-T_c} b}{Ha\text{Nu}(a+bT_c^2)} - \\ & \frac{1}{2} \frac{\dot{m}_g c_{p,g} t_{iso} \ln \frac{T_g-T_c}{T_{g,0}-T_c}}{H(a+bT_c^2)T_c} + \frac{\dot{m}_g c_{p,g} t \ln \frac{T_g}{T_{g,0}}}{Ha\text{Nu}T_c} + \\ & \frac{\dot{m}_g c_{p,g} t_{iso} b \arctan \left( \frac{b(T_g-T_{g,0})(2a+bT_c^2)}{\sqrt{(2a+bT_c^2)b(2a+bT_c^2+bT_g T_{g,0})}} \right)}{H(a+bT_c^2)\sqrt{(2a+bT_c^2)b}} \end{aligned} \quad (6.12)$$

In Eq. 6.12,  $T_{g,0}$  represents the initial flue gas temperature at the inlet of the heat exchanger. For the calculations an initial flue gas temperature at the inlet of the heat exchanger of 1047 °C is assumed, that is equal to the average flue gas temperature in the secondary combustion zone during the experiments as described in Sec. 6.1.3. Contrary to the experiments performed with the water cooled heat exchangers as described in Sec. 5.3, no sophisticated cooling water regulation system was available for the experiments with the insulated plate type heat exchanger. As a result of this, ordinary tap water with a typical temperature of 12 °C was used as cooling medium, which is freely exhausted in a sink. Consequently, the cooling water temperature required for the calculation is subjected to this temperature. In order to achieve a capacity of approximately 7.5 kW<sub>th</sub>, the flue gas mass flow  $m_g$  through one heat exchanger passage during the calculations was  $5.2 \cdot 10^{-4} \frac{\text{kg}}{\text{s}}$ , whereas the heat capacity of the flue gas  $c_{p,g}$  for the analytical solution is kept constant at  $1100 \frac{\text{J}}{\text{kgK}}$ .

A graphical representation of the temperature profile in a heat exchanger passage calculated according to Eq. 6.12 using the previously described physical quantities is depicted in Fig. 6.5. Besides analytically, Eq. 6.11 is also solved numerically in compliance with a lower wall temperature regarding the calculation for the thermal conductivity of the insulation material. In Fig. 6.5 it can be observed that the numerical and analytical model are in good agreement. The temperature difference between the analytical and numerical model is less than 6 %.

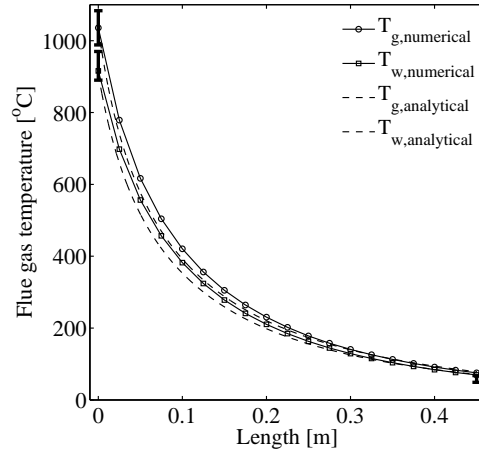


**Figure 6.5.** Numerically and analytically determined flue gas temperature  $T_g$  and wall temperature  $T_w$  profile in the heat exchanger.

**Explanation:** The error bars at the inlet represents respectively the flue gas temperatures in the secondary combustion zone and the wall temperature near the heat exchanger inlet. The error bar at heat exchanger outlet represents the wall temperature at that position.

Based on the resulting flue gas outlet temperature, a maximum Reynolds number of 200 is calculated, so it is proven that the flow is laminar through the whole heat exchanger section. The wall temperature  $T_w$  is given by:

$$T_w = T_g - (T_g - T_c) \frac{U}{h} \quad (6.13)$$

where the overall heat transfer coefficient  $U$  is determined according to Eq. 6.10 and the convective heat transfer coefficient is calculated by use of Eq. 6.5. An iterative method is used in order to determine the wall temperature profile for the numerical approach. The wall temperatures for both methods are depicted in Fig. 6.5.

### 6.1.3 Results from test runs with HE5

From the experiments with the water cooled heat exchanger and the gas to gas heat exchanger it is proven that significant aerosol emission reductions can be achieved when the heat exchanger passage is in the millimetre regime. For comparison of the different heat exchanger designs comparable initial conditions were required.

In extreme cases,  $T_{sec}$  varies between 1000 and 800 °C. Therefore, experiments with the insulated plate type heat exchanger were conducted at flue gas temperatures in the secondary combustion zone of approximately 1000 and 800 °C. For each flue gas temperature three BLPI measurements were performed for determining the overall aerosol emission reduction. Additionally, HT – LPI measurements were performed directly in the secondary combustion zone. Using this measurement device it



is possible to quantify the concentration of aerosols formed in the secondary combustion zone before the flue gas enters the aerosol condenser. It is noticed that due to practical reasons the HT – LPI measurements inside the furnace were not performed simultaneously with the BLPI measurements downstream the boiler and the heat exchanger.

In order to verify the model describing the temperature profile inside the insulated plate type heat exchanger, firstly temperature measurements were performed.  $T_{sec}$  was measured with a thermocouple that was also used for the furnace control system, having a diameter of approximately 20 mm. Measuring the flue gas inlet and outlet temperature was not that straightforward. Due to the chlorine in the flue gas in combination with high temperatures, the thermocouples oxidised very quickly. As a result of this, the lifetime of the thermocouples was limited. This especially holds for the thermocouple near the heat exchanger inlet. Small vibrations of the thermocouple at temperatures around 1000 °C already resulted in irreparable damage. Unfortunately, applying ceramic thermocouple protection tubes that is commonly used was not an option due to geometrical restrictions. As an alternative approach the wall temperature near the inlet as well as near the outlet of aerosol condenser was measured instead of the flue gas temperature. The benefit of measuring the wall temperature is that the thermocouple itself is not directly in contact with the hot flue gas, such that the thermocouples remains intact during the experiments. For determining the wall temperatures type K thermocouples with a diameter of 1 mm were used.

## Fuel and predicted aerosol composition

Again, chemically untreated wood chips were chosen as fuel during the experiments with the insulated plate type heat exchanger. The moisture content as well as the ash content and the concentrations of the most relevant ash and aerosol forming elements of the fuel applied are depicted in Tab. 6.1.

Comparing the fuel composition as shown in Tab. 6.1 with the one of the fuel used for test runs with HE1 and HE2 (see Tab. 5.2), it can be observed that the moisture content of this fuel is almost 5 wt.%(w.b.) lower. Furthermore, it can be observed that the concentration of main ash forming species in the above described fuel, like Ca and Si, are significantly lower than the fuel used for test runs with HE1 and HE2, resulting in a lower ash content of 0.7 wt.%(d.b.).

Regarding the aerosol forming elements in the fuel it can be observed that the Cl concentration was very low. While the Cl concentration amounted to 100 and 80 mg/kg (d.b.) during test runs with respectively HE1 and HE2, the Cl concentration during experiments with HE5 amounted to 28 mg/kg (d.b.), a difference of approximately a factor of 3 to 4. Regarding the K concentration it can be observed that this value is much lower, and amounts to 619 mg/kg (d.b.). Compared to the K and S concentrations in the fuel during test runs with HE1 and HE2, these value are approximately 20 % lower. Because K is one of the main aerosol forming elements, the potential for aerosol formation also becomes less for the fuel presented in Tab. 6.1 compared to previous estimations (HE1 and HE2). Furthermore, the heavy metal concentrations were in general relatively low.

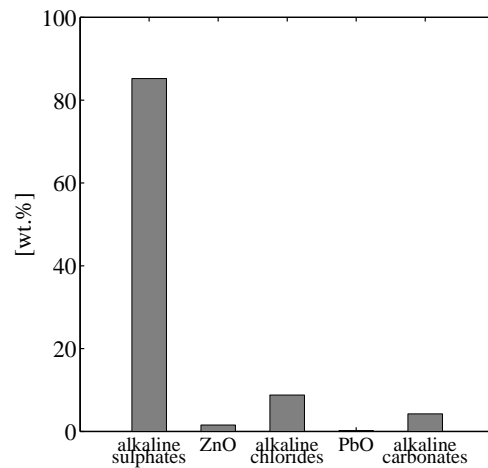
**Table 6.1.** Composition of chemically untreated wood chips used for the experiments with the insulated plate type heat exchanger (HE5).

Explanations: d.b. ... dry base; w.b. ... wet base; STD ... standard deviation.

		HE5
parameter	unit	average value & STD <sup>a</sup>
Moisture content	wt. % (w.b.)	22.6 ± 0.6
Ash content	wt. % (d.b.)	0.7 ± 0.1
S	mg/kg (d.b.)	110 ± 1
Cl	mg/kg (d.b.)	28 ± 8
Ca	mg/kg (d.b.)	2003 ± 140
Si	mg/kg (d.b.)	229 ± 42
Mg	mg/kg (d.b.)	230 ± 21
K	mg/kg (d.b.)	619 ± 31
Na	mg/kg (d.b.)	15 ± 3
Zn	mg/kg (d.b.)	9 ± 1
Pb	mg/kg (d.b.)	< 5 <sup>b</sup>

<sup>a</sup> based on 3 fuel analyses

<sup>b</sup> below detection limit

**Figure 6.6.** Aerosol composition calculated from the fuel composition during test runs with HE5 ( $D_h \approx 6$  mm).

Based on the fuel composition as depicted in Tab. 6.1, an estimation is made regarding the maximum concentration of aerosol forming compounds released to the flue gas. For these calculations it was assumed that the fuel is combusted at temperatures

around 1000 °C.

Based on the fuel analyses and release factors as described in Sec. 3.2, the concentration of aerosol forming compounds in the flue gas is estimated to 48 mg/Nm<sup>3</sup> (dry flue gas and 13 vol.% O<sub>2</sub>). Compared to previous experiments with the fuel used for HE1 (75 mg/Nm<sup>3</sup>) and HE2 (58 mg/Nm<sup>3</sup>), then this value is slightly lower, mainly caused by the lower K concentration in the fuel. When all aerosol forming compounds are transformed into aerosols, then the corresponding aerosol composition calculated from the fuel composition is shown in Fig. 6.6. In this figure it can be seen that the aerosols are expected to consist mainly of alkaline sulphate (85 wt. %).

Furthermore, also some small share of ZnO particles are formed (2 wt. %). Because the concentration Pb in the fuel was below the detection limit, the contribution of PbO in the aerosols is debatable.

### Process control parameters

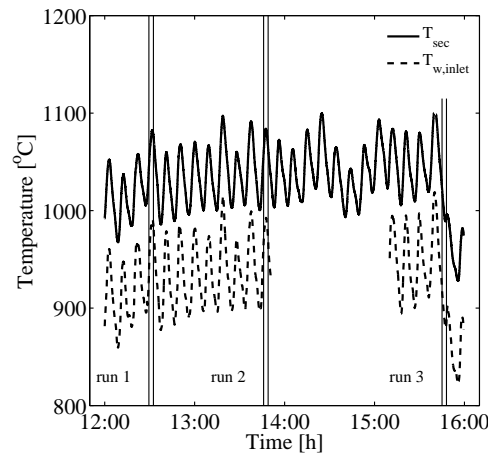


**Figure 6.7.** Temperature in the secondary combustion zone and the wall temperature near the inlet of the heat exchanger test runs for combustion temperatures > 1000 °C. The vertical lines indicate the measurement periods.

In Fig. 6.7 and 6.8, cyclic temperature variations in the secondary combustion zone with a typical cycle time of 9 minutes can be observed. These variations are mainly caused by the movement of the grate. By analysing the process data, it has been found out that the backward movement of the grate resulted in a short periods with increased combustion rates. Consequently, also the furnace temperatures increases in these periods.

A major disadvantage of measuring the temperature in a dynamic environment with two different thermocouple sizes is that the time response of the different thermocouples exhibits different time constants  $\tau$ . Because of this, a phase change or time delay of approximately 1 minute occurs between the different thermocouple dimen-

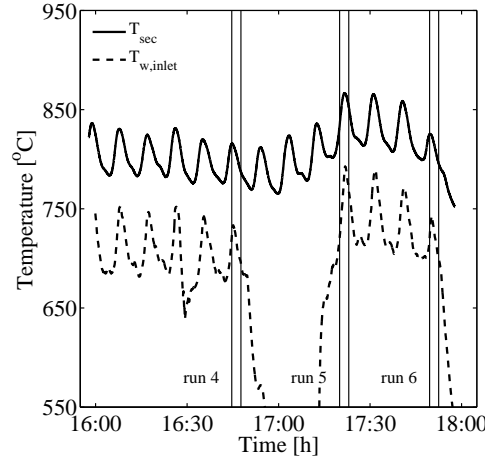


**Figure 6.8.** Temperature in the secondary combustion zone and the wall temperature near the inlet of the heat exchanger during test runs for combustion temperatures of about 800 °C. The vertical lines indicate the measurement periods.

sions that could also be observed from the measurement data. In order to determine the phase change for matching the temperatures, the time constants of each thermocouple have to be known. A conservative estimation of the time constant  $\tau_{tc}$  of a thermocouple without radiation effects is given by:

$$\tau_{tc} = \frac{\rho_{tc} D_{tc} c_{p,tc}}{6h_{tc}} \quad (6.14)$$

where  $c_p$  and  $\rho$  are respectively the heat capacity and the density, whereas the subscript  $tc$  refers to the thermocouple. The diameter of the thermocouple is denoted by  $D_{tc}$ . A Nusselt relation is used to determine the heat transfer coefficient  $h_{tc}$ . From equation 6.14 it can be observed that the time response of a thermocouple is proportional to its diameter  $D_{tc}$ . The time constant of a 1 mm thermocouple is in the order of a couple of seconds, whereas the time constant for the thicker thermocouple in the furnace (12 mm) is in the order of one minute. These typical time constants are used to compensate the time delay between both thermocouples.

A good agreement between the measured wall temperatures and the calculated wall temperatures as shown in Fig. 6.5 is observed. This observation indicates that the model derived using *Rosseland's approximation* is sufficient to describe the temperature profile inside the insulated plate type heat exchanger as shown in Fig. 6.2 and 6.3. The calculations as shown in Fig. 6.5 are subjected to an initial flue gas inlet temperature equalling the measured average flue gas temperature in the secondary combustion zone of  $1033 \pm 32$  °C during a four hour operation. However, during the impactor measurements the average flue gas temperature in the secondary combustion zone was about 1050 °C (see Tab. 6.2). The furnace temperature in the secondary

**Table 6.2.** Overview of process conditions during experiments at flue gas temperatures in the secondary combustion zone of about 1050 °C.

Explanations:  $T_{sec}$  ... flue gas temperature in secondary combustion zone;  $T_{w,in}$  ... wall temperature at heat exchanger inlet;  $T_{boiler,out}$  ... flue gas temperature at boiler outlet;  $T_{w,out}$  ... wall temperature at heat exchanger outlet.

run	$T_{sec}$ [°C]	$T_{w,in}$ [°C]	$T_{boiler,out}$ [°C]	$T_{w,out}$ [°C]
1	1064 ± 16	976 ± 16	192 ± 4	62 ± 1
2	1073 ± 12	983 ± 7	199 ± 1	63 ± 1
3	1006 ± 14	894 ± 13	196 ± 3	76 ± 1

**Table 6.3.** Overview of process conditions during experiments at flue gas temperatures in the secondary combustion zone of about 800 °C.

Explanations:  $T_{sec}$  ... flue gas temperature in secondary combustion zone;  $T_{w,in}$  ... wall temperature at heat exchanger inlet;  $T_{boiler,out}$  ... flue gas temperature at boiler outlet;  $T_{w,out}$  ... wall temperature at heat exchanger outlet.

run	$T_{sec}$ [°C]	$T_{w,in}$ [°C]	$T_{boiler,out}$ [°C]	$T_{w,out}$ [°C]
4	792 ± 9	673 ± 17	172 ± 5	96 ± 3
5	808 ± 7	740 ± 32	182 ± 5	47 ± 2
6	814 ± 10	724 ± 13	181 ± 5	90 ± 1

combustion zone during experiments at lower temperatures was about 800 °C (see Tab. 6.3).

In Tab. 6.2 and 6.3 it can be observed that the wall temperatures near the heat exchanger outlet  $T_{w,out}$  during test runs at a the furnace temperature of about 1050 °C were lower than during test runs at  $T_{sec} \approx 800$  °C. This deviation is caused by the fact that the mass flow through HE5 during test runs at  $\approx 800$  °C was lower. Using the same mass flow as used during test runs at about 1050 °C would have resulted in flue gas temperatures at the heat exchanger outlet below the dew point of the water vapour in the flue gas resulting in inaccurate BLPI measurements. However, as already mentioned in Sec. 3.8.1, it is expected that the influence of the mass flow, does not influence the condensation process.

Furthermore, it can be observed that the wall temperature at the heat exchanger outlet  $T_{w,out}$  during run 5 was significantly lower than the wall temperatures at heat exchanger outlet for run 4 and 6, see Fig. 6.8. The reason for this deviation is the fact that the flue gas fan downstream the heat exchanger was switched off immediately after run 4, such that the heat exchanger could be inspected visually. Contrary to the flue gas fan, the cooling water flow through the aerosol condenser was not switched off. As a result of this the whole heat exchanger cooled down. After inspection of the heat exchanger the flue gas fan was switched on again. However, due to the mass

capacity of the heat exchanger, it took some time to heat up the heat exchanger. As the time to reach stable conditions downstream the heat exchanger was not fully achieved for run 5, the resulting flue gas temperature at the heat exchanger outlet temperature for that particular measurement was lower (see Tab. 6.3).

## Impactor measurements

The aerosol concentrations downstream the boiler and the heat exchanger were determined with BLPI measurements, whereas the aerosol concentration sampled inside the furnace were determined by use of the HT – LPI measurements.

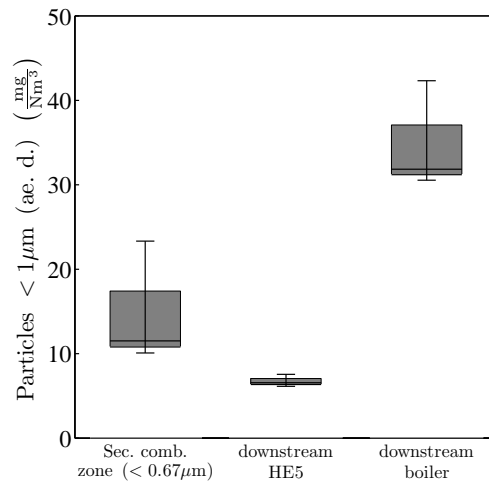


**Figure 6.9.** Concentration of aerosols in the flue gas sampled directly in the furnace, at boiler outlet and downstream HE5 ( $D_h \approx 6 \text{ mm}$ ) for test runs performed at flue gas temperatures in the secondary combustion zone of approximately  $1050 \text{ }^\circ\text{C}$ . Note that BLPI and HT – LPI measurements are not performed simultaneously.

Explanations: All concentrations related to dry flue gas and  $13 \text{ vol.}\% \text{ O}_2$ ; ae. d. ... aerodynamic particle diameter; number of BLPI measurements: boiler outlet 3, at heat exchanger outlet 3; number of HT – LPI measurements in secondary combustion zone 3; the boxes indicate the quartiles 25 % to 75 %, the line in the box displays the median value; the error indicator represents the maximum and minimum values.

In Fig. 6.9 and 6.10 the particle fractions  $< 1 \mu\text{m}$  determined downstream the boiler and HE5 as well as inside the secondary combustion zone are shown as box plots. The upper and lower limit of the boxes represent the 1<sup>st</sup> and 3<sup>rd</sup> quartile of the measurement results, while the line in the boxes indicates the median value. The error indicators represent the minimum and maximum aerosol concentration. It has to be noticed that the HT – LPI measurements in secondary combustion zone were not performed simultaneously with the BLPI measurements downstream HE5 and the boiler.

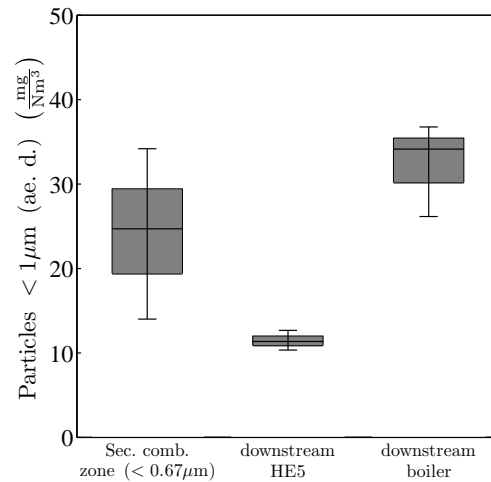


**Figure 6.10.** Concentration of aerosols in the flue gas sampled directly in the furnace, at boiler outlet and downstream HE5 ( $D_h \approx 6\text{ mm}$ ) for test runs performed at flue gas temperatures in the secondary combustion zone of approximately  $800\text{ }^\circ\text{C}$ . Note that BLPI and HT – LPI measurements are not performed simultaneously.

Explanations: All concentrations related to dry flue gas and  $13\text{ vol.}\% O_2$ ; ae. d. ... aerodynamic particle diameter; number of BLPI measurements: boiler outlet 3, at heat exchanger outlet 3; number of HT – LPI measurements in secondary combustion zone 3; the boxes indicate the quartiles 25 % to 75 %, the line in the box displays the median value; the error indicator represents the maximum and minimum values.

Despite the different temperature in the secondary combustion zone, the concentration of aerosols measured downstream the boiler at  $T_{sec} \approx 1050\text{ }^\circ\text{C}$  ( $34.9\text{ mg}/Nm^3$ ) and  $800\text{ }^\circ\text{C}$  ( $32.3\text{ mg}/Nm^3$ ) were approximately equal. Based on a the fuel analyses as described in Sec. 6.1.3, a maximum aerosol concentration of  $48\text{ mg}/Nm^3$  was expected. The release factors used for these calculations were all related to a combustion temperature of  $\approx 1000\text{ }^\circ\text{C}$ . Comparing the estimated aerosol concentration ( $48\text{ mg}/Nm^3$ ) with the measured aerosol concentration at  $T_{sec} \approx 1050\text{ }^\circ\text{C}$  downstream the boiler ( $34.9\text{ mg}/Nm^3$ ), then it can be observed that, based on the estimated concentration, approximately 27 % less aerosol mass was detected downstream the boiler. This observation is in agreement with expectations from previous measurements as described in Sec. 5.3.4, where a difference of 30 % is mentioned.

The aerosol concentration at  $T_{sec} \approx 1050\text{ }^\circ\text{C}$  amounts to  $15.0\text{ mg}/Nm^3$ , whereas the concentration of aerosols at the same position for  $T_{sec} \approx 800\text{ }^\circ\text{C}$  was higher ( $24.3\text{ mg}/Nm^3$ ). It is noticed that the measurements with the HT – LPI were not performed simultaneously with the BLPI. However, still a clear trend can be observed that more aerosols are formed in the secondary combustion zone for lower flue gas temperatures in that zone. The reason for this is that, due to the lower temperature, aerosol forming compounds become supersaturated in the secondary combustion zone.

As a result of this, aerosol forming compounds are able to nucleate and/or condense on already existing particles in that zone, resulting in a higher concentration of aerosols.

The heat exchanger is designed to optimise condensation of aerosol forming vapours on heat exchanger surfaces, rather than deposition of already formed aerosols. Consequently, for increasing fine particulate matter formation inside the furnace also higher fine particulate matter emissions can be expected downstream HE5. On average, the aerosol concentration downstream HE5 during test runs at furnace temperatures around  $1050\text{ }^{\circ}\text{C}$  amounts to  $6.7\text{ mg}/\text{Nm}^3$ , whereas for a temperature around  $800\text{ }^{\circ}\text{C}$  this concentration amounts to  $11.5\text{ mg}/\text{Nm}^3$ .

In Fig. 6.11 and 6.12, the PSD's of the aerosols downstream the boiler and the heat exchanger as well as the PSD's of the aerosols sampled directly in the secondary combustion zone at temperatures around  $1050$  and  $800\text{ }^{\circ}\text{C}$  are given.

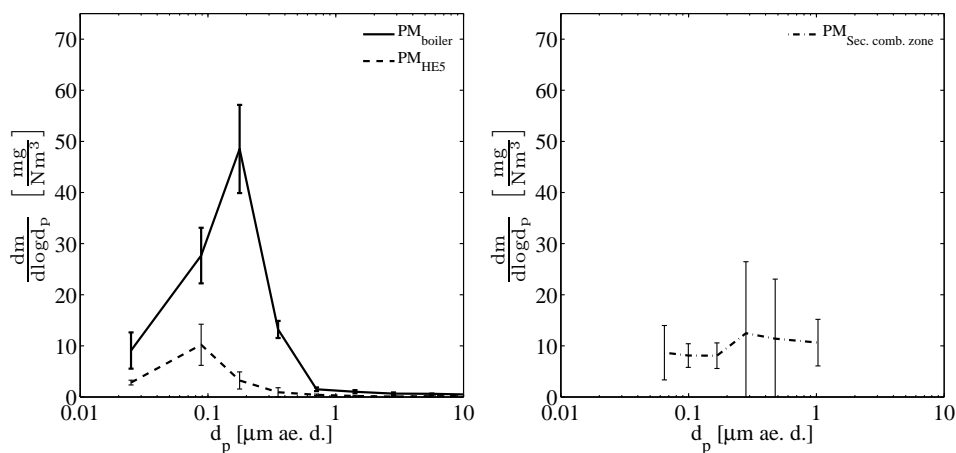


**Figure 6.11. On the left:** Average PSD of the particles downstream the ordinary boiler and HE5, determined by BLPI measurements for combustion temperatures of about  $1050\text{ }^{\circ}\text{C}$ . **On the right:** Average PSD of the particles inside the furnace, determined by HT – LPI measurements for combustion temperatures of about  $1050\text{ }^{\circ}\text{C}$ .

Explanations: All concentrations are expressed in  $\text{mg}/\text{Nm}^3$  and related to dry flue gas and  $13\text{ vol.}\% \text{ O}_2$ ; number of BLPI measurements: 3; number of HT – LPI measurements: 3; subscript *boiler* ... boiler outlet; subscript *HE5* ... aerosol condensing heat exchanger outlet; subscript *Sec. comb. zone* ... secondary combustion zone; ae. d. ... aerodynamic particle diameter.

Impactor measurements performed at  $T_{\text{sec}} \approx 1050\text{ }^{\circ}\text{C}$  show a clear peak of the average PSD of the aerosols downstream the ordinary boiler around a particle size between  $0.125\text{ }\mu\text{m}$  and  $0.25\text{ }\mu\text{m}$ , see Fig. 6.11. Comparing the average PSD of the aerosols sampled downstream the boiler during experiments with HE5 with previous PSD's of aerosols sampled at comparable conditions downstream the boiler (see Fig. 5.7, 5.8, 5.9 and 5.17), it can be observed that the shape of the PSD is comparable. In Fig. 6.12 it can be observed that the average PSD of the aerosols downstream



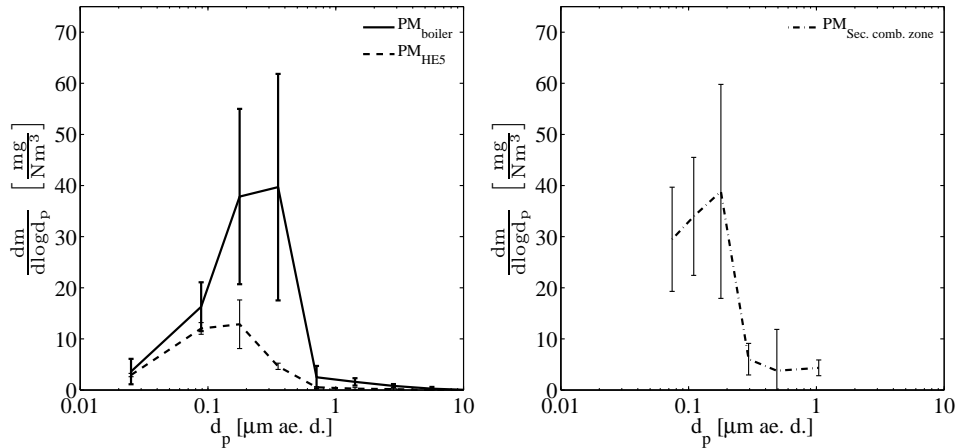


**Figure 6.12.** **On the left:** Average PSD of the particles downstream the ordinary boiler and the insulated heat exchanger, HE5, determined by BLPI measurements for combustion temperatures of about  $800\text{ }^{\circ}\text{C}$ . **On the right:** Average PSD of the particles inside the furnace, determined by HT – LPI measurements for combustion temperatures of about  $800\text{ }^{\circ}\text{C}$ . Explanations: All concentrations are expressed in in  $\text{mg}/\text{Nm}^3$  and related to dry flue gas and  $13\text{ vol.}\% \text{O}_2$ ; number of BLPI measurements: 3; number of HT – LPI measurements: 3; subscript *boiler* ... boiler outlet; subscript *HE5* ... aerosol condensing heat exchanger outlet; subscript *Sec. comb. zone* ... secondary combustion zone; ae. d. ... aerodynamic particle diameter.

the boiler during experiments with HE5 at  $T_{sec} \approx 800\text{ }^{\circ}\text{C}$  is around a particle size between  $0.125\text{ }\mu\text{m}$  and  $0.5\text{ }\mu\text{m}$ . This is caused by the fact that individual PSD's of the aerosols downstream the boiler showed twice a clear peak at a cut size of  $0.5\text{ }\mu\text{m}$  and one experiment showed a clear peak of the PSD of the aerosols at a cut size of  $0.25\text{ }\mu\text{m}$ . Consequently, the error bars of the average PSD of the aerosols downstream the boiler at  $T_{sec} \approx 800\text{ }^{\circ}\text{C}$  using HE5 are relatively large.

The concentrations of particles downstream HE5 at  $T_{sec} \approx 1050\text{ }^{\circ}\text{C}$  and  $T_{sec} \approx 800\text{ }^{\circ}\text{C}$  are over the whole size range lower than the concentration of particles sampled downstream the boiler. During test runs at  $T_{sec} \approx 1050\text{ }^{\circ}\text{C}$ , it can also be observed that the peak of the average PSD of the aerosols downstream HE5 is shifted to a smaller particle size (i.e. from a cut diameter of  $0.25\text{ }\mu\text{m}$  to a cut diameter of  $0.125\text{ }\mu\text{m}$ ) compared to the peak of the PSD of the aerosols sampled downstream the boiler, which was at between particle sizes of  $0.125\text{ }\mu\text{m}$  and  $0.25\text{ }\mu\text{m}$ . This observation indicates that a part of already existing aerosols and aerosol forming compounds are precipitated in the aerosol condenser. Subsequently, aerosol growth due to coagulation and condensation in the aerosol condenser is suppressed, resulting is smaller particles compared to the situation downstream the boiler.

The following remark can be made regarding the PSD of the aerosols downstream HE5 at  $T_{sec} \approx 800\text{ }^{\circ}\text{C}$ . One measurement showed a peak of the PSD of the aerosols in the particle size range between  $0.125\text{ }\mu\text{m}$  and  $0.25\text{ }\mu\text{m}$ . However, the concentration

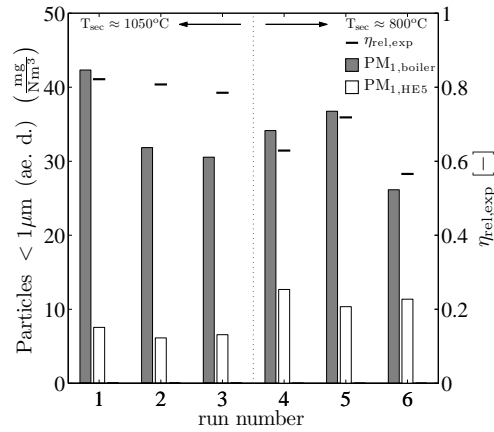


**Figure 6.13.** Overview of the aerosol emission reductions compared to ordinary boiler design for two different flue gas temperatures in the secondary combustion zone using an insulated plate type heat exchanger (HE5).

**Explanation:** All concentrations related to dry flue gas and 13 vol.%  $O_2$ ; ae. d. ... aerodynamic particle diameter;  $\eta_{rel,exp}$  ... particulate emission reduction compared to ordinary boiler design, calculated according to Eq. 5.1; subscript *boiler* ... boiler outlet; subscript *HE* ... aerosol condensing heat exchanger outlet.

of particles was very low for that particular measurement. Accidentally, the other two measurements showed a peak in the PSD of particles that was between  $0.25 \mu m$  and  $0.5 \mu m$ , whereas the concentration of particles in the particle size range between  $0.125 \mu m$  and  $0.25 \mu m$  were almost equal to that of maximum concentration in the previous described measurement. As a result of this, the standard deviation at a particle size class between  $0.125 \mu m$  and  $0.25 \mu m$  is rather low.

The average PSD of the aerosols sampled in the secondary combustion zone using the HT – LPI at flue gas temperatures around  $1050^\circ C$  as depicted in Fig. 6.11 do not show a clear peak. This does not only hold for the average PSD of the particles formed, but also for the individual HT – LPI measurements. The mutual differences of the individual HT – LPI measurements performed at  $T_{sec} \approx 800^\circ C$  also show quite large deviations. However, on average, the peak of the PSD of the aerosols formed inside the furnace at  $T_{sec} \approx 800^\circ C$  was between a particle size of  $0.125 \mu m$  and  $0.25 \mu m$ . As the HT – LPI measurements were not performed simultaneously with the BLPI measurements, it is hard draw conclusions about this observation. However, as described in Sec. 4.4, thermophoresis is the most relevant particle deposition mechanism for aerosols in the size range between  $0.1$  and  $1.0 \mu m$ , resulting in lower particulate matter emissions downstream the aerosol condenser. As already mentioned in Sec. 4.5, thermophoresis in such heat exchanger results in an additional particulate emission reduction of approximately 25 %.

In Fig. 6.13 the particle fractions  $< 1 \mu m$  downstream the boiler and HE5 are depicted for the individual BLPI measurements at  $T_{sec} \approx 1050^\circ C$  and  $\approx 800^\circ C$ . The

corresponding fine particulate emission reduction based for the coupled set of BLPI measurements are calculated according to Eq. 5.1.

Quite constant aerosol emission reductions could be achieved of about  $80 \pm 2 \%$  when applying temperatures in the secondary combustion zone around  $\approx 1050^\circ\text{C}$ . A lower flue gas temperature in the secondary combustion zone does not result in a significant difference in the aerosol emissions at boiler outlet (see Fig. 6.9 and 6.10). However, the aerosol emissions at heat exchanger outlet are significantly higher. Consequently, the aerosol emission reductions using  $T_{sec} \approx 800^\circ\text{C}$  are lower. On average an aerosol emission reduction of  $64 \pm 7 \%$  could be achieved.

## 6.2 Comparison of experimental results of HE5 with simulations

To verify whether the 2D model expressed in Cartesian coordinates as described in chapter 4 and in Appendix A is correct, a comparison is made between measured aerosol emission reductions at  $T_{sec} \approx 1050^\circ\text{C}$  and simulated aerosol emission reductions. During the simulations, condensation and nucleation of  $\text{K}_2\text{SO}_4$  only is considered as well as deposition of already formed particles. The inlet conditions were approximately equal compared to the conditions during the experiments.

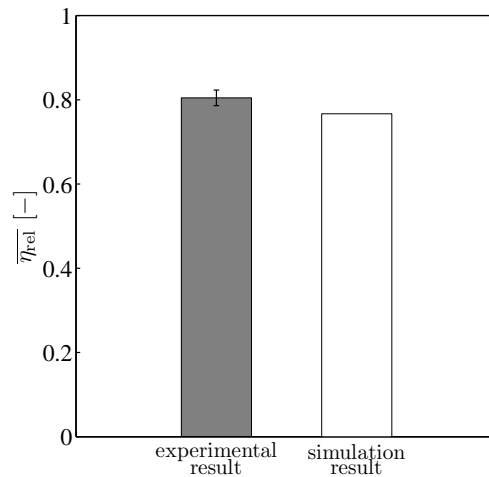


**Figure 6.14.** Comparison between experimental obtained average aerosol emission reductions and the aerosol emission reduction obtained by simulations according to the 2D model as described in chapter 4 at inlet temperatures around  $1050^\circ\text{C}$ .

Explanation: Experimental results are related to dry flue gas and 13 vol.%  $\text{O}_2$ ;  $\bar{\eta}_{rel}$  ... average particulate emission reduction compared to ordinary boiler design, calculated according to Eq. 5.1.

In Fig. 6.14 it can be observed that there is a good agreement between experimental

results and the simulation result. Experiments showed aerosol emission reductions of about  $80 \pm 2$  %, whereas the simulation predicts an aerosol emission reduction of 77 %.

Unfortunately, it was not possible to perform simulations for combustion temperatures around  $\approx 800^\circ\text{C}$ . This is caused by the fact that the model described is limited to the condensation of one aerosol forming component (i.e.  $\text{K}_2\text{SO}_4$ ) only. As alkaline sulphate already starts to nucleate around  $\approx 1000^\circ\text{C}$ , almost all alkaline sulphate is in a solid state at  $\approx 800^\circ\text{C}$ . Consequently, only particle deposition will occur in the heat exchanger during these simulations.

However, a worst case estimation can be derived assuming that all  $\text{K}_2\text{SO}_4$  for combustion temperatures  $\approx 800^\circ\text{C}$  is already transformed into particles (neglecting  $\text{ZnO}$  due to its low concentration). Based on fuel analyses and the aerosol formation process as described in Sec. 3.2, it revealed that the maximum potential for aerosol formation was  $48 \text{ mg}/\text{Nm}^3$ , from which 85 wt. % consists of alkaline sulphate. Consequently, based on this analysis  $40.8 \text{ mg}/\text{Nm}^3$  of aerosol forming vapours should already be transformed into particles, whereas the remaining part of the aerosol forming compounds is assumed to be still in the gaseous phase. Assuming that all gaseous compounds in HE5 condense on heat exchanger surfaces and approximately 25 % of the particles deposit on heat exchanger surfaces (see Sec. 4.5), then it is revealed that the aerosol concentration downstream the aerosol condensing heat exchanger for combustion temperatures around  $\approx 800^\circ\text{C}$  amounts to  $30.6 \text{ mg}/\text{Nm}^3$ . Based on this worst case analysis, an aerosol emission reduction up to 37 % is estimated. Comparing the estimated aerosol emission reduction with aerosol emission reduction, based on measurements inside the furnace and downstream HE5, then it appears that this value amounts to 52 %. A difference of 15 % can be observed between the analysis described and measurement data provided. One reason for this difference can be that the K release, as used for the worst case estimation, differs from the actual K release factor.

### 6.3 Fin tube heat exchanger

The principle and applicability of the aerosol condenser has been proven by both the gas to gas heat exchanger (HE4) and the insulated plate type heat exchanger (HE5). Thereby the first step towards a commercially viable heat exchanger design has been made. Several other heat exchanger designs have been investigated in order to find an alternative heat exchanger geometry applicable to aerosol reduction for small-scale biomass combustion plants.

The results of the insulated plate heat exchanger (HE5) open the possibility to adapt a common fin tube heat exchanger design as being used for instance for economisers. For the sake of simplicity, this fin tube heat exchanger will be denoted as HE6 in this work. The required temperature profile can be achieved by reducing the heat transfer through the fin by using stainless steel (having a low heat conduction coefficient) and introducing an extra heat resistance in the fins by punching holes.

### 6.3.1 Description of HE6, fin tube heat exchanger

Starting from a layout as applied in for instance economisers, the fins are elongated after a heat resistance introduced by punching holes to realise a high temperature section in the heat exchanger passage, see Fig. 6.15 and 6.16. For the calculations of the temperature profile, the design code, originally developed by LEVEL energy technology for the gas to gas heat exchanger [47, 49], is adapted for fin tube heat exchangers see Fig. 6.17. Within the limits of the lay-out, the heat exchanger is designed to mimic the temperature profile of the insulated plate type heat exchanger.

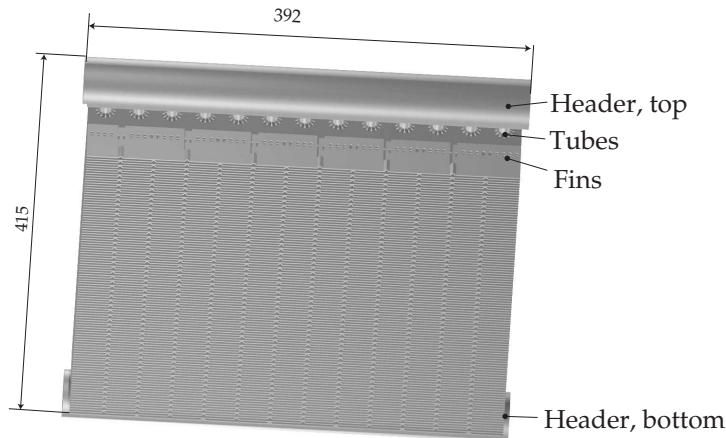


**Figure 6.15.** Drawing of fin tube heat exchanger.

The fin tube heat exchanger consists of a top and bottom header that are connected by 13 rows of tubes on which the fins are mounted, see Fig. 6.15. The top and bottom headers have dimensions of  $\varnothing 38.4 \times 2 \text{ mm}$ , whereas the vertical tubes have dimensions of  $\varnothing 10 \times 1 \text{ mm}$ . Because the heat exchanger is directly in contact with the flue gas, both the headers and the tubes are made of stainless steel AISI 316. The height of the fin tube heat exchanger is  $415 \text{ mm}$ . Cooling water enters the heat exchanger via the bottom header and flows in upward direction to the top header. On its way up, heat is transferred from the fins to the cooling water. Flue gas flows between the fins. During the cooling process of the flue gas, aerosol forming vapours will partially deposit on the fins.

The fins of the fin tube heat exchanger through which the flue gas flows are made of heat resistant stainless steel AISI 310. The distance between the fins is  $2 \text{ mm}$ , whereas the width of the fins is  $392 \text{ mm}$ . Consequently, the hydraulic diameter  $D_h \approx 4 \text{ mm}$ . The total length of the fins is  $70 \text{ mm}$ , so that a good accessibility is achieved and cleaning becomes rather easy. The distance from the centre of the water channels to the hot end of the fins is  $50 \text{ mm}$ , resulting in a small view-factor from the cold tubes towards the hot furnace so that radiative heat transfer is minimised. Instead of

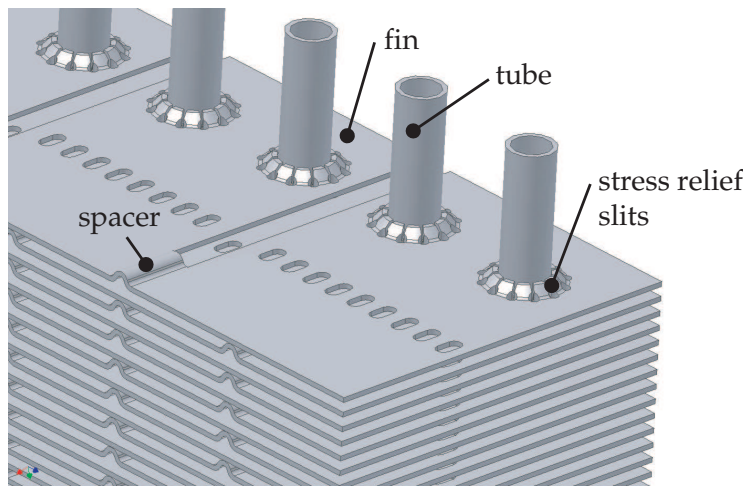


**Figure 6.16.** Detailed drawing of fin tube heat exchanger.

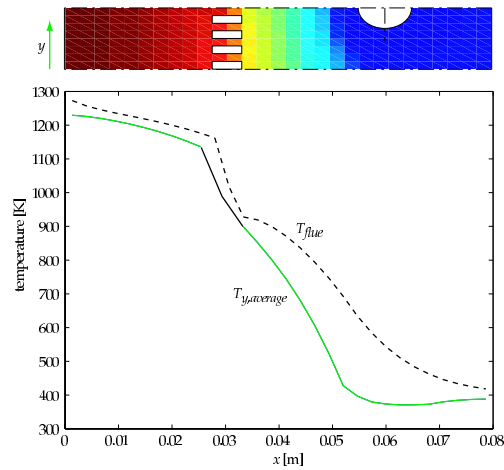


**Figure 6.17.** Calculated average temperature of the fin and the flue gas using an inlet flue gas temperature of  $1000\text{ }^{\circ}\text{C}$  and a cooling water temperature of approximately  $20\text{ }^{\circ}\text{C}$ .

applying insulation material as provided in the insulated plate type heat exchanger a heat resistance is built into the plates by removing material half way the fins, see Fig. 6.16. In this way a high temperature zone is created wherein the condensation process should take place at a rather low heat exchanging power. The remaining area around the water cooled tubes is designed as a conventional heat exchanger to achieve the required flue gas temperature near the outlet. The plates can be stacked in modules according to the nominal capacities of the heat exchanger. Slits are provided

in the fins around the water cooled tubes to prevent cracking due to thermal stresses. The fins on the hot ends (on the furnace side) are provided with bends that relieve the stresses and provide spacers while stacking the plates.

### 6.3.2 Results from test runs with HE6

#### Fuel and predicted aerosol composition

In Tab.6.4, the fuel used during the test runs performed with the fin tube heat exchanger (HE6) is characterised by its moisture content, ash content and chemical composition. As for all previous experiment, also for these experiments chemically untreated wood chips were used.

**Table 6.4.** Composition of chemically untreated wood chips used for the experiments with fin tube heat exchanger (HE6).

Explanations: d.b. ... dry base; w.b. ... wet base

		HE6
parameter	unit	average value <sup>a</sup>
Moisture content	wt. % (w.b.)	26.2
Ash content	wt. % (d.b.)	0.9
S	mg/kg (d.b.)	98
Cl	mg/kg (d.b.)	29
Ca	mg/kg (d.b.)	2230
Si	mg/kg (d.b.)	480
Mg	mg/kg (d.b.)	242
K	mg/kg (d.b.)	827
Na	mg/kg (d.b.)	24
Zn	mg/kg (d.b.)	11
Pb	mg/kg (d.b.)	< 5 <sup>b</sup>

<sup>a</sup> based on 1 fuel sample

<sup>b</sup> below detection limit

The K concentration of this fuel amounts to 827 mg/kg (d.b.), which is almost 33 % higher compared to the K concentration of the fuel used for test runs with HE5. Furthermore, the concentration Na amounts to 24 mg/kg (d.b.). The S concentration in the fuel is 98 mg/kg (d.b.). Comparing it with the S concentration in the fuels used for test runs with HE1, HE2 and HE5, it can be observed that this value is slightly lower. The Cl concentration, which is 29 mg/kg (d.b.), is approximately equal to the Cl concentration in the fuel used for HE5. The concentrations of Pb and Zn in the fuel are respectively < 5 mg/kg (d.b.) and 11 mg/kg (d.b.), which are of the same order compared to previous fuel compositions.

Based on the fuel composition as described in Tab.6.4, in combination with release factors as denoted in Tab. 3.1, a maximum potential for aerosol formation that

amounts to  $62 \text{ mg/Nm}^3$  (dry flue gas 13 vol.% oxygen) is estimated. A graphical representation of the predicted aerosol composition based on the fuel composition is depicted in Fig. 6.18.

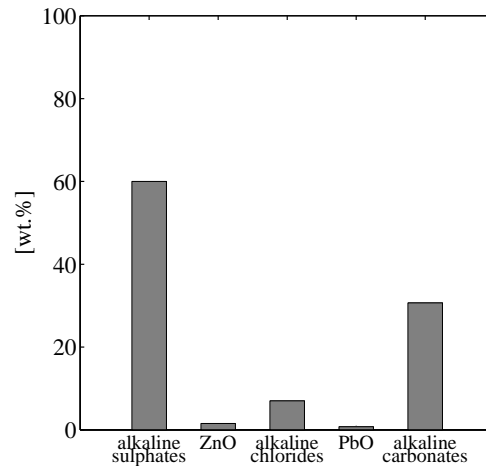


**Figure 6.18.** Aerosol composition calculated from the fuel composition during experiments performed with the fin tube heat exchanger.

The Cl concentration in the fuel applied during test runs with HE5 and HE6 are almost equal. Therefore, this is a nice example to see the influence of the higher K concentration in the fuel. Due to the almost equal Cl concentrations in the fuels, yields that the KCl concentrations in the flue gas and consequently also in the aerosols (see Fig. 6.18) are approximately equal for both test runs. Because of the higher K concentration compared to the fuel used for test runs with HE5, more K is available to form alkaline sulphate and carbonate. However, due to approximately equal S concentration in the fuel results that less alkaline sulphate (60 wt. %) and more alkaline carbonate (30 wt. %) are formed. Furthermore, the contribution ZnO is estimated to 2 wt. %, whereas the concentration PbO is estimated < 1 wt. %.

### Process control parameters

In the configuration, equal type-K thermocouples positioned downstream as well as upstream the heat exchanger, were installed to control the temperatures in the different zones of the furnace (see Fig. 5.1). In this way a good indication of the flue gas inlet temperature is obtained.

Just as for HE5, experiments were performed at two different flue gas temperatures in the secondary combustion zone. The first serie of experiments was conducted at as high as possible combustion temperatures ( $T_{sec} > 1000 \text{ }^\circ\text{C}$ ). The second series of experiments were conducted for combustion temperatures around  $800 \text{ }^\circ\text{C}$ . The flue gas temperatures in the secondary combustion zone as well as the start and end times



of the BLPI and HT – LPI measurements that were conducted simultaneously are shown in Fig. 6.19 and 6.20.

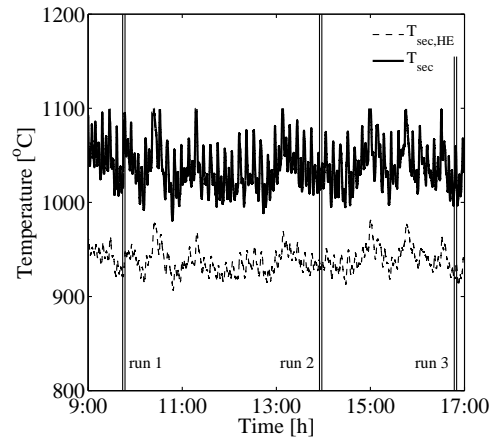


**Figure 6.19.** Temperature in the secondary combustion zone and the temperature near the inlet of the fin tube heat exchanger (HE6) during BLPI measurements at flue gas temperature in the secondary combustion zone  $> 1000$  °C. The vertical lines indicate the measurement periods.

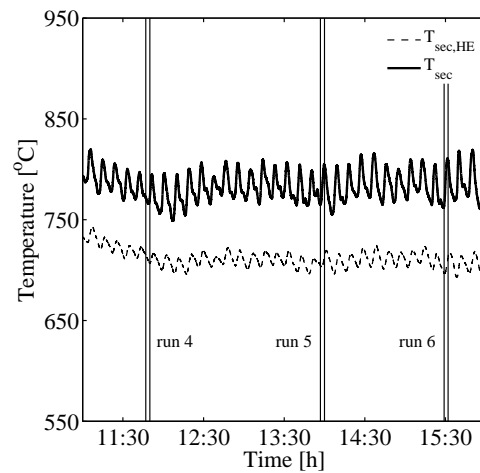


**Figure 6.20.** Temperature in the secondary combustion zone and the temperature near the inlet of the fin tube heat exchanger (HE6) during BLPI measurements at flue gas temperature in the secondary combustion zone of about  $800$  °C. The vertical lines indicate the measurement periods.

**Table 6.5.** Overview of process conditions during experiments at gas temperatures in the secondary combustion zone around 1050 °C with the fin tube heat exchanger (HE6).

Explanations:  $T_{sec}$  ... flue gas temperature in secondary combustion zone;  $T_{sec,HE}$  ... flue gas temperature near heat exchanger inlet;  $T_{boiler,out}$  ... flue gas temperature at boiler outlet;  $T_{HE,out}$  ... flue gas temperature at heat exchanger outlet. Note that  $T_{HE,out}$  is an average temperature based on single snapshot measurements.

run	$T_{sec}$ [°C]	$T_{sec,HE}$ [°C]	$T_{boiler,out}$ [°C]	$T_{HE,out}$ [°C]
1	1060 ± 31	930 ± 9	229 ± 3	160
2	1024 ± 8	931 ± 3	225 ± 3	160
3	1036 ± 15	926 ± 6	231 ± 3	160

**Table 6.6.** Overview of process conditions during experiments at flue gas temperatures in the secondary combustion zone around 800 °C with the fin tube heat exchanger (HE6).

Explanations:  $T_{sec}$  ... flue gas temperature in secondary combustion zone;  $T_{sec,HE}$  ... flue gas temperature near heat exchanger inlet;  $T_{boiler,out}$  ... flue gas temperature at boiler outlet;  $T_{HE,out}$  ... flue gas temperature at heat exchanger outlet. Note that  $T_{HE,out}$  is an average temperature based on single snapshot measurements.

run	$T_{sec}$ [°C]	$T_{sec,HE}$ [°C]	$T_{boiler,out}$ [°C]	$T_{HE,out}$ [°C]
4	768 ± 2	711 ± 3	182 ± 1	140
5	786 ± 15	705 ± 3	184 ± 1	140
6	794 ± 17	702 ± 5	184 ± 4	160

In Fig. 6.19 it can be observed that  $T_{sec}$  varied between 1000 and 1100 °C. The average flue gas temperature at that position, during six hour operation was  $1044 \pm 63$  °C. The rather large temperature fluctuations are mainly caused by the fact that the furnace operated at its maximum allowable temperature requiring a maximum performance of the control system. The temperature in the secondary combustion zone show rather large fluctuations, caused by the fact that no flue gas recirculation occurs at this high combustion temperature. On average,  $T_{sec,HE}$  that was close positioned at the heat exchanger inlet (see Fig. 5.1) was approximately 100 °C lower than the flue gas temperature upstream the heat exchanger (measured with thermocouple  $T_{sec}$ ).

The temperature fluctuations during a four hour operation for combustion temperatures around 800 °C were much smaller. On average  $T_{sec}$  was  $781 \pm 15$  °C. The smaller temperature fluctuations are caused by the fact that flue gas recirculation could be applied to control the furnace temperature, resulting in less temperature fluctuation compared to the temperature fluctuations at  $T_{sec} > 1000$  °C. The temperature difference between  $T_{sec}$  and the flue gas temperature near the heat exchanger inlet measured with  $T_{sec,HE}$  was limited to approximately 75 °C. On average the oxy-

gen content amounted to 11.7 *vol.%* related to dry flue gas during the measurements.

In Tab. 6.5 and 6.6 the average temperatures in the furnace as well as downstream the boiler and the heat exchanger during the impactor measurements are presented. Unfortunately, no continuous temperature measurements were performed downstream the heat exchanger. As an alternative, snapshot measurements were performed during the impactor measurements. On average, the flue gas temperatures at the outlet of HE5 were around 160 and 147 °C for combustion temperatures of respectively around 1050 and 800 °C measured by  $T_{sec}$ .

### Impactor measurements

An overview of the aerosol emissions for combustion temperatures around 1050 and 800 °C is given in Fig. 6.21 and 6.22. These figures contain information regarding the aerosol concentrations sampled in the furnace as well as downstream the boiler and HE6. All impactor measurements were performed simultaneously. For both temperatures, three measurements were performed to measure the aerosol concentrations at the different positions. The aerosol concentrations measured are shown as box plots. The box represent the 1<sup>st</sup> and 3<sup>rd</sup> quartile of the measurement results, while the lines in the boxes indicates the median values. The error indicators represent the minimum and maximum values identified.

As it can be observed in Fig. 6.21, the differences between the minimum and maximum concentration of aerosols downstream the boiler at  $T_{sec} \approx 1050^{\circ}C$  were quite small. The minimum and maximum concentrations amount to 30 and 32  $mg/Nm^3$  (dry flue gas and 13 *vol.%*  $O_2$ ). From previous experiments it is known that the estimated aerosol concentration based on fuel analyses and release rates from literature data were approximately 30 % higher compared to what was measured. As the aerosol concentration based on one singly fuel analysis as shown in Tab.6.4 is estimated to approximately 62  $mg/Nm^3$  (dry flue gas and 13 *vol.%*  $O_2$ ), the resulting difference between estimated and measured concentration is  $\approx 50$  %. The most obvious explanation for this difference compared to previous observations can be that the fuel as shown in Tab.6.4 was not a representative one for all series of test runs.

Besides low fluctuations in the aerosol concentration measured downstream the boiler, also low fluctuations downstream HE6 can be observed at  $T_{sec} \approx 1050^{\circ}C$ . The aerosol concentration measured downstream the heat exchanger was at minimum 5 and at maximum 7  $mg/Nm^3$ , which was significantly lower compared to the aerosol concentrations downstream the boiler. From this observation can already be derived that the precipitation efficiency for HE6 is quite good.

At first, low concentration of combustion particles could be observed in the secondary combustion zone. However, as SEM/EDX-analysis shows, the particles during HT – LPI at  $T_{sec} \approx 1050^{\circ}C$  almost exclusively consist of  $Cr_2O_3$ , which is assumed to be released from the material of the HT – LPI at this very high temperature. By taking into account thermodynamic restrictions it can be stated that the first formation of aerosols in the case of wood chips combustion should start at temperatures around 950 °C. Therefore, it can be concluded that up to the measurement port in the secondary combustion zone almost no aerosols have been formed during the experiments performed at  $T_{sec} \approx 1050$  °C.

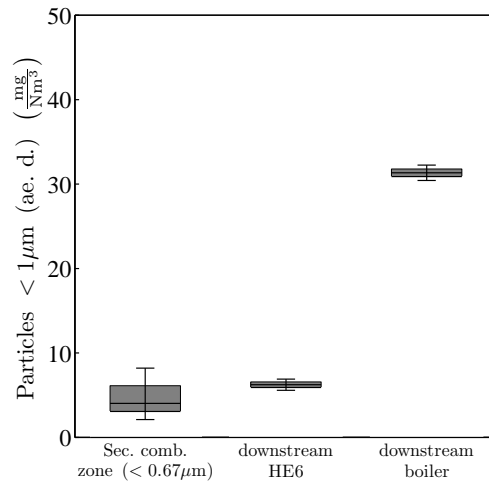


**Figure 6.21.** Concentration of aerosols in the flue gas sampled directly from the furnace, at boiler outlet and downstream insulated heat exchanger for test runs performed at flue gas temperatures in the secondary combustion zone of approximately  $1050\text{ }^{\circ}\text{C}$ .

Explanations: All concentrations related to dry flue gas and  $13\text{ vol.}\% \text{O}_2$ ; ae. d. ... aerodynamic particle diameter; number of BLPI measurements: boiler outlet 3, at heat exchanger outlet 3; number of HT – LPI measurements in secondary combustion zone 3; the boxes indicate the quartiles 25 % to 75 %, the line in the box displays the median value; the error indicator represents the maximum and minimum values; particles determined in the secondary combustion zone almost exclusively consist of  $\text{Cr}_2\text{O}_3$ , which is assumed to be released from the HT – LPI material.

In Fig. 6.22 the average aerosol concentration measured at three different positions is depicted during operation at flue gas temperatures in the secondary combustion zone around  $800\text{ }^{\circ}\text{C}$ . From this figure it can be observed that the aerosol concentrations downstream the boiler varies between  $21$  and  $26\text{ mg/Nm}^3$ , which is significantly lower from when applying  $T_{sec} \approx 1050\text{ }^{\circ}\text{C}$  (see Fig. 6.21). Comparing to the aerosol concentration downstream the fin tube heat exchanger at  $T_{sec} \approx 1050\text{ }^{\circ}\text{C}$ , with the concentration of aerosols downstream the fin tube heat exchanger at  $T_{sec} \approx 800\text{ }^{\circ}\text{C}$ , then this concentration is almost twice as high. The aerosol concentrations downstream HE6 at  $T_{sec} \approx 800\text{ }^{\circ}\text{C}$  is between  $6$  and  $13\text{ mg/Nm}^3$ . This is caused by the fact that aerosols are already formed in the secondary combustion zone as already mentioned in Sec. 6.1.3. Furthermore, this observation confirms the trend that could already be observed from test runs with HE5 that lower aerosol emission reductions can be expected for decreasing combustion temperatures. Contrary to the HT – LPI performed at  $T_{sec} \approx 1050\text{ }^{\circ}\text{C}$ , no  $\text{Cr}_2\text{O}_3$  is observed in the aerosols sampled at flue gas temperatures around  $800\text{ }^{\circ}\text{C}$ . The concentration of aerosols sampled in the secondary combustion zone at  $T_{sec} \approx 800\text{ }^{\circ}\text{C}$  varied between  $14$  and  $22\text{ mg/Nm}^3$ . Compared to the aerosol concentration sampled downstream HE6 at equal flue gas temperatures, it can be observed that this aerosol concentration is lower than the concentration of

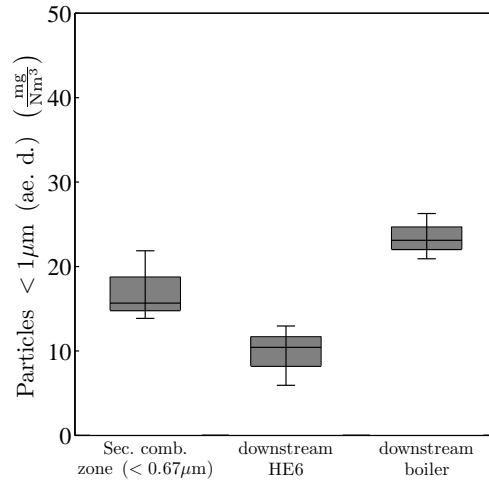


**Figure 6.22.** Concentration of aerosols in the flue gas sampled directly from the furnace, at boiler outlet and downstream insulated heat exchanger for test runs performed at flue gas temperatures in the secondary combustion zone of approximately 800 °C.

Explanations: All concentrations related to dry flue gas and 13 vol.%  $O_2$ ; ae. d. ... aerodynamic particle diameter; number of BLPI measurements: boiler outlet 3, at heat exchanger outlet 3; number of HT – LPI measurements in secondary combustion zone 3; the boxes indicate the quartiles 25 % to 75 %, the line in the box displays the median value; the error indicator represents the maximum and minimum values.

aerosols in the furnace. So it can be concluded that besides vapour deposition also particle deposition occurs inside the heat exchanger. Unfortunately, due to the complex geometry and temperature distribution inside HE6 it is not that straightforward to predict the deposition rate of already existing particles on heat exchanger surfaces.

Typical PSD's of aerosols downstream the boiler and HE6 as well as for the aerosols in the secondary combustion zone for combustion temperatures around 1050 and 800 °C are shown in Fig. 6.23 and 6.24.

In Fig. 6.23 a clear peak of the PSD regarding the aerosols downstream the boiler can be observed between particle diameters of 0.125  $\mu m$  and 0.25  $\mu m$  for  $T_{sec} \approx 1050^\circ C$ . As for all three BLPI measurements downstream the boiler the concentration aerosols for each particle size class was approximately equal, the resulting standard deviations for each particle size class becomes also low, indicated by the small error bars. Comparing the PSD as depicted in Fig. 6.23 with previous PSD's, determined at approximately equal conditions and at the same position (see Fig. 5.7, 5.9, 5.9, 5.17 and 6.11), again no significant differences can be observed.

A comparison between of the PSD of aerosols downstream the insulated plate type heat exchanger (HE5) is made, as the fin tube heat exchanger (HE6) should be a commercially alternative design for this heat exchanger. Regarding the PSD of the aerosols downstream HE6 at a combustion temperature around 1050 °C, no

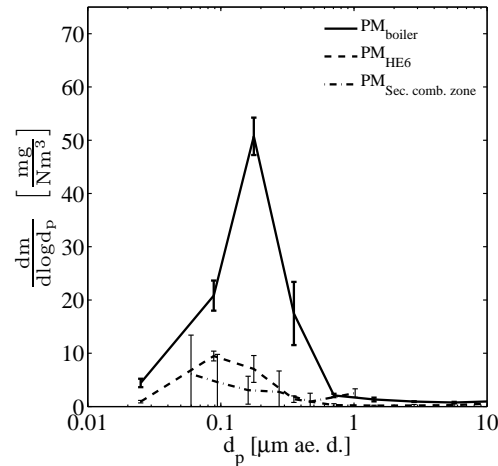


**Figure 6.23.** Average PSD downstream the ordinary boiler and the insulated heat exchanger (BLPI measurements) as well as inside the furnace (HT – LPI measurements) at flue gas temperatures in the secondary combustion zone of about  $1050\text{ }^{\circ}\text{C}$ .

Explanations: All concentrations are expressed in in  $\text{mg}/\text{Nm}^3$  and related to dry flue gas and  $13\text{ vol.}\% \text{O}_2$ ; number of BLPI measurements: 3; number of HT – LPI measurements: 3; subscript *boiler* ... boiler outlet; subscript *HE6* ... aerosol condensing heat exchanger outlet; subscript *Sec. comb. zone* ... secondary combustion zone; ae. d. ... aerodynamic particle diameter.

significant differences in shape as well as in values can be observed compared to the average PSD of the aerosols downstream HE5. The peak of the PSD's of the aerosols are for both measurements at a cut diameter of  $0.125\text{ }\mu\text{m}$ .

As for HE5, also for HE6 HT – LPI measurements were performed inside the secondary combustion zone. In comparison with the test runs performed with HE5, these measurements were performed simultaneously with the BLPI measurements. However, as already mentioned, SEM/EDX-analysis show that the particles during HT – LPI at  $T_{sec} \approx 1050^{\circ}\text{C}$  almost exclusively consist of  $\text{Cr}_2\text{O}_3$ , which is assumed to be released form the material of the HT – LPI at this very high temperature. Consequently, it is meaningless to discuss the large variations of the PSD of the particulate matter measured inside the furnace, as this has nearly nothing to do with the aerosol particles in the furnace.

In Fig. 6.24 a graphical representation of the resulting PSD's of the aerosols formed inside the furnace as well as downstream the boiler and HE6 during operation at furnace temperatures of  $\approx 800\text{ }^{\circ}\text{C}$  are shown. Again, a comparison can be made with the PSD as shown in Fig. 6.12 for HE5, also performed at furnace temperatures around  $800\text{ }^{\circ}\text{C}$ . Whereas the peak of the PSD of the aerosols formed downstream the boiler during experiments with HE5 at  $T_{sec} \approx 800\text{ }^{\circ}\text{C}$  (see Fig. 6.12) was between particle sizes of  $0.125\text{ }\mu\text{m}$  and  $0.5\text{ }\mu\text{m}$ , the peak of the average PSD of the aerosols downstream the boiler during experiments with HE6 was clearly between  $0.125\text{ }\mu\text{m}$

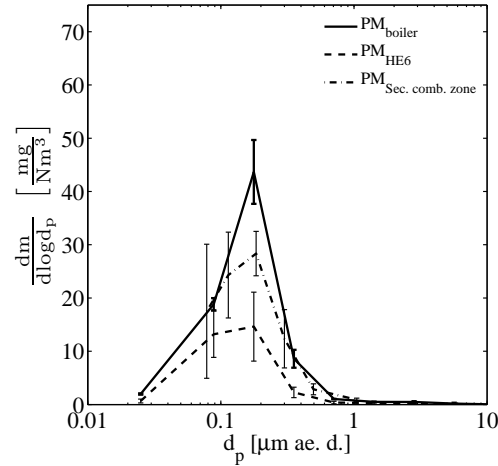


**Figure 6.24.** Average PSD downstream the ordinary boiler and the insulated heat exchanger (BLPI measurements) as well as inside the furnace (HT – LPI measurements) at flue gas temperatures in the secondary combustion zone of about  $800\text{ }^{\circ}\text{C}$ .

Explanations: All concentrations are expressed in in  $\text{mg}/\text{Nm}^3$  and related to dry flue gas and  $13\text{ vol.}\% \text{O}_2$ ; number of BLPI measurements: 3; number of HT – LPI measurements: 3; subscript *boiler* ... boiler outlet; subscript *HE6* ... aerosol condensing heat exchanger outlet; subscript *Sec. comb. zone* ... secondary combustion zone; ae. d. ... aerodynamic particle diameter.

and  $0.25\ \mu\text{m}$ .

Whereas for combustion temperatures around  $1050\text{ }^{\circ}\text{C}$  a clear peak of the PSD of the aerosols downstream HE6 could be observed at a cut diameter of  $0.125\ \mu\text{m}$ , the peak of the average PSD of the aerosols downstream HE6 at  $T_{sec} \approx 800\text{ }^{\circ}\text{C}$  is now shifted towards slightly larger particle sizes i.e. towards a cut diameter of  $0.25\ \mu\text{m}$ . Besides a shift towards larger particle sizes, also a shift towards larger particle concentrations can be observed. Both shifts indicate higher particulate matter emissions that could already be observed in Fig. 6.22. Furthermore, the average PSD of the aerosols downstream HE6 shows approximately the same shape as for the average PSD of the aerosols downstream HE5. Both PSD's at furnace temperatures of  $\approx 800\text{ }^{\circ}\text{C}$  show a peak between  $0.0625\ \mu\text{m}$  and  $0.25\ \mu\text{m}$ .

The concentration aerosols at  $T_{sec} \approx 800\text{ }^{\circ}\text{C}$  is higher in the furnace compared to concentration of aerosols downstream HE6 (see Fig. 6.22). As thermophoresis is very effective regarding particle deposition in the particle size range between  $0.1\ \mu\text{m}$  and  $1.0\ \mu\text{m}$  (see Fig. 4.11), yields that also a certain share of these particles is precipitated from the flue gas.

The measured particle fractions  $< 1\ \mu\text{m}$  sampled downstream the boiler and HE6 are used to calculate the resulting aerosol emission reduction according to Eq. 5.1. In Fig. 6.25 these data are depicted. The measured particle fractions  $< 1\ \mu\text{m}$  for combustion temperatures above  $1000\text{ }^{\circ}\text{C}$  were quite constant as could also be observed

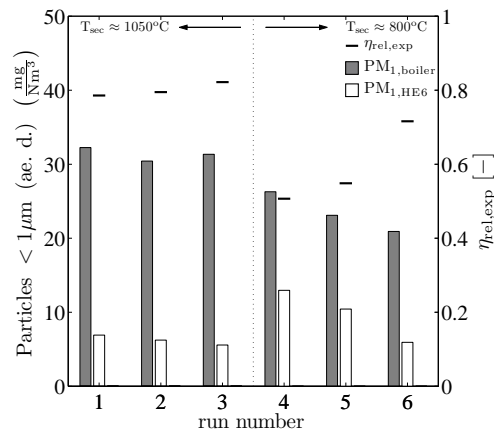


**Figure 6.25.** Overview of the aerosol emission reductions compared to ordinary boiler design using an insulated plate type heat exchanger.

Explanation: All concentrations related to dry flue gas and 13 vol.% O<sub>2</sub>; ae. d. ... aerodynamic particle diameter;  $\eta_{rel,exp}$  ... particulate emission reduction compared to ordinary boiler design, calculated according to Eq. 5.1; subscript *boiler* ... boiler outlet; subscript *HE* ... aerosol condensing heat exchanger outlet.

in Fig. 6.21. Consequently, the average aerosol emission reduction obtained by the aerosol condensing fin tube heat exchanger compared to the current boiler design is also quite constant at  $80 \pm 2$  %. Furthermore, the aerosol average emission reduction at  $T_{sec} \approx 800$  °C is  $59 \pm 11$  %.

### Chemical composition of aerosols sampled downstream the boiler and the aerosol condensing heat exchanger

Wet chemical analyses of the BLPI samples were performed to determine the composition of the particles formed. The results of these analyses as well as the corresponding emission reduction per element are depicted in Fig. 6.26 and 6.27. To determine the chemical composition of the particles, a certain amount of mass on the impactor stages is required. Because the particle fraction  $> 1 \mu m$  is negligible (see Fig. 6.23 and 6.24), yields that these impactor stage could not be analysed. The reduction per element is determined according to the relation as described in Eq. 5.2.

As can be observed in Fig. 6.26 and 6.27, K, S and in less extend Cl are the main aerosol forming elements. In these figures it can be seen that the concentrations for all aerosol forming elements investigated at the boiler outlet are higher than at the outlet of HE6.

On an element basis the reduction of K and S related to the ordinary boiler is  $\approx 70$  % at  $T_{sec} \approx 1050$  °C, whereas the Cl reduction (88 %) is slightly higher. In first order approximation, these reductions are in line with the total aerosol emission reduction ( $\approx 80$  %). Slight differences can be observed when applying a combustion



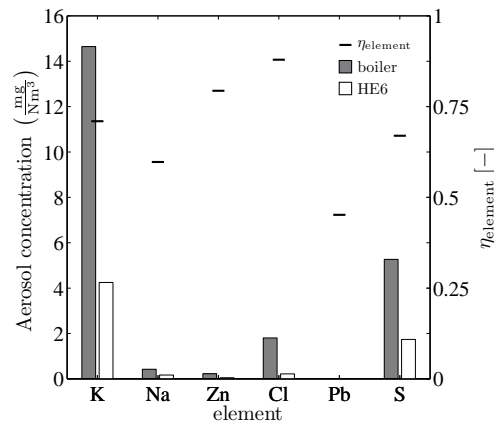


**Figure 6.26.** Comparison of the concentration of aerosol forming elements at boiler outlet and downstream the aerosol condensing fin tube heat exchanger at a flue gas temperature in the secondary combustion zone of about  $1050\text{ }^{\circ}\text{C}$ .

Explanation: All concentrations related to dry flue gas and  $13\text{ vol.}\% \text{O}_2$ .

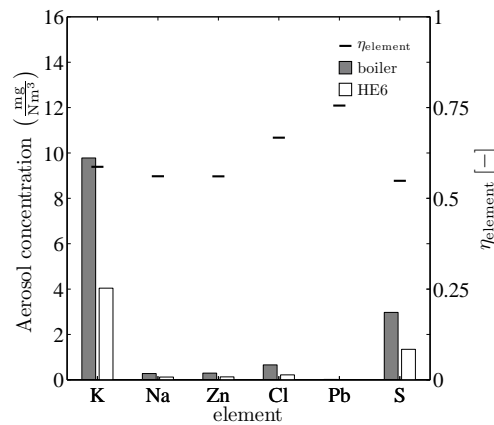


**Figure 6.27.** Comparison of the concentration of aerosol forming elements at boiler outlet and downstream the aerosol condensing fin tube heat exchanger at a flue gas temperature in the secondary combustion zone of about  $800\text{ }^{\circ}\text{C}$ .

Explanation: All concentrations related to dry flue gas and  $13\text{ vol.}\% \text{O}_2$ .

temperature  $\approx 800\text{ }^{\circ}\text{C}$ . At this lower combustion temperature, K is reduced by 59 %, whereas S is reduced by 55 %. These reductions are in line with the total aerosol emission reduction, which was  $\approx 59\%$ . The Cl reduction at  $T_{\text{sec}} \approx 800\text{ }^{\circ}\text{C}$  (77 %) is significantly higher compared to the total aerosol emission reduction. This behaviour can be explained by the fact that K and S are most probably already transformed

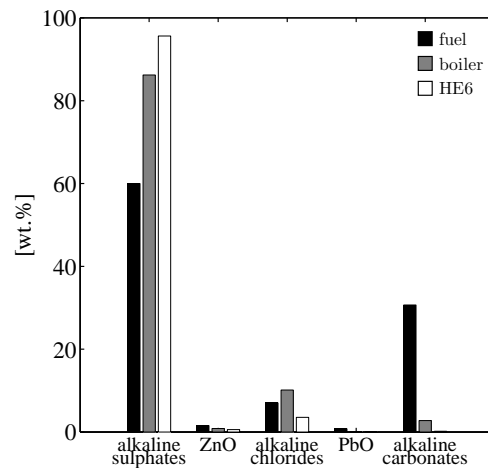


**Figure 6.28.** Comparison of the aerosol composition based on a fuel analysis and determined by wet chemical analysis of the aerosols sampled downstream the boiler outlet and downstream the aerosol condensing fin tube exchanger at a flue gas temperature in the secondary combustion zone of about  $1050\text{ }^{\circ}\text{C}$ .

Explanation: All concentrations related to dry flue gas and  $13\text{ vol.}\% \text{O}_2$ .

into solid  $\text{K}_2\text{SO}_4$  particles near the inlet of HE6, contrary to  $\text{KCl}$  that is still in the gaseous phase. Consequently, at lower temperatures,  $\text{KCl}$  can still be condensed on heat exchanger surface whereas  $\text{K}_2\text{SO}_4$  particles can only be precipitated by external forces. Concerning the heavy metal concentrations in the aerosols it can be observed that the contribution of  $\text{Pb}$  and  $\text{Zn}$  are almost negligible.

In Fig. 6.28 the chemical composition of the aerosols sampled with the BLPI downstream the two sampling points during experiments at  $T_{sec} \approx 1050\text{ }^{\circ}\text{C}$  are compared with predicted aerosol compositions derived from fuel analysis as shown in Tab. 6.4 and release factors obtained from literature (see Tab. 3.1).

Wet chemical analysis show that the concentration of alkaline sulphate downstream the boiler amounts to  $86\text{ wt.}\%$ , whereas the aerosols downstream the aerosol condenser almost exclusively consists of alkaline sulphate ( $96\text{ wt.}\%$ ). Comparing these values with the predicted concentration of alkaline sulphate ( $60\text{ wt.}\%$ ), then the predicted concentration is much lower. Furthermore, it can be observed that almost no alkaline carbonate is formed, contrary to what is expected from the fuel data. As already mentioned, the  $\text{K}$  concentration in the fuel amounts to  $827\text{ mg/kg (d.b.)}$ , which was quite high compared to previous analyses. These observations indicate that most probably less  $\text{K}$  is released from the fuel to the flue gas, resulting in rather low concentrations of alkaline carbonate. Another problem that might cause this difference between expectations and results obtained by wet chemical analysis is that only one fuel sample was analysed, which was apparently not representative for the composition of the fuel used during the experiments, which is already mentioned before.

### Chemical composition of aerosols sampled at high temperatures directly from the secondary combustion zone

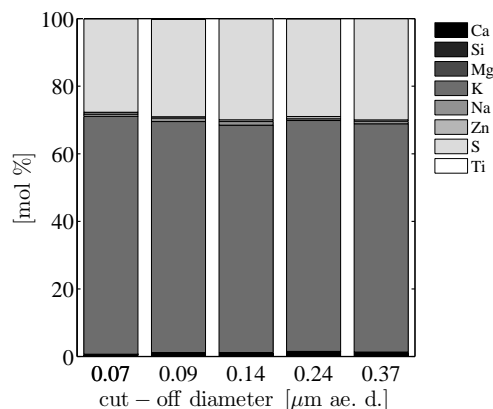


**Figure 6.29.** Chemical composition of aerosols in the flue gas sampled at high temperatures directly from the secondary combustion zone during the experiments performed at a flue gas temperature in the secondary combustion zone around  $800\text{ }^{\circ}\text{C}$ .

Explanations: bar charts show the results of area scan EDX analyses; results normalised to 100 % not considering O, Pt (material of sampling foil), Cr (component of the alloy of stainless steel 1.4841) and C (used for coating of the sample); measurement performed at a mean furnace temperature of  $789\text{ }^{\circ}\text{C}$  (secondary combustion zone); ae. d. ... aerodynamic particle diameter.

The chemical composition of the aerosols in the flue gas sampled at high temperatures directly from the secondary combustion zone of the furnace is depicted in Fig. 6.29. The aerosols sampled with the HT – LPI were subsequently analysed by means of SEM/EDX.

As can be seen, the aerosols almost exclusively consist of  $\text{K}_2\text{SO}_4$  with small amounts of Ca, Zn and Na. These results correspond well with the results achieved for aerosols sampled at boiler outlet and downstream the aerosol condenser. Main elements of the aerosols were K and S, no Cl was found in the hot furnace due to the high temperature. Moreover, low amounts of Zn and Na were identified for all measurement ports. Based on this analysis it can be concluded that  $\text{K}_2\text{SO}_4$  is the first component which forms particles.

## 6.4 Closure

From theory it was known that promoting condensation of aerosol forming vapours on heat exchanging surfaces in combination with relatively large diameters is accompanied by decreased heat transfer rates. Experiments with narrow channeled heat exchangers with tube dimensions of  $1.07\text{ mm}$  showed blocking of heat exchanger passages with coarse fly ash particles. Cleaning of such small tubs was not easy. Because of this a plate type heat exchanger was developed exhibiting a plate distance of  $3\text{ mm}$ . Insulation material between the flue gas passages and the cooling water channels was applied to tone down the temperature gradient of the flue gas, so that condensation of aerosol forming vapours towards heat exchanging surfaces was promoted.

One major disadvantage of applying insulation material in a heat exchanger is that an increased surface area is required for heat transfer. This in combination with the additional insulation material results in a voluminous heat exchanger, thus requiring a lot of material. Therefore, an insulated heat exchanger is from an economic point of view not attractive.

To achieve a commercially attractive design, a fin tube heat exchanger made of heat resistant stainless steel was developed and tested. This heat exchanger could operate even at flue gas temperatures up to  $1000\text{ }^{\circ}\text{C}$ . Furthermore, this heat exchanger design exhibits a good accessibility so that cleaning was not that difficult and also requires less material. These properties, together with a sufficient reduction of fine particulate matter should draw a distinction between all previously tested heat exchangers.

The distance between the fins in the final fin tube heat exchanger design is  $2\text{ mm}$ , so that the resulting hydraulic diameter is  $\approx 4\text{ mm}$ . A heat resistance build into the fins should decrease the temperature gradient of the flue gas as is achieved by insulation in the insulated plate type heat exchanger. Furthermore, relatively flexible connections in the fins around the tubes and at the hot end of the fins make sure that thermal stresses are limited.

Experiments performed with this prototype heat exchanger showed good results regarding the fine particulate emission reduction. Experiments have been conducted for combustion temperatures of about  $800$  and  $1050\text{ }^{\circ}\text{C}$ . HT – LPI measurements downstream the boiler and the fin tube heat exchanger as well as HT – LPI measurements inside the secondary combustion zone were performed. Based on BLPI measurements quite constant aerosol emission reductions of about  $80\%$  could be achieved using  $T_{sec} \approx 1050\text{ }^{\circ}\text{C}$ . Decreasing the furnace temperature to  $800\text{ }^{\circ}\text{C}$  resulted in particle formation inside the secondary combustion zone, confirmed by HT – LPI measurements in that zone.

Wet chemical analysis showed that the chemical composition of the particles sampled downstream the fin tube heat exchanger and the boiler at  $T_{sec} \approx 1050\text{ }^{\circ}\text{C}$  were approximately equal, indicating that the heat exchanger design does not influence the chemical composition. At  $T_{sec} \approx 800\text{ }^{\circ}\text{C}$  more Cl is precipitated in the heat exchanger tested than in the ordinary boiler. This is mainly caused by the fact that alkaline chlorides are formed at temperatures below  $600\text{ }^{\circ}\text{C}$ . Because of this, it is most likely that this compound is precipitated on heat exchanger surfaces instead of forming particles via nucleation or condensation. SEM/EDX analysis of the aerosols

sampled inside the secondary combustion zone at  $T_{sec} \approx 800$  °C showed that the aerosols sampled exclusively consist of  $K_2SO_4$  with small shares of Ca, Zn and Na.

Stimulating condensation of aerosol forming vapours on heat exchanger surfaces actually results in fouling of the heat exchanger. The condensed ash vapours forms a powdery layer on the heat exchanger surfaces that can easily be removed by pressurised air or by knocking. To remove this fouling layer, aerosol condensing heat exchangers have to be adopted with a cleaning system. However, the design of an appropriate heat exchanger cleaning system is a topic for further investigation.

## Chapter 7

# Conclusions

In this work, the feasibility of reducing aerosol emissions (particles  $< 1 \mu m$ ) during combustion of chemically untreated wood in small-scale biomass combustion plants is investigated. Aerosol forming compounds are released from the fuel to the gas phase. Subsequently these compounds undergo gas phase reactions. When the flue gas temperature decreases, these aerosol forming compounds can become supersaturated, resulting in aerosol formation by homogeneous nucleation or condensation on already existing surfaces. As current boiler designs aim at minimisation of condensation of aerosol forming compounds on heat exchanging surfaces, it should also be possible to stimulate aerosol forming vapours to condense on these surfaces.

An analytical approach incorporating heterogeneous- and wall condensation (chapter 2) indicates a significant reduction of aerosol emissions by wall condensation by preference when sufficient heat exchanging area is provided and the flow is laminar. A crucial parameter in the model is the number concentration of the particles formed near the heat exchanger inlet. Estimations in combination with experiments show that even for high particle number concentrations in the furnace immediately above the fuel bed, the concentration near the heat exchanger is around  $1 \cdot 10^{13} Nm^{-3}$  due to coagulation processes. Although the simplifications made in deriving the model prohibit a quantitative comparison with experiments, the results justify further research.

As current boilers mainly use round tubes, the model was firstly extended to this geometry. The model derived include particle formation by homogeneous nucleation assuming that  $K_2SO_4$  is the dominant compound in aerosol formation. Wet chemical analysis and SEM/EDX analysis of aerosols sampled inside a furnace by use of a high-temperature low pressure impactor (HT – LPI) as well as downstream the boiler by use of a Berner-type-low-pressure impactor (BLPI) confirm this assumption (chapter 5 - 6). A sensitivity analysis revealed that a significant aerosol emission reduction of about 80 % can be achieved for tubes with dimensions in the order of 1 mm. Increasing the tube dimension rapidly results in lower aerosol emission reductions. Coagulation processes inside heat exchanger passages are of minor interest when the formation of new particles by homogeneous nucleation is widely suppressed due to the high aerosol concentration near the heat exchanger inlet. Reducing the cooling rate,

i.e. by decreasing the temperature gradient of the flue gas, results in higher aerosol emission reductions, caused by the strong non linear dependency of the saturation vapour pressure on temperature. This effect enhances the emission reduction by increasing the heat exchanging surface (chapter 6).

Classical Nucleation Theory (CNT) is invoked to describe the particle formation process via homogeneous nucleation. As no measurement data of the surface tension of  $K_2SO_4$  could be found in literature, a parachor method is used to predict the surface tension. Despite reliable input parameters of the surface tension prediction, the parachor method itself is only accurate within approximately 10 %. For rather low initial particle number concentrations near the heat exchanger inlet ( $N_{tot,ini} \ll 1 \cdot 10^{13} Nm^{-3}$ ), deviations in the predicted wall condensation rate up to more than 50 % could be observed. However, using a number concentration of particles near the heat exchanger inlet of about  $1 \cdot 10^{13} Nm^{-3}$ , the results are stable within 2 % when varying the value of the surface tension by  $\pm 10$  %.

In laminar flow, the effect of the Saffman lift force and thermophoresis on aerosol deposition is investigated by extending the model to two dimensions. For 1 mm tubes the additional effect is estimated to be below 5 % compared to the total available concentration of aerosol forming compounds. Increasing tube dimensions to 10 mm increases this value slightly above 10 % as the size of the depositing particles becomes larger due to a lower condensation rate of aerosol forming vapours on heat exchanger surfaces. Thermophoresis is more effective in particle deposition on heat exchanger surfaces than lift force. Particle deposition efficiencies of particles in the heat exchanger by thermophoresis up to about 18 % could be achieved in cylindrical tubes.

Based on the simulation results, three water cooled heat exchangers that stay close to conventional boiler designs were designed and tested to investigate whether decreasing the tube diameter indeed results in a reduction of fine particulate matter emissions (chapter 5). The heat exchangers designed exhibit tube dimensions of 12.50 (HE1), 6.20 (HE2) and 1.07 mm (HE3). The combustion temperatures during the measurements varied around 1000 °C. The mutual ratio of the aerosol concentration downstream the heat exchanger tested and the ordinary boiler measured simultaneously was a measure for the aerosol emission reduction. Average aerosol emission reductions compared to ordinary boiler designs of respectively 28 and 36 % could be achieved using heat exchangers with tube dimensions of respectively 12.50 and 6.20 mm. Experiments performed with a water cooled heat exchanger exhibiting a hydraulic diameter of 1.07 mm (HE3) were not successful. Due to the lack of insulation near the heat exchanger inlet, heat transfer in the vicinity of the heat exchanger inlet was already significant, lowering the inlet temperature to 760 °C and leading to aerosol formation before the heat exchanger. Therefore, a compact laminar counter-flow gas to gas heat exchanger with a hydraulic diameter of 2.22 mm (HE4) originally developed for recuperative burners was applied and showed an aerosol emission reduction of about 70 %. The influence of the cooling rate is verified by experiments with a water cooled heat exchanger consisting of rectangular flue gas passages with a hydraulic diameter of 3 mm that are covered with insulation material (HE5). Experiments at a combustion temperature of 1000 °C resulted in an aerosol reduction

compared to ordinary boiler designs of about 80 % while at combustion temperatures of 800 °C the reduction still amounted to 64 %.

The dimensions needed to achieve significant aerosol reductions are comparable to commonly used fin tube heat exchangers provided that the cooling rate can be influenced and the capability to withstand a high temperature. Even when using heat resistant stainless steel for the fins, it was necessary to introduce an extra heat resistance in the form of holes. This design gave comparable aerosol emission reductions related to ordinary boiler designs of 80 % at at combustion temperatures of  $\approx 1050$  °C. Decreasing combustion temperatures to approximately 800 °C still resulted in aerosol emission reduction between 51 and 55 %.

## 7.1 Future outlook

At this point it is concluded that an applicable design for aerosol condensers is viable. Although not part of this research, it was observed during experiments that a powdery layer builds up on the heat exchanger surfaces that could easily be removed by knocking or pressurised air. Provided that an adequate cleaning system is installed, aerosol emissions can cost efficiently be reduced. The design of an appropriate heat exchanger cleaning system is a topic for further investigation.

It has to be noticed that the heat exchanger can be optimised for material use such that the holes in the fins can be left out. Furthermore, it would be favourable if the relatively expensive laser cutting process used to produce the fins of the fin tube heat exchanger could be replaced by a more common punching process as used in mass production. However, it is noticed that punching could cause small cracks near the edge of the surfaces. As large temperature gradients in the fins can rapidly result in relatively high thermal stresses, yields that these small crack can rapidly grow to large cracks, resulting in an irreparable damage. Because of this, more investigation regarding the production method is required to arrive at a production method for mass production.





# Bibliography

- [1] M.B. Allen and O.G. Raabe. Slip correction measurements of spherical solid aerosol particles in an improved millikan apparatus. *J. Aerosol Sci.*, 4:269–286, 1985.
- [2] J.C. Barret and T.J. Baldwin. Aerosol nucleation and growth during laminar tube flow: maximum saturations and nucleation rates. *J. Aerosol Sci.*, 31(6):633–650, 2000.
- [3] R. Becker and W. Döring. Kinetische Behandlung der Keimbildung in Äubersättigten Dämpfern. *Ann. Phys.*, 24:719–752, 1935.
- [4] A. Bejan. *Heat transfer*. John Wiley & Sons, New York, 1993.
- [5] G. Bertozzi and G. Soldani. Surface tension of molten salts. alkali sulphate and chloride-sulphate binary systems. *J. Phys. Chem.*, 71(5):1536–1538, 1965.
- [6] R.B. Bird, W.E. Steward, and E.N. Lightfoot. *Transport Phenomena, second edition*. John Wiley & Sons, New York, 2002.
- [7] C. Braun-Fahrländer. Health effects of aerosols: what is the epidemiologic evidence? In *Proceedings of the IEA Seminar*, pages 11–18. Verenum, Zürich, 2001.
- [8] J.J.H. Brouwers. Particle collection efficiency of the rotational particle separator. *Powder Technology*, 92(2):89–99, 1997.
- [9] T. Brunner. *Aerosols and coales fly ashes in fixed-bed biomass combustion*. PhD thesis, Department of Mechanical Engineering, Eindhoven University of Technology, Eindhoven, 2006.
- [10] T. Brunner, M. Jöller, I. Obernberger, and F. Frandsen. Aerosol and fly ash formation in fixed bed biomass combustion systems using woody biofuels. In *12th European Conference and Technology Exhibition on Biomass for Energy, Industry and Climate Protection*, 2002.
- [11] T. Brunner, I. Obernberger, J.J.H. Brouwers, and Z. Preveden. Efficient and economic dust separation from flue gas by the rotational particle separator as an

- innovative technology for biomass combustion and gasification plants. In *Proceedings of the 10th European Bioenergy Conference*, pages 1630–1633. Rimpär, Germany, 1998.
- [12] C.Y. Cha and B.J. McCoy. Thermal force on aerosol particles. *Phys. Fluids*, 17:1375–1380, 1974.
- [13] K.A. Christensen, M. Stenholm, and H. Livbjerg. The formation of submicron aerosol particles, HCl and SO<sub>2</sub> in straw-fired boilers. *J. Aerosol Sci.*, 29(4):421–444, 1998.
- [14] C.J.J.M. de Best, H.P. van Kemenade, T. Brunner, and I. Obernberger. Particulate emission reduction in small-scale biomass combustion plants by a condensing heat exchanger. Accepted for publication.
- [15] EU. BIO – Aerosols, project ERK6 – CT – 1999 – 00003. Technical report, Graz University of Technology, 2003.
- [16] A.P.C. Faaij. Bio-energy in europe: changing technology choices. *Energy Policy*, 34:322–342, 2006.
- [17] G.W. Finger, J.S. Kapat, and A. Bhattacharya. Molecular dynamics simulation of adsorbent layer effect on tangential momentum accommodation coefficient. *J. Fluids Eng.*, 129:31–39, 2007.
- [18] F.J. Frandsen, L. Moiraghi, S. van Lith, P.A. Jensen, and P. Glarborg. Release of metals, sulphur and chlorine and residual ash formation during biomass combustion on a grate. In *Aerosol in Biomass Combustion*, pages 65–78. Medienfabrik, Graz, 2005.
- [19] S.K. Friedlander. *Smoke, Dust, and Haze*. John Wiley & Sons, New York, 2000.
- [20] N.A. Fuchs. *The mechanics of aerosols*. Pergamon Press Ltd., New York, 1964.
- [21] M.J. Haye and C. Bruin. Molecular dynamics study of the curvature correction to the surface tension. *J. Chem Phys.*, 100(1):556–559, 1993.
- [22] C. He and G. Ahmadi. Particle deposition with thermophoresis in laminar and turbulent duct flows. *Aerosol Sci. and Tech.*, 29:525–546, 1998.
- [23] M.T. Heath. *Scientific Computing, An Introductory Survey, second edition*. McGraw Hill, New York, 2002.
- [24] W.C. Hinds. *Aerosol Technology*. John Wiley & Sons, New York, 1982.
- [25] International Energy Agency. Key world energy statistics 2007. Technical report, IEA, [http://www.iea.org/Textbase/nppdf/free/2007/Key\\_Stats.2007.pdf](http://www.iea.org/Textbase/nppdf/free/2007/Key_Stats.2007.pdf), 2007.
- [26] F.M. Jaeger. Über die Temperaturabhängigkeit der Molekularen freien Oberflächenenergie von Flüssigkeiten im Temperaturbereich von - 80 bis + 1650 °c. *Z. Anorg. Allgem. Chem.*, 101(1):187, 1917.

- [27] W.S. Janna. *Engineering Heat Transfer, second edition*. CRC Press, Boca Raton, 2000.
- [28] J.R. Jensen, L.B. Nielsen, C. Schultz-Möller, S. Wedel, and H. Livbjerg. The nucleation of aerosols in flue gases with a high content of alkali - a laboratory study. *Aerosol Sci. and Tech.*, 33:490–509, 2000.
- [29] P.A. Jensen, F.J. Frandsen, K. Dam-Johansen, and B. Sander. Experimental investigation of the transformation and release to gas phase of potassium and chlorine during straw pyrolysis. *Energy Fuels*, 14:1280–1285, 2000.
- [30] M. Jöller, T. Brunner, and I. Obernberger. Modeling of aerosol formation during biomass combustion in grate furnaces and comparison with measurements. *Energy & Fuels*, 19:311–323, 2005.
- [31] J.N. Knudsen, P.A. Jensen, and K. Dam-Johansen. Transformation and release to the gas phase of Cl, K, and S during combustion of annual biomass. *Energy Fuels*, 18:1385–1399, 2004.
- [32] J.S. Lin and C.J. Tsai. Thermophoretic deposition efficiency in a cylindrical tube taking into account developing flow at the entrance region. *J. Aerosol Sci.*, 34:569–583, 2003.
- [33] D.B. Macleod. On a relation between surface tension and density. *Trans. Faraday Soc.*, 19(38):38–41, 1923.
- [34] I. Obernberger, T. Brunner, and M. Jöller. Characterisation and formation of aerosols and fly-ashes from fixed-bed biomass combustion. In *Proceedings of the IEA Seminar*, pages 69–74. Verenum, Zürich, 2001.
- [35] J. Pyykönen. *Computational simulation of aerosol behaviour*. PhD thesis, Technical Research Centre of Finland, Espoo, 2002.
- [36] J.M. Rhine. *Modelling of gas fired furnaces and boilers, and other industrial heating processes*. British Gas, London, 1991.
- [37] S. Rosseland. *Theoretical Astrophysics; Atomic Theory and the Analysis of Stellar Atmospheres and Envelopes*. Clarendon Press, Oxford, 1936.
- [38] P.G. Saffman. The lift on a small sphere in a slow shear flow. *J. Fluid Mech.*, 22(2):385–400, 1965.
- [39] P.G. Saffman. Corrigendum. *J. Fluid Mech.*, 31(4):624, 1968.
- [40] K. Sato. Sensitivity of interfacial-tension predictions to parachor-method parameters. *J. Jpn. Petrol. Inst.*, 46(2):148–153, 2003.
- [41] J.H. Seinfeld. *Atmospheric Chemistry and Physics of Air Pollution*. John Wiley & Sons, New York, 1986.

- [42] M. Smoluchowski. Versuch einer Mathematischen Theorie der Koagulationskinetik Kolloider Lösungen. *Z. Phys. Chem.*, 92:129–168, 1916.
- [43] G. Sugden. *The Parachor and Valency*. George Routledge, London, 1930.
- [44] C. Tsai and H. Lu. Design and evaluation of a plate-to-plate thermophoretic precipitator. *Aerosol Sci. and Tech.*, 22:172–180, 1995.
- [45] C. Tseng and K. Kuo. Thermal properties of phenolic foam insulation. *J. Chin. Inst. Chem. Eng.*, 25(6):753–758, 2002.
- [46] T. Valmari, E.I. Kaupinnen, J. Kurkela, J.K. Jokiniemi, G. Sfriris, and H. Reitzner. Fly ash formation and deposition during fluidized bed combustion of willow. *Aerosol Sci. and Tech.*, 29(4):445–459, 1998.
- [47] H.P. van Kemenade. Ontwikkeling prototype recuperatieve stralingsbrander. Technical report, Level Energietechniek.
- [48] H.P. van Kemenade. Aerosol and particle transport in biomass furnaces. In *Aerosol in Biomass Combustion*, pages 107–118. Medienfabrik, Graz, 2005.
- [49] H.P. van Kemenade. *Innovative Process Design*. Eindhoven University of technology, Eindhoven, 2006.
- [50] S. van Loo and J. Koppejan. *Handbook of Biomass Combustion and Co-Firing*. Twente University Press, Enschede, 2002.
- [51] VDI. *Wärmeatlas, 6th ed.* VDI-Verlag GmbH, Düsseldorf, 1991.
- [52] W. Vogelsberger. Influence of curvature-dependent surface tension on the free energy of formation of microclusters. *Chem. Phys. Lett.*, 74(1):143–146, 1980.
- [53] L. Walmann and K.H. Schmitt. Fly ash formation and deposition during fluidized bed combustion of willow. In *Aerosol Science*. Academic Press, London, 1966.
- [54] C.L. Weakliem and H. Reiss. The factor  $1/S$  in the classical theory of nucleation. *J. Phys. Chem.*, 98:6408–9412, 1994.
- [55] H. Wiinikka, R. Gebart, C. Boman, D. Boström, and M. Öhman. Influence of fuel ash composition on high temperature aerosol formation in fixed bed combustion of woody biomass pellets. *Energy Fuels*, 86:181–193, 2006.
- [56] N.B. Wood. The mass transfer of particles in acid vapour to cooled surfaces. *J. Institute of Energy*, 76:76–93, 1981.
- [57] J Zeldovich. *J. Exp. Theor. Phys.*, 12:525, 1942.

# Appendix A

## Transport equations in cartesian coordinates

The initial longitudinal flue gas velocity expressed in terms of cartesian coordinates is given by (see Bird et al. [6]):

$$v_z(x) = \frac{3}{2} \frac{\dot{m}_g}{\rho_g B W} \left( 1 - \left( \frac{x}{B} \right)^2 \right). \quad (\text{A.1})$$

where  $v_z(x)$  represents the axial flue gas velocity. The coordinates  $x$  and  $z$  represent respectively the transversal and longitudinal coordinate. In Eq. A.1,  $\dot{m}_g$  represents the mass flow through one heat exchanger passage, whereas  $\rho_g$  represents the density of the flue gas.  $B$  represents half the plate distance whereas  $W$  is the width of the plates.

Conservation of momentum is applied for the calculation of the axial flue gas velocity at an arbitrary position in the heat exchanger passage (see Bird et al. [6]):

$$0 = -\frac{\partial p}{\partial z} + \mu_g \frac{\partial^2 v_z}{\partial x^2}, \quad (\text{A.2})$$

where the term  $\frac{dp}{dz}$  represents the pressure gradient and  $\mu_g$  is the dynamic viscosity of the flue gas.

The energy equation expressed in cartesian coordinates under assumption that heat conduction in the axial direction is much smaller than heat convection and the flow is not sufficiently fast that viscous heating is significant is given by (see Bird et al. [6]):

$$\rho_g c_{p,g} v_z \frac{\partial T_g}{\partial z} = k_g \left[ \frac{\partial^2 T_g}{\partial x^2} \right] - \Delta H \frac{dm}{dt}, \quad (\text{A.3})$$

where  $\rho_g$  and  $c_{p,g}$  represent respectively the density and the heat capacity of the gas and  $T_g$  is the temperature of the gas. The last term on the RHS of Eq. A.3 represents the latent heat release by the particles formed.

The continuity equation for aerosol forming species expressed in cartesian coordinates under assumption that the total pressure  $p_{tot}$  remains constant is given by (see Bird et al. [6]):

$$\frac{\partial p_\alpha}{\partial z} = \frac{p_{tot} M_g}{R_u \rho_g v_z} \frac{\partial}{\partial x} \left( \mathbb{D} \frac{1}{T_g} \frac{\partial p_\alpha}{\partial x} \right) - \frac{p_{tot}}{v_z \rho_g} \frac{dm}{dt} \quad (\text{A.4})$$

The first term on the RHS of Eq. A.4 represents the vapour flux towards the cold heat exchanger wall. The second term on the RHS is a source term, which consists of a part which describes the gas to particle process. Furthermore  $M_g$  is the molar mass of the carrier gas whereas  $R_u$  is the universal gas constant and  $\mathbb{D}$  is the diffusion coefficient.

# Dankwoord

Na 4 jaar, met veel plezier en hard gewerkt te hebben, is het proefschrift dan eindelijk af. Vele personen hebben op verschillende disciplines hun bijdrage geleverd aan dit werk, waarvoor ik ze dan ook zeer dankbaar ben.

Om te beginnen was mijn promotie nooit tot stand gekomen zonder de inzet van mijn eerste promotor prof. Bert Brouwers, welke op belangrijke momenten mij de nodige motivatie gaf om onoverkomelijke problemen te overwinnen. Verder wil ik je bedanken voor het vertrouwen wat je in mij hebt gesteld en niet te vergeten de diverse reizen welke we, al dan niet in gezelschap van anderen hebben gemaakt, met de bijbehorende etentjes en versnaperingen. Dit geldt zeker ook voor mijn copromotor Erik van Kemenade met wie ik samen Europa in ongeveer alle denkbare vormen van vervoer heb doorkruist. Verder wil ik Hans Kuerten hartelijk danken. Niet alleen voor de gezelligheid tijdens de koffie 's morgens en de reis naar Glasgow, maar ook voor je inzet om het proefschrift van het nodige commentaar te voorzien. Tevens wil ik de overige collega's hartelijk danken voor de plezierige samenwerking.

Natürlich möchte ich auch Prof. Ingwald Obernberger und Thomas Brunner herzlich für Ihnen Einsatz und Motivation danken. Ihre Hilfe und Kenntnis war sehr wichtig für die Abrundung meiner Doktorarbeit. Außerdem danke ich auch *Peppi* und Joachim herzlich für die Hilfe während der Experimente. Selbstverständlich möchte ich mich auch bei allen anderen Mitarbeitern herzlich für die angebotene Hilfe bedanken.

Naast theoretische ondersteuning, ben ik Geert-Jan, Henry en Gerard ook zeer erkentelijk voor hun praktische ondersteuning. In het bijzonder wil ik Geert-Jan hartelijk danken voor zijn bereidheid de praktische ondersteuning vanuit de TU/e te demonstreren in Graz. Geert-Jan, bedankt voor al je hulp en plezierige samenwerking.

Om de dag goed te beginnen, is koffie voor mij erg belangrijk. Niet alleen de geur van het aroma draagt hieraan bij, maar ook de gezelligheid van mijn kamergenoten, Mart, Niels en in het bijzonder Ralph. Daarnaast wil ik ook alle overige collega AiO's bedanken, in het bijzonder, Raymond, Guy, Nicole, Joost, David en Arend.

Als laatste wil ik een aantal voor mij persoonlijk belangrijke mensen danken. Allereerst wil ik mijn ouders en *Bruur* hartelijk danken voor hun steun, wat zeer belangrijk voor mij was. Last but not least: Josée, dank voor al je liefde, steun en alles wat je voor me gedaan hebt gedurende deze periode.

Carlo





# Curriculum vitae

Carlo de Best was born on March 3rd, 1977 in Wamel, The Netherlands. From 1989 to 1993 he followed secondary education (MAVO) at the Joannes Bosco Mavo in Druten. In 1993 he started his technical study (MBO) mechanical engineering at "Technisch College Nijmegen" in Nijmegen. During this study he did several practical traineeships.

After his MBO graduation in 1997 he started his B.Sc. study mechanical engineering at "Hogeschool 's Hertogenbosch" in 's Hertogenbosch, where he received his BSc. degree (Cum Laude) in June 2000. During his BSc. project, which he carried out at Robert Bosch Packaging in Weert, The Netherlands, he proposed several constructional adaptations to improve the reliability of the sealing process for polymer packaging materials

In November 2003 he received his MSc. degree (Cum Laude) in Mechanical Engineering from the Technische Universiteit Eindhoven (TU/e). During his internal traineeship, which he carried out at TU/e, he designed a *bubble generator* used to investigate bubble detachment in a uniform approaching flow. In February 2003 he started his MSc. project at the TU/e in close cooperation with Nestlé Food Production, The Netherlands. The goal of the project he worked on was to improve the drying process of potato granules. Several design proposals, supported by analyses of the flow in a mock-up and by numerical calculations of evaporating potato granules were made and implemented in real scale applications.

Since December 2003 he is a PhD. student in the Process Technology group at the department of Mechanical Engineering of the Technische Universiteit Eindhoven. The topic of his research is to reduce the fine particulate emissions during the combustion of woody biomass fuels in small-scale biomass combustion plants. This project, which is a part of the EU project BioAsh, is carried out in close cooperation with several international partners.



















